Modeling reconfiguration strategies in plants submitted to flow

Diego Lopez

École Polytechnique
Laboratoire d'Hydrodynamique

Thèse présentée pour obtenir le grade de

DOCTEUR DE L'ÉCOLE POLYTECHNIQUE
Spécialité : Mécanique

par

Diego LOPEZ

Modeling reconfiguration strategies in plants submitted to flow*

*Modèles de stratégies de reconfiguration dans les plantes soumises à un écoulement

Thèse soutenue le 15 octobre 2012 devant le jury composé de:

M. Bruno MOULIA	Président	PIAF, INRA, Clermont-Ferrand
M. Barry GARDINER	Rapporteur	INRA, Bordeaux
M. Benoît ROMAN	Rapporteur	PMMH, ESPCI, Paris
M. Dominique CHAPELLE	Examinateur	INRIA, Saclay
M. Sébastien MICHELIN	Co-directeur de thèse	LADHYX, Ecole Polytechnique, Paris
M. Emmanuel DE LANGRE	Directeur de thèse	LADHYX, Ecole Polytechnique, Paris

Remerciements

Je tiens à remercier en premier lieu mes deux directeurs de thèse, Emmanuel de Langre et Sébastien Michelin. Ils m'ont énormément appris, tant sur le plan scientifique que sur le métier de chercheur. Ils ont su me laisser la liberté de développer mes idées tout en restant présent lorsque je me perdais dans des méandres de calculs ou que je revenais sur des questions déjà posées et résolues. Je leur suis très reconnaissant d'avoir su me remettre sur les rails quand il fallait! Je les remercie pour la confiance qu'ils m'ont témoignée, qui m'a donné un soutien en toutes circonstances. Enfin je les remercie de m'avoir donné l'opportunité de prendre l'air (et le soleil...) à l'UC San Diego; cet échange m'a donné un tout nouvel élan pour aborder ma dernière année de thèse.

Je remercie également les membres de mon jury, Barry Gardiner, Benoît Roman, Dominique Chapelle et Bruno Moulia, pour avoir accepter d'évaluer mon travail et pour l'intérêt qu'ils y ont porté.

Je veux remercier Eric Lauga de m'avoir accueilli dans son groupe à l'UCSD, et bien sûr Christophe Eloy pour le travail que nous avons pu faire ensemble là-bas, pour sa grande disponibilité et son intérêt pour mon sujet.

La motivation pour la recherche ne vient pas de nulle part. Je dois en grande partie mon goût pour la recherche à Laurent Jacquin, que je remercie fortement d'avoir voulu nous expliquer lors des descentes de l'Ardèche toute la complexité de l'eau sur laquelle nous circulions, alors que nous ne pensions qu'à ramer! Je remercie également les amis que j'ai pu rencontrer lors de mon premier vrai contact avec la recherche au Québec, Bertrand, Kris, Alberto, Lavinia, Andrei et Marcel: ils ont réussi à ne pas m'effrayer du monde mystérieux de la recherche, et même plutôt à m'en donner le goût (pour rester québecois).

Une thèse ne pourrait pas se dérouler agrèablement sans une équipe fiable et un laboratoire dynamique, que ce soit du côté administratif, scientifique, ou humain. Aussi, j'exprime toute ma reconnaissance envers Patrick Huerre, Jean-Marc Chomaz et Christophe Clanet pour l'ambiance chaleureuse qu'ils ont su créer et maintenir au Ladhyx; Sandrine, Thérèse, Caroline et Tonio, pour leur efficacité et temps de réponse record en toutes circonstances, Dany pour avoir pris au sérieux mes gros problèmes informatiques, tels qu'un flash-payer en panne; enfin, tout un ensemble de doctorants, post-doc, stagiaires, grâce à qui les mardis midi ont ressemblé à des rediffusion du Barça-Real, les pauses café à des concours de mots-féchés, pour avoir fondé ce site d'avenir (ou du passé...) qu'est Doctranet, et pour avoir instauré les tartateam. Je remercie ainsi Anders, Benoît, Loïc, Cristobal pour le pisco sour, Etienne pour ses buts des lunettes, Clément, Franz pour l'intégrale du film que je n'ai pas pu voir, Marine, Nicolas pour ses idées de soirées, Fabien, Caroline pour ses gâteaux, Adrien, Rémi pour ses beaux logos multicolores en micro-flu, Xavier pour son calme à toute épreuve (et sa contribution engagée à doctranet), Christelle pour ses belles imitations de plantes en mouvement et Miguel pour toutes les délicates expressions mexicaines qu'il a voulu m'apprendre!

Pour leur présence au cours de ces années de thèse (et même avant), je tiens à remercier mes amis de longue date Hugo (pour tout...), Louis-J et Louis, les amis de l'escalade, Jon, Fabien, ceux du volley, Pierre, Sofia, Henri, Antoine, Paul et Sylvan. Merci à Joseph pour sa patate permanente, Louise pour la vie nocturne de Montpellier, Hélène pour les soirées à thème. Sans la musique il paraît que la vie pose quelques problèmes, alors je remercie aussi "mes chers amis" Joël, Hélène (x2), Agnès, Anna, Eric; j'ai une pensée émue pour Pascal et les Dolce, Camille, Marie-Léonie et Vincent, avec qui mon violoncelle et Mêêêndelssohn ont pris une toute autre ampleur!

Enfin, il en est sans qui rien de tout ça n'aurait pu arriver. Je finis donc par une forte pensée et de grands remerciements pour ma famille, toujours là, qui m'a soutenu depuis la construction du premier lego jusqu'à la destruction de tous ces arbres, mes parents, mon frère et ma sœur (contribution artistique en couverture de ce manuscrit), Flavia, et le petit Pablo qui, inspiré par mes travaux, s'amuse maintenant à reconfigurer les plantes d'intérieur.

Merci!

Contents

Chapter 1

Introduction

Among the living beings surrounding us, plants are very intriguing and inspiring subjects. Plants are used in many different ways, from agriculture to decoration, and their properties have been a continuous source of interest for men. The particular response of terrestrial plants to the wind gave rise to various interpretations; an example is that of the oracles in Dodona (Greece, 500 BC), where the rustling of the oak or beech leaves was interpreted by priests (Fontenrose 1988). A more rational historical approach is that of the Beaufort scale (1805), which characterizes wind intensity through qualitative observations. For instance, a gentle breeze is defined by: "Leaves and small twigs constantly moving, light flags extended" (Huler 2004).

In fact, significant loads result from the fluid – be it air or water – flowing around plants, greatly influencing their growth, reproduction, and survival. Indeed, wind can cause heavy damages to cereal cultures or forests, with consequential economic loss. Plants have developed different strategies for surviving in stressful environments. The understanding of the complex interactions between flow and plants can be of great interest in many fields, from fundamental mechanics to applied forestry or agriculture. The problem of interaction between flow and vegetation is also an original fluid-structure interaction problem. The interactions between flow and a complex body – complex by its geometry and its mechanical behavior – are not trivial, and the response of such bodies to the flow is not yet fully understood. The need of a better understanding of the plants' strategies and responses to external loads has therefore raised the interest of the scientific community for the past decades.

The purpose of this work is to study the response of plants to external loads induced by the fluid flow. From a fundamental point of view, our aim is to characterize the behavior of plants under static loads while taking into account accurate geometries and mechanical properties, and therefore derive a simple continuous model for the study of the interactions between plants and external flows. In this introductory chapter, we first present the motivations for this study by looking at the general effects of flow on plants. We will then provide a selective review of the current knowledge on flow-plant interactions, with a closer look at the response to static loads.

Figure 1.1: Wind-induced lodging in a wheat field. The clear areas correspond to lodged wheat [WEB01].

1.1 Flow effects on vegetation – A general overview

1.1.1 A stressful environment

The fluid surrounding terrestrial plants and aquatic vegetation is a major source of external stress on vegetation. The loads resulting from the fluid flow are non-uniform and variable in time, orientation and intensity (de Langre 2008, Koehl *et al.* 2008). The consequences of such loads are multiple, from growth modification to irreversible destruction of the plant.

From an agronomic and economic point of view, the destruction of plants by the wind originates massive production losses on cereal crops or forests (Berry *et al.* 2004, Gardiner & Quine 2000). A crucial problem in cereal plantations is lodging, that is, cereals being blown down in an irreversible way, as shown in Figure 1.1. Lodged crops are much more difficult to harvest, when not irremediably damaged, and result in 10 to 30% annual production loss (Farquhar *et al.* 2000, Berry *et al.* 2004). In the past decades, considerable improvements were made in selecting shorter and more resistant varieties, but lodging remains a major problem for the global food-industry.

Similarly to cereal crops, trees and forests experience severe damage from extreme events like storms, which provoke substantial losses to the wood industry. For instance, the damages caused by the storm Lothar in France in 1999 are estimated to 140 million cubic meter of wood (Vernier 2001). As trees are widely used in urban conditions, they represent a significant risk to people and goods, and their destruction by the wind can cause important damages (Kane *et al.* 2008). A good understanding of the flow effect on trees and forests is therefore necessary for improving the management of forests, for instance by thinning the stand or artificially pruning some trees (Gardiner *et al.* 2008, Larjavaara 2010).

In water, benthic organisms are also affected by the water currents and waves (Koehl

Figure 1.2: Photograph of a mountain flag tree. The branches are all oriented along the main flow direction [WEB02].

1984). Seaweeds or giant kelps are swept by the waves and undergo large amplitude oscillations (Gaylord *et al.* 2008, Koehl *et al.* 2008), and coral colonies, which are crucial for the equilibrium of the marine ecosystems, can be irremediably damaged by extreme events (Madin 2005, Denny & Gaylord 2010). In fact, even if the mass ratio – solid density compared to fluid density – is very different between terrestrial plants and benthic organisms, the interactions between aquatic plants and their surrounding fluid are similar and raise identical questions.

1.1.2 Growth modification: thigmomorphogenesis

In order to resist the mechanical stresses they experience, plants can adapt their growth to their environment; this is referred to as thigmomorphogenesis (Jaffe 1973, Moulia *et al.* 2006, Telewski 2006). This adaptability leads to significant morphological variations that are observable in many types of plants. A well-known example of a plant strongly modified by the external flow is the flag tree, Figure 1.2. Here, the tree grows under a strong wind with a permanent direction, and its branches show a very specific pattern, as most of them are oriented along the flow, downwind.

Figure 1.3 shows two examples where the morphology of the plant is very different depending on its growth environment. The experiment shown in Figure 1.3a was conducted on Alfalfa by Moulia & Combes (2004), showing that for the same biomass the plants with limited movement grew 40% higher than those that could move freely. Similarly, Koehl *et al.* (2008) showed how giant kelp blades were modified depending on flow conditions (Figure 1.3b). The kelps growing in high current regions exhibit smooth and streamlined blades, as opposed to the ruffled blades of kelps growing in slow flow regions. This is also observed in trees. Baker (1997) pointed out important morpholog-

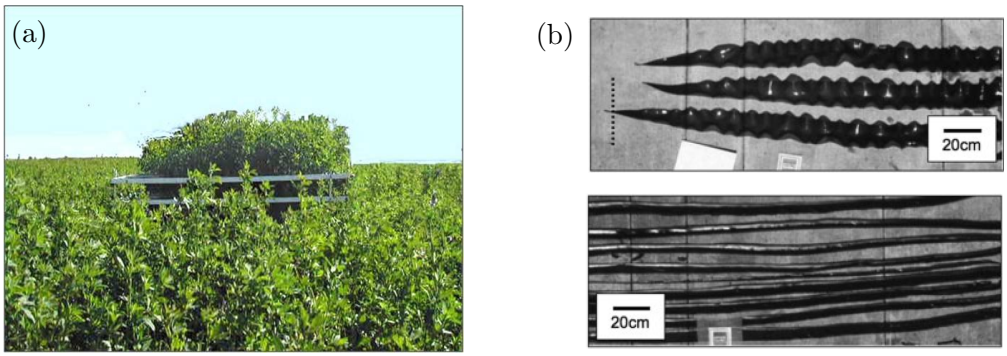

Figure 1.3: Examples of thigmomorphogenesis: (a) Alfalfa growing between grids grew much higher than when free of movement, from Moulia & Combes (2004); (b) Macroalgae blades (*N. luetkeana*), growing in slow flow area (top) and high currents area (bottom), from Koehl *et al.* (2008).

ical and mechanical differences in lime trees when growing isolated or in a stand. Such differences can be also visible within the same stand, as it was observed in a forest from the edge to the center (Bruchert & Gardiner 2006). This adaptability yields important modifications of the mechanical properties (Speck & Burgert 2011). An example is that of tutored plants, which are generally higher but less stiff than natural plants (Jacobs 1954); tutored plants can buckle under their own weight if the tutor is removed. The modifications are also appreciable on the anchorage properties, and the root system is strongly dependent on the flow conditions on the plant (Nicoll *et al.* 2008).

It is now established that plants are sensitive to the deformations induced by external loads (Coutand & Moulia 2000). By performing experiments on young poplar trees under dynamic loads, der Loughian (2012) showed that trees are not sensitive to the dynamic component of the load but only to the static deformation. This suggests that one needs to understand well the static deformation induced by the flow in order to assess the consequences on the plant's morphology. Before focusing on the static response of plants to an external flow, which is the object of the present work, we present hereafter some elements on the dynamic response of plants submitted to a flow.

1.1.3 Flow-induced oscillations

The flow surrounding plants generally has a strong unsteady component that provokes a dynamic response of the plant (de Langre 2008). Flow-induced oscillations can play an important role in plant breakage. Hence, the mechanisms by which the plants dissipate the energy transferred from the fluid to the solid plays a major role. Energy dissipation is usually done through viscoelastic damping (within the structure) and aerodynamic damping (with the surrounding fluid).

The oscillatory behavior of trees has particular characteristics due to their branched geometry. Sellier & Fourcaud (2005) observed a modal localization, suggesting that different branch levels oscillate at different natural frequencies, and Rodriguez *et al.*

(2008) showed how this modal localization was linked to the tree architecture. Recently, Theckes *et al.* (2011) pointed out the occurrence of a non-linear energy transfer from trunk vibration modes to branch modes. Therefore, the energy is transferred to higher branch levels where aerodynamic and viscoelastic dissipation can occur. The tree's architecture may play an important role for survival under extreme events by facilitating energy dissipation from the vital parts, i.e. the trunk, to regions with higher damping possibilities (aerodynamic damping due to leaves, for instance).

At the scale of a canopy, which is a group of homogeneous plants close to each other compared to the size of the canopy, the wind can be at the origin of global dynamics involving the entire canopy. The fluid-structure coupling that occurs is analogous to a mixing layer (Raupach *et al.* 1996), with large eddies forming over the canopy. As a result the canopy starts waving, a phenomenon called honami (Inoue 1955), see Figure 1.4. This behavior can lead to a resonance of the waving plants, and it is possibly involved in lodging. Numerical computations provide accurate predictions of this behavior (Dupont *et al.* 2010), and advances in experimental techniques for quantifying this phenomenon have provided additional elements for its understanding (Py *et al.* 2005). When this phenomenon occurs, a frequency lock-in is observed: in a wide range of flow velocity, the waving frequency of the canopy is the natural frequency of the plants for terrestrial plants (Py *et al.* 2006), and five times smaller for aquatic vegetation, where the mass ratio is clearly different (Ghisalberti & Nepf 2002, Gosselin & de Langre 2009).

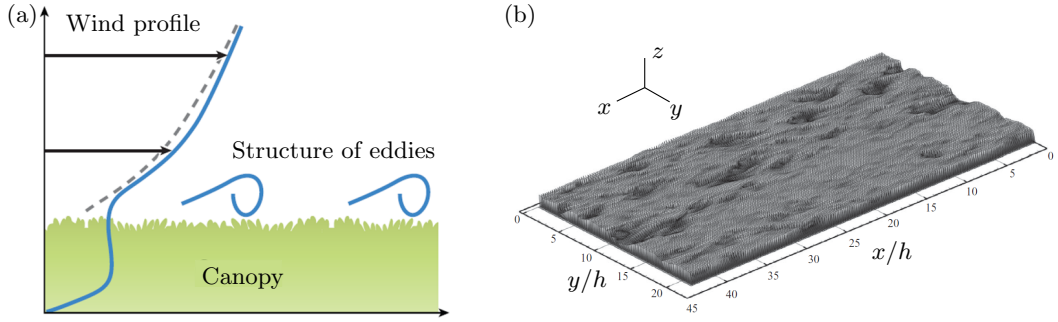

Figure 1.4: (a) Sketch of the flow structure above a canopy; (b) Numerically computed honami (LES), from Dupont *et al.* (2010).

In the mechanisms presented here, a key mechanical property of the plants is their ability to deform significantly. In the next section, we present the consequences of this property on the static response of vegetation submitted to flow.

1.2 Static response to external flow

As it was discussed previously, plants modify their growth and adapt themselves to the mechanical stress they experience on the long term. However, flow-induced loads generally have short-term variations. Hence, plants require generic strategies for handling large fluid-loading and surviving to extreme events. In addition to energy dissipation

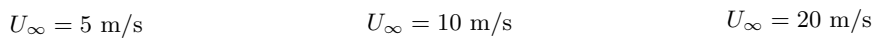

Figure 1.5: Tulip tree leaf reconfiguring as the flow velocity increases, from Vogel (1989). The fluid flows from left to right.

strategies when the flow induces important oscillations, the static response of plants reveals remarkable behaviors, providing significant resistance to heavy fluid-loading. Besides, thigmomorphogenetic response is related to static flow-induced deformations; understanding the static response to wind-loads is relevant for the analysis of plant growth and adaptability. We review hereafter several mechanisms that exist in plants for reducing flow-induced static loads.

1.2.1 Elastic reconfiguration

A key characteristic in plants is their ability to significantly change their geometry under flow. As opposed to most man-made structures that are built to resist fluid-loading without experiencing any noteworthy deformation, plants are typically less stiff. Due to their high slenderness, the deformations they undergo can be of the order of the size of the plant itself. The significant deformation of a plant under an external flow is referred to as reconfiguration, suggesting some sort of adaptability of the plant to the external flow (Vogel 1984; 1989). This adaptability, however, is different from thigmomorphogenesis, as it is temporary and reversible. The first analysis of reconfiguration was carried out by Vogel (1989) on a tulip tree leaf (*Liriodendron tulipifera*). In that case, the leaves reconfigure into a conical shape as the flow velocity is increased (see Figure 1.5).

Geometrical changes under this reconfiguration process have a major effect on flow-induced loads (typically the drag). Indeed, two aerodynamic effects, resulting from this change of shape, can be identified: (i) a reduction of the frontal area and (ii) a streamlining of the body allowing a better pressure recovery in the body wake. These two behaviors are visible in Figure 1.5, from sketch (a), at low fluid velocity, to sketch (c), at high fluid velocity, where the leaf presents a smaller area facing the flow and a more streamlined shape. As the drag is typically proportional to the frontal area with a drag coefficient that depends on the streamlining of the body, the two behaviors contribute to reducing the drag; the resulting drag is lower to that of a non-deformable body.

Flow-induced deformations depend on fluid velocity: under increasing fluid velocity reconfiguration becomes more important. Hence, drag evolution with flow velocity differs from that of a bluff body. Its dependence to flow velocity is generally expressed through the Vogel exponent ν (Vogel 1984), namely

$$T \sim U^{2+\nu}, \tag{1.1}$$

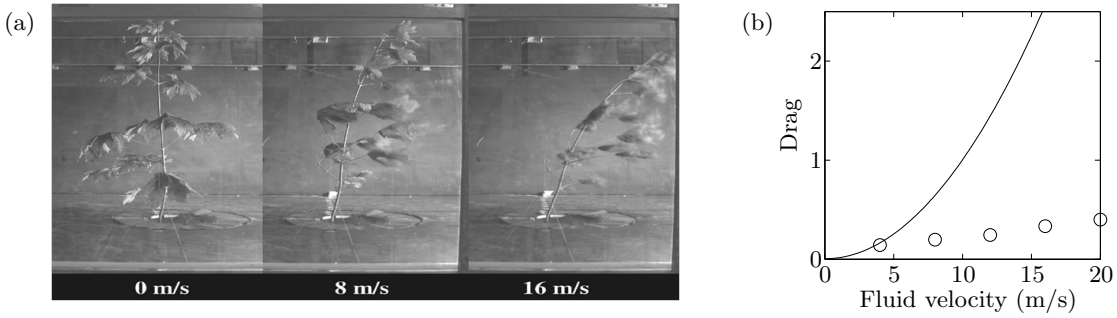

Figure 1.6: Reconfiguration of a bigleaf maple in a wind tunnel, from Vollsinger *et al.* (2005): (a) lateral views under increasing flow velocity; (b) Drag (arbitrary units) as a function of fluid velocity: (∘) experimental data, (—) extrapolated drag without reconfiguration.

where T is the drag and U the fluid velocity. The Vogel exponent is usually negative, and the value $\nu = 0$ corresponds to the drag of a rigid body. Some Reynolds number effects may cause a drag reduction for the smallest plant components, but at the scale of the entire plant geometrical changes are the major cause for drag reduction.

An example of drag reduction measured experimentally is shown in Figure 1.6. In these experiments, Vollsinger *et al.* (2005) measured in a wind tunnel the reconfiguration of different hardwood species, combining both visualization and drag measurements. The flow-induced deformation of the plant (here a bigleaf maple, *Acer macrophyllum*) is clearly visible, and the resulting drag reduction is shown on Figure 1.6b. The solid line corresponds to an extrapolated bluff body drag ($\nu = 0$), for comparison. The actual drag evolves almost linearly with the flow velocity, which corresponds in that case to a Vogel exponent around -1.

This mechanism of drag reduction by deformation is observed in a wide variety of plants, in air (Rudnicki *et al.* 2004, Speck & Spatz 2004), or water (Koehl 1984, Stewart 2006), to cite a few. Moreover, this is also observed in model geometries such as fibers in a two-dimensional soap film (Alben *et al.* 2002), discs in water modeling the reconfiguration of Vogel's tulip tree leaf (Schouveiler & Boudaoud 2006), and more recently plates and fibers in air (Gosselin *et al.* 2010). A remarkable feature is that the Vogel exponent is always found around the value $\nu \sim -1$, the exact geometry and the fluid type does not seem to play an important role in the scaling of drag reduction.

One can note that the Vogel exponent corresponds to an asymptotic regime, in the fully reconfigured state. In some cases, the drag can increase at first, before reaching the asymptotic regime. This was noted by Vogel (1984), and it results from the reconfiguration of an upwind-facing body. On the onset of reconfiguration, the frontal area increases first, hence increasing the drag.

Whereas the absolute value of the drag is very dependent on the structure itself, a common representation for reconfiguration is to consider the drag normalized by the drag of a non-reconfigurable body, and to plot it against a normalized fluid loading

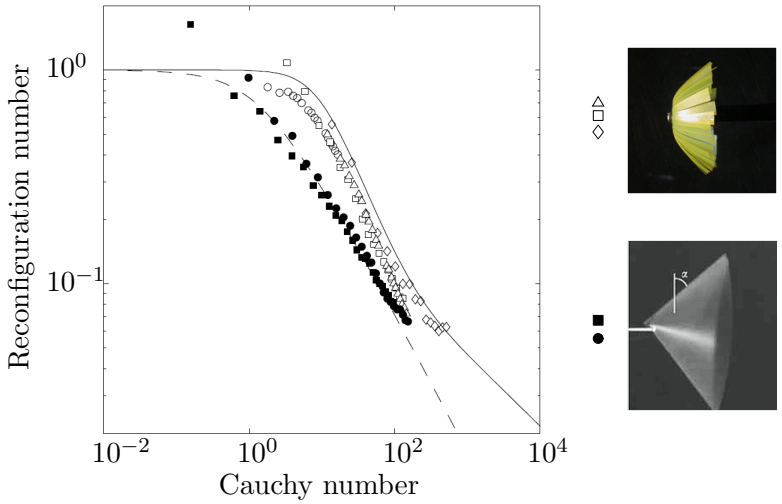

Figure 1.7: Representation of drag reduction by reconfiguration through reconfiguration curves, from Gosselin *et al.* (2010). The white symbols represent the experimental data from Gosselin *et al.* (2010), the black symbols that of Schouveiler & Boudaoud (2006) on two disks in a water flow; their corresponding models are plotted as (—) and (- - -), respectively.

(de Langre 2008). This normalized drag is referred to as the reconfiguration number, defined as

$$\mathcal{R} = \frac{T}{T_{\text{rigid}}}, \tag{1.2}$$

where T_{rigid} is the drag of the rigid body. The non-dimensional fluid load is the Cauchy number C_Y, which scales the fluid load with the modulus of elasticity (or Young modulus) E,

$$C_Y \sim \frac{\rho U^2}{E}, \tag{1.3}$$

where ρ is the fluid density; the exact scaling depends on the structure geometry (Niklas 1992). The Cauchy number therefore characterizes the flow-induced deformations. For instance, a low Cauchy number implies that the flow dynamic pressure on the structure is negligible compared to the body stiffness, resulting in low deformations. This representation provides common generic curves of reconfiguration. Figure 1.7, from Gosselin *et al.* (2010), shows the reconfiguration curves of the experimental and numerical work of Schouveiler & Boudaoud (2006) and Gosselin *et al.* (2010); the different curves exhibit very similar patterns.

The review of de Langre *et al.* (2012) on a wide variety of biological systems and models showed that any elastic structure submitted to a flow follows a similar reconfiguration law, with a Vogel exponent typically around $-2/3$.

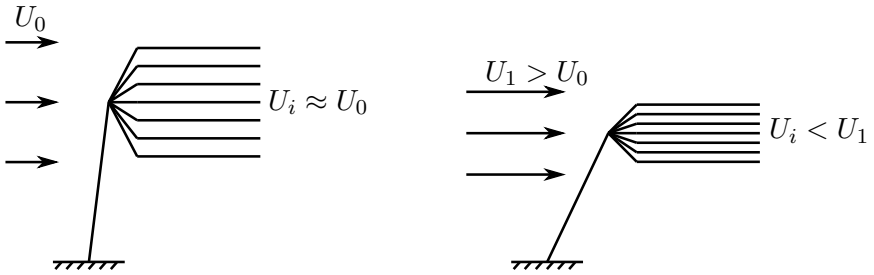

Figure 1.8: Friction drag reduction by clumping in a giant kelp: at high flow velocity, the inner fluid velocity U_i is less than that of the free stream flow.

1.2.2 Load reduction by porosity effect: clumping

The mechanism described above applies to isolated bodies under flow. For a more complex medium made of different elements, additional effects are observed as the fluid flows within the structure. In the non-deformable case, Grant (1983) noted a change of flow "penetration" inside a spruce twig as flow velocity increased. In that case, the flow will be more likely to "avoid" low porosity regions. The parts of the plants located inside these regions are thus submitted to a lower flow velocity than the free stream velocity. When the body can deform significantly, different elements get packed together, thereby modifying the porosity; the plant acts as a poroelastic medium. Packing induces a reduction of porosity, which may result in less effective flow velocity inside the plant, hence reducing the total drag of the body.

A change in porosity from flow-induced deformations was observed in giant kelps (*Nereocystis luetkeana*) (Koehl & Alberte 1988, Koehl *et al.* 2008). The blades of the kelps are packed together in a clump, and the inner fluid velocity is lower than that of the free stream flow (see Figure 1.8). In this case, the total drag of the structure is essentially due to the friction drag along the blades; the flow velocity reduction inside the clump induces a significant drag decrease. When the drag of the structure is related to the pressure drag – which is typically the case in air – similar results can be observed (Gosselin & de Langre 2011). In this study, the authors investigated both experimentally and theoretically the reconfiguration of an ideal poroelastic system. A key result is that the Vogel exponent is changed from $-2/3$, for a single beam, to -1, for this particular poroelastic system made of beams, as the porosity (at rest) decreases. The drag reduction is therefore more important for a bundle a beams than for an isolated beam.

As opposed to the reconfiguration of isolated bodies, which has been abundantly studied over the past decades, the reconfiguration of a poroelastic medium is not yet fully understood. Accurately reproducing the reconfiguration of such systems necessitates fully coupled fluid-structure models. Since such models are usually complex and require heavy computations, it is of capital importance to identify the key elements of the problem to derive simpler models.

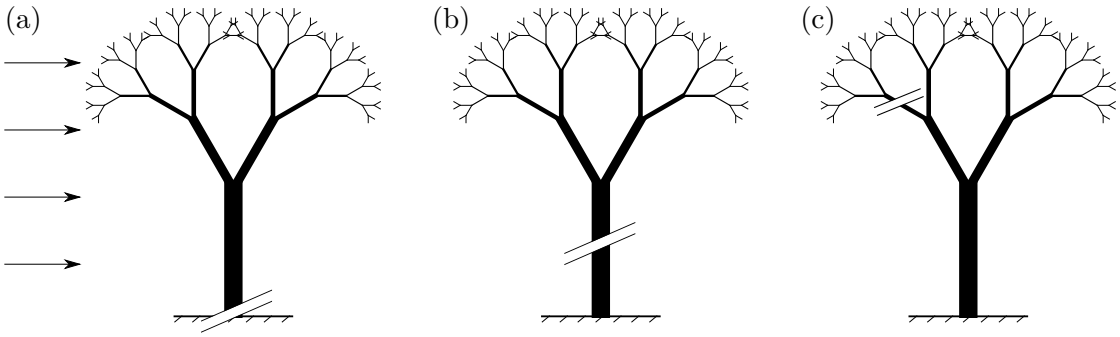

Figure 1.9: Schematic view of breakage process in a branched brittle system under flow. (a) Base breakage, (b) Trunk breakage, (c) Branch breakage.

1.3 Flow-induced breakage: pruning

The mechanisms of load reduction presented above rely on the ability to undergo large deformations compared to the size of the body. However, plants show a wide variety of mechanical behaviors, and not all are very flexible. A second typical behavior observed in plants submitted to an external flow is breakage; this will be referred to as brittle behavior, as opposed to the flexible behavior presented above. Breakage can result from flow-induced oscillations as well as static loads. We focus hereafter on the occurrence of breakage in the static case, and disregard the effect of the structural dynamics.

The occurrence of breakage has already been reported in corals or trees (Koehl 1984, Niklas & Spatz 1999), therefore suggesting that this behavior is more likely to be observed in slender ramified structures. Such structures are ubiquitous in nature: trees (McMahon 1975), bushes, algae (Koehl 1984), corals (Madin 2005) and corallines (Martone & Denny 2008), to list a few. In the following we refer mainly to trees under wind loading, with the understanding that these results are also applicable to a large variety of other biological systems under fluid-loading. For a brittle branched system attached to a support, one can identify schematically three distinct types of breakage, sketched in Figure 1.9. The first one is base breakage, Figure 1.9a; the attachment to the ground is broken, as in uprooting or windfall. The second type is trunk breakage, Figure 1.9b, when the main element is broken (windbreak). Finally, branch breakage, when an upper element breaks, is illustrated in Figure 1.9c; this can be referred to as flow-induced pruning.

In fact, the distinction between trunk and branch breakage has a biological relevance, since breakage of the trunk is likely to be fatal, while re-growth is often possible after branch breakage. Moreover, branch breakage does reduce loads on the trunk and the attachment, thereby delaying their breakage (Koehl 1984, Niklas & Spatz 2000). This can be considered as analogous to elastic reconfiguration, where a change in geometry (or in this case topology) results in load reduction. Furthermore, branch breakage can also be part of the asexual reproduction process by propagation. This is observed in terrestrial plants such as willows and poplars (Beismann *et al.* 2000), and in stony corals such as *Acropora Cervicornis* or *Acropora Palmata* (Tunnicliffe 1981, Highsmith 1982).

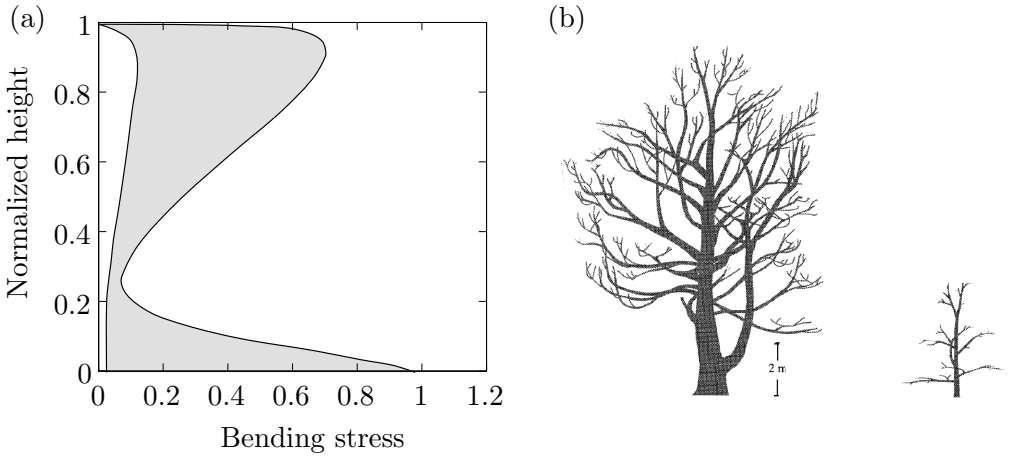

Figure 1.10: (a)Schematic view of the bending stress profiles given by Niklas & Spatz (2000) for five cherry trees, showing a local maximum near the top. (b) Corresponding geometry of two cherry trees.

Breakage is the consequence of an unacceptable stress level, and is therefore directly related to the stress state in the structure (Niklas & Spatz 2000, Gardiner & Quine 2000). In particular, the issue of whether the stress level is uniform or not in the tree is crucial, as breakage is expected to occur at the point of maximal stress. For instance, Niklas & Spatz (2000) showed that, in several cherry trees, the flow-induced stress level varies by one to two orders of magnitude within the tree and has a local maximum in the branches (Figure 1.10). On the other hand, Bejan *et al.* (2008) showed that flow-induced stress is uniform for a tapered trunk when the taper is linear.

Tree geometry plays an important role on stress distribution. Considering the stress induced by gravity, McMahon & Kronauer (1976) showed how the stem taper plays a role in the tree resistance to buckling under its own weight, but the effect of the taper on the wind-induced loads is not yet fully understood. Eloy (2011) recently investigated a law characterizing the branching nodes of a tree, from the wind-induced loads point of view, providing new elements for understanding the effect of flow on tree geometry and the possibility of breakage. In this work, the conservation of total branch section at a branching point was shown to be the best design to resist wind-induced fracture.

Apart from this work, the general relationship between the architecture of trees and the flow-induced stress state has not been studied. The localization of breakage under flow is not fully understood, and the physical parameters driving the occurrence of breakage are not yet clearly identified.

1.4 Models for the mechanical behavior of plants

Modeling and predicting the behavior of plants under flow is a challenging issue. To optimize the management of plantations, such as cereal fields or forest stands, reliable

modeling tools are required. Computation of accurate stress levels in plants is crucial in determining their response to flow, and in identifying the possible occurrence of breakage in the structure. Numerous models of the interaction between flow and plants or canopies have been developed over the past decades; we review hereafter some of these models suitable for numerical computations.

For simple geometries like cereal crops or seaweeds, most models use a cylindrical beam representation (Baker 1995, de Langre 2008, Luhar & Nepf 2011). For more elaborate geometries like trees, the ramified geometry is often modeled by an assembly of rods. The resulting geometry can be either a symmetric idealized tree (Kerzenmacher & Gardiner 1998, Rodriguez *et al.* 2008), or a fractal tree (Endalew *et al.* 2009, Eloy 2011, Bai *et al.* 2012). Large scale computations cannot be done easily using this kind of models due to their heavy computational requirements. Modeling the exact geometry of a tree is not trivial: the examples mentioned above rely on statistical laws for the geometry of trees. Considering actual tree geometries can provide interesting results. Rodriguez *et al.* (2008) studied the modal behavior of trees using different actual trees that had been entirely digitized, using a method described in Sinoquet *et al.* (1997). Such analyses provide good numerical insights but their results cannot be easily generalized.

A continuous equivalent representation of a tree as a tapered beam was first proposed by McMahon (1975) for analyzing the mechanical stability of a tree under its own weight. This model was used recently in the work of Eloy (2011) for analyzing wind-induced loads. The equivalent tapered beam is obtained by formulating the tree dimensions as a function of the height: for instance, the frontal area at branching level is the sum of the frontal area of all branches at the same level. Although the basic features of a tree-like structure are well captured by this model, it does not allow for computing the flow modifications within the tree crown.

Plant canopies are often described by continuous models, as the typical size of the canopy is by definition much larger than that of a single individual. GALES model (Gardiner *et al.* 2000), which is used for computing wind damage to conifer stands, is based on the aerodynamic roughness of the canopy surface for computing the flow-induced stress. Otherwise, in most models the canopy is studied as a porous layer (Raupach *et al.* 1996, Dupont & Brunet 2008). These models were first developed to capture the effect of the canopy on the flow, without considering canopy deformations. The fluid dynamics within and above the canopy are accurately modeled in such cases, but the mechanical response of the canopy to the flow is not captured. To understand the propagating waves observed at the canopy surface, the deformations of the canopy were added to the previous models (Doaré *et al.* 2004, Py *et al.* 2006, Hsieh & Shiu 2006, Dupont *et al.* 2010). These enhanced models provide a good understanding of the global dynamics of the canopy, but give a poor insight into the stress distribution inside a plant. Actually, the loads that the plants experience within the canopy cannot be accurately predicted, since in most models the canopy is considered to be either an array of cylindrical beams (Doaré *et al.* 2004, Py *et al.* 2006, Liu *et al.* 2010) or a homogeneous isotropic porous medium (Hsieh & Shiu 2006).

The flow in such continuous models corresponds to a non-Darcian flow in a porous

medium. This problem has been abundantly studied and a wide variety of models have been developed, predicting consistently the flow behavior (Ochoa-Tapia & Whitaker 1995, Higdon & Ford 1996, Pedras & de Lemos 2001, Hoffmann 2004). Models of high Reynolds number flow through a porous medium benefit from numerous experiments on the flow through arrays of cylinders (Koch & Ladd 1997, Nepf 1999, Tanino & Nepf 2008), but the resulting loads on the structures are less quantified. In order to compute the flow-induced loads on the structures, models need to take into account a full fluid-structure formulation through a poroelastic model. The main issue in these models is to give a constitutive equation for the material defined continuously in the porous medium. Such models are built on homogenization techniques to compute the equivalent elasticity coefficients or similar mechanical quantities of the equivalent porous structure (Diebels & Ehlers 1996, Sigrist & Broc 2008, Chapelle *et al.* 2010). The complexity of the geometries of interest make these models non trivial, and apart from the recent work of Gosselin & de Langre (2011) on drag reduction by porosity effect, there is no simple theoretical model representing a plant as a porous medium.

Current models allow for computing the flow-induced stresses in plants at different scales, from a single plant to a large scale canopy. However, fully coupled fluid-structure interaction models require heavy computations, and most fluid-structure models for plants do not take into account the complexity of the geometry, such as branching or diameter evolution.

1.5 Aim of the present work

From the different topics presented in this introduction, we see that several questions remain regarding the static response of plants to an external flow. Elastic reconfiguration has been abundantly studied, and the response of an isolated deformable body under flow is well understood. However, the mechanical behavior of plants involves also the possibility of breakage, and the occurrence of such phenomenon has not yet been related to the geometry of plants in a systematic way. In fact, the complex geometry of plants is generally not taken into account in reconfiguration studies; a question remains about the role of the geometry in the response of plants to the external flows.

The aim of this thesis is to get a general understanding of the static response of plants submitted to an external flow, and to identify the essential elements that drive the plants' behavior. By reducing then the problem to its essential ingredients, we want to derive the simplest continuous model that will still allow us to accurately compute the static flow-plant interaction problem. We are therefore interested in addressing the three following questions:

a. Can breakage be part of a reconfiguration strategy in plants?

The occurrence of breakage in plants is a key issue in terms of survival of the plant. Similarly to elastic reconfiguration, one can wonder whether breakage is part of a general reconfiguration strategy, providing additional means for surviving extreme loads. We need therefore to get a better understanding of the occurrence of breakage in plants

under static loads; this issue is addressed in Chapter 2. We are interested not only in characterizing the occurrence of breakage, but also in the possible gain for a plant of losing some of its elements under strong flow. A key issue here is to determine whether a plant will experience base/trunk breakage or branch breakage, depending on its geometry. We will focus on the ideal case of a brittle and non-deformable structure, in order to exhibit the essential elements characterizing breakage. The content of Chapter 2 was the object of a publication in the *Journal of Theoretical Biology* (Lopez *et al.* 2011), in Appendix E.

b. Are breakage and elastic reconfiguration compatible?

As we show that the mechanism of flow-induced pruning is possibly a widespread reconfiguration strategy in plants, it becomes relevant to compare and combine it with the elastic reconfiguration strategy. Indeed, the actual mechanical behavior of plants is a combination of deformation and breakage. We are therefore interested in understanding how the two strategies couple, and in characterizing the response of a plant under flow in the general case. This is the object of Chapter 3. In order to answer this question, we will characterize the kind of reconfiguration strategy a structure will follow depending on its mechanical and geometrical parameters. We will then consider the transition from the pruning strategy to the bending strategy, and point out the effect of such a combination. Finally, we will compare the results with the observations in nature, as a tool for understanding the survival strategies in plants.

c. Can these results be extended to a homogenized representation of branched systems?

This last question addresses the issue of the generalization of the previous results, obtained in the case of isolated and idealized structure. The aim is to derive a model that can be easily used for a wide variety of geometries, as an application of the results on plant reconfiguration under flow. This model should be continuous and allow for coupling the solid and the fluid equations; we also want this model to require a small number of parameters to reduce numerical computations. For that purpose, from the essential physical elements that are identified in the previous chapters, we derive a homogenized model for plants and canopies in Chapter 4. This continuous model will be developed from a porous medium approach, but with a particular attention to accurately describing the mechanical response of the solid to the flow. The model is first validated by comparison with automatically generated geometries, on which an averaging procedure is required. We then present a case where the continuous domain is created directly, without averaging process; such application enables fast computations for tree-like structures or forests under flow.

The main contributions and results of this thesis are summarized in Chapter 5. The importance of the different reconfiguration strategies in plants and the approaches used to modeling plants' response to static loads are discussed, with an emphasis on the future applications and perspectives provided by this work.

Chapter 2

Flow-induced pruning of branched systems

The present Chapter focuses on the question of flow-induced breakage in tree-like structures. As it was presented in the previous Chapter, we are interested in getting an insight into the consequences of breakage, and its possible interest as a reconfiguration strategy. Using simple numerical and analytical models for the mechanical behavior of slender and brittle structures, we want first to understand the effects of the geometric and physical parameters on the occurrence of branch breakage, as defined in Figure 1.9. In the case of branch breakage, we are interested in the occurrence of successive breaking events as the flow is increased, and in the compatibility with other constraints on the geometry, assuming that branch breakage is favorable in biological terms.

The modeling assumptions and framework used throughout this Chapter are first presented in Section 2.1. In Section 2.2, we compute the stress distribution and successive breaking events in a complex tree, using the geometry of an actual walnut tree. Using an idealized branched system, we derive conditions for branch breakage in Section 2.3. These are further analyzed with a continuous model adapted from McMahon's tapered beam (McMahon 1975), here referred to as the slender cone model, in Section 2.4. The corresponding three geometries are sketched in Figure 2.1. Finally a general discussion and conclusion on the issue of flow-induced pruning are given in Section 2.5. Apart from minor modifications, this Chapter is identical to the article published in *Journal of Theoretical Biology*, in Appendix E.

2.1 Mechanical model and parameters

Similarly to the existing studies on elastic reconfiguration mentioned in Section 1.2, we consider throughout this Chapter a cross flow over the entire structure. The flow is uniform, as the dependence of the stress on the wind velocity profile was shown to be small (Niklas & Spatz 2000). Also, only static loads are taken into account, and the

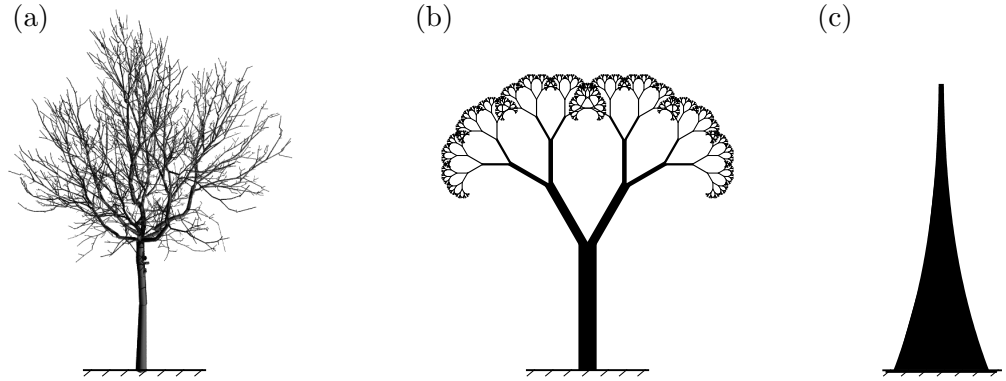

Figure 2.1: Geometries of the models used for analyzing flow-induced pruning: (a) Section 2.2: Walnut tree, as in Sinoquet *et al.* (1997); (b) Section 2.3: Idealized branched system, as in Rodriguez *et al.* (2008); (c) Section 2.4: Tapered beam, as in McMahon (1975) and Bejan *et al.* (2008).

corresponding fluid force magnitude F per unit length reads

$$F = \frac{1}{2}\rho C_D D U^2, \tag{2.1}$$

where U is the free stream velocity, ρ the fluid density, D the local branch diameter and C_D the drag coefficient (de Langre 2008, Madin & Connolly 2006). The direction is assumed to be that of the flow velocity. In order to isolate the effect of the branched geometry on the occurrence of breakage, the fluid load is here computed on leafless branches, and the influence of leaves will be discussed in Section 2.5.

This load is applied on the whole branched system, which is held by a perfect clamping at the base. The structure is brittle, as defined in Section 1.3. More precisely, the brittle behavior is introduced as follows: (i) the deformations are assumed to be negligible, so the stress state is computed on the initial configuration, without elastic reconfiguration; (ii) when increasing the flow velocity U, breakage occurs when and where the local skin stress Σ reaches the critical yield stress, Σ_c; (iii) the broken branch is then removed, and this results in a new flow-induced stress state. Flow velocity may then be further increased until a new breaking event occurs.

In the absence of deformations, and because of the high slenderness of the system, we use a standard linear beam theory to derive the stress state, essentially the bending moment M. The maximum stress in the cross-section resulting from this bending moment is the skin stress, defined as $\Sigma = 32M/\pi D^3$ (Niklas 1992, Gere & Timoshenko 1990).

By analogy with the non-dimensional fluid-load introduced in Section 1.2 for the analysis of flow-induced elastic deformations, the dimensionless number to scale the

fluid effect on the structure is the Cauchy number, defined here as

$$C_Y = \frac{\rho C_D U^2}{\Sigma_c} G, \tag{2.2}$$

where G is a geometrical factor introduced for comparison purpose and defined such that $\Sigma = \Sigma_c$ at the base of the intact structure when $C_Y = 1$. Note that this Cauchy number is similar in principle but differs from that introduced in Section 1.2.1; the critical yield stress Σ_c simply replaces here the Young modulus E. As the structure can break, there is a limit fluid velocity – or Cauchy number – at which the structure will break at its base. This corresponds to a maximum sustainable fluid velocity, and the corresponding Cauchy number will be noted C_Y^{last}. According to the scaling chosen for the Cauchy number, C_Y^{last} is equal to 1 in the absence of branch breakage.

The non-dimensional local stress is defined as $\sigma = \Sigma/\Sigma_c$ and the non-dimensional local bending moment as $m = M/M_c$, with $M_c = \Sigma_c \pi D_B^3/32$, D_B being the base diameter (Niklas 1992). This latter scaling is chosen so that breakage occurs at the base of the trunk when $m = 1$. The non-dimensional vertical coordinate z is defined using H, the height of the structure, as a reference length scale.

2.2 Flow-induced pruning of a walnut tree

The geometry of the branched system is expected to have a large influence on the stress state and thus on the location and timing of breaking events. We therefore first apply the procedure described above using the digitized geometry of an actual 20-yr-old walnut tree (*Juglans Regia L.*) described in Sinoquet *et al.* (1997) (Figure 2.1a). This tree is 7.9 m high, 18 cm in diameter at breast height (dbh); it has a sympodial branching pattern (Barthelemy & Caraglio 2007) and about eight orders of branching. Note that for this actual geometry, the different orientations of the branches with respect to the flow are taken into account; the effective fluid velocity for the fluid force is the velocity normal to the branch axis. The stress state under flow is computed using a standard finite element software (CASTEM v. 3M, Verpeaux *et al.* (1988)), and is presented in Figure 2.2a for four different branching paths.

We observe that the stress level is not uniform but shows a maximum located in the branches, which is consistent with the results of Niklas & Spatz (2000) (see Figure 1.10). Note that since the bending stress σ varies linearly with the fluid-loading C_Y, one needs only to focus on the critical situation where $\sigma = 1$ is first reached in the structure. In this tree, the criterion for breakage is satisfied first in a branch and not in the trunk. This corresponds to the mechanism of branch breakage, as defined in Section 1.3. If the fluid-loading is further increased after removal of the broken parts, successive breaking events are observed, in a flow-induced pruning sequence: Figure 2.3a shows three states of the tree at increasing Cauchy number with branches progressively removed as they break off.

During the sequence of breakage, the bending moment at the base of the tree, m_B, evolves significantly with the Cauchy number, Figure 2.3b. Up to the first breakage, the

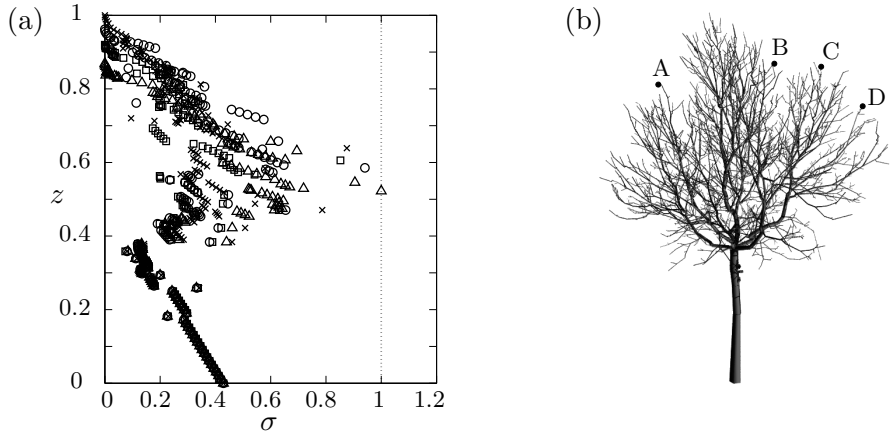

Figure 2.2: Non-dimensional stress profile $\sigma(z)$ in a tree under cross-flow. (a) Computed stress profiles along four branching paths, A ($\times$), B ($\square$), C ($\triangle$) and D ($\circ$) in the digitized tree geometry shown in (b).

moment is proportional to the fluid-loading C_Y (zone I in Figure 2.3b). Then, in a small range of load increase (zone II), all large branches are broken at an intermediate level, resulting in a significant decrease of the bending moment. Breakage then continues but to a much smaller extent (zone III), while the moment increases almost linearly up to the value $m_B = 1$ when the trunk breaks. Note that the benefit of this sequence of breaking events is that the critical value of the base moment $m_B = 1$ is reached only at $C_Y^{\text{last}} \simeq 10$ instead of 1 if there was no branch breakage. This corresponds to more than a factor of 3 on the acceptable fluid velocity. For instance, for a critical stress $\Sigma_c = 30$ MPa, which is the order of magnitude of maximum acceptable bending stresses measured in trees (Beismann *et al.* 2000, Lundstrom *et al.* 2008), the maximum sustainable fluid velocity before trunk breakage is increased from $U \simeq 20$ m.s^{-1} without branch breakage to $U \simeq 70$ m.s^{-1} with branch breakage.

To summarize, this set of computations clearly shows that branch breakage can occur prior to trunk breakage, and that the sequence of flow-induced pruning results in a significant reduction in the load applied on the base of the tree, or equivalently, an increase in the sustainable fluid velocity. To further analyze this process, we turn to a simple model in the next section.

2.3 The ideal tree model

2.3.1 Infinite branched tree

To establish the relation between the parameters of the system and the flow-induced pruning process, we simplify the problem to its essential elements: the branched geometry and the slenderness of branches; we disregard now the effect of branch orientation relative to the flow. Similarly to Rodriguez *et al.* (2008), we consider first an infinitely

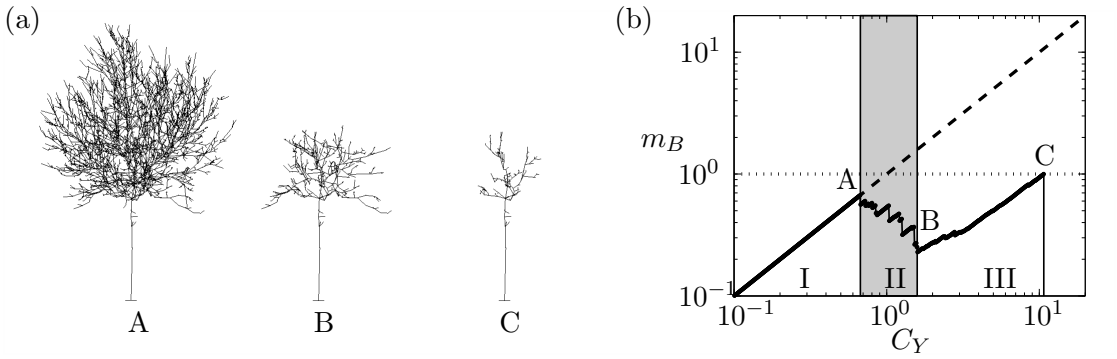

Figure 2.3: Computed sequence of branch breakage in the walnut tree: (a) A: initial tree for $C_Y \leq 0.67$; B: after breakage in large branches, $C_Y = 1.7$; C: just before trunk breakage, $C_Y = 10.7$. (b) Corresponding evolution of the bending moment at the base of the tree m_B, in three distinct ranges. The dashed line shows the moment that would exist without breakage. The dotted line shows the critical value m_B that causes trunk breakage.

iterated sympodial tree made of cylindrical branches (Figure 2.4). Two parameters only are needed to describe this ideal tree: (i) the branching ratio λ, giving the reduction of diameter through branching, and (ii) the slenderness exponent β, giving the relationship between length and diameter in branch segments of the tree, so that

$$\lambda = \left(\frac{D_{k+1}}{D_k}\right)^2, \quad \frac{D_{k+1}}{D_k} = \left(\frac{L_{k+1}}{L_k}\right)^\beta, \tag{2.3}$$

where D_k and L_k are the diameter and length of a branch segment of order k, see Figure 2.4 (Rodriguez *et al.* 2008). Typical values of these parameters are $\lambda < 1$ and $1 < \beta < 2$. Note that the number of branches emerging from a branching point is typically equal to $1/\lambda$ (Lindenmayer & Prusinkiewicz 1996). This property is usually referred to as Leonardo's rule, as it is Leonardo da Vinci who first observed in his notebooks that there was a conservation of section at a branching point (Richter & Bell 1970). Such observation implies that the sum of the section of the emerging branches is equal to the section of the mother branch.

We use now a scaling argument similar to that of Rodriguez *et al.* (2008) for the dynamics of trees. On the ideal infinitely branched system of Figure 2.4, we can compare the stress level in branch $k = 1$ (the trunk) and in branch $k = 2$. The sub-tree labeled II in Figure 2.4 is identical to the full tree, I, but for a change in length and diameter scales. All diameters (resp. lengths) in II are reduced by a factor $\lambda^{1/2}$ (resp. $\lambda^{1/2\beta}$). Let Σ_1 be the maximum skin stress in the trunk ($k = 1$) under a given fluid-loading U, and Σ_2 the maximum skin stress in the branch $k = 2$. The relations between the flow velocity and Σ_1 or Σ_2 are identical, but for the change of diameter and length scales. The dependence of the stress on diameter and length is the following: (i) Σ varies as M/D^3, where M is the bending moment, (ii) M varies as FL^2, where F is the norm of the local

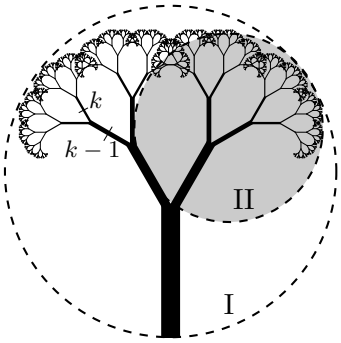

Figure 2.4: Idealized branched system: infinite iterated tree. The sub-tree II is equivalent to the whole tree I but for a change of scales.

fluid force, Equation (2.1), (iii) F varies as $\rho U^2 D$. Hence Σ varies as $\rho U^2 (L/D)^2$. We therefore may state that

$$\frac{\Sigma_2}{\Sigma_1} = \left(\frac{L_2}{D_2}\right)^2 \left(\frac{D_1}{L_1}\right)^2 = \lambda^{\frac{1-\beta}{\beta}}. \tag{2.4}$$

Since $\lambda < 1$, the condition for the stress to be higher in branches than in the trunk becomes

$$\beta > 1. \tag{2.5}$$

Here the only parameter controlling the possibility of branch breakage is the slenderness exponent, a classical parameter in the allometry of trees. As β is typically greater than 1 for trees, branch breakage is expected to occur. This simplistic approach now deserves to be improved, as the assumption of an infinite number of branching levels is very strong, and may not be compatible with the constraint that the tree area has to be finite.

2.3.2 Finite branched tree

Let us consider now the same idealized tree, but with a finite number of branching iterations (Figure 2.5). This structure has N levels, which are labeled in this section from the top to the bottom. Note that $n = N - k + 1$, where k is the label of the previous section from the base of the tree. The trunk corresponds now to the last level, N. At each level n, we define the branch diameter D_n and length L_n, which can be expressed as a function of the trunk diameter and length D_N and L_N as

$$D_n = \lambda^{\frac{N-n}{2}} D_N, \quad L_n = \lambda^{\frac{N-n}{2\beta}} L_N. \tag{2.6}$$

By a simple integration of the fluid force on the branches, the moment at the base of a branch of order n may be derived, as well as the corresponding skin stress, which is

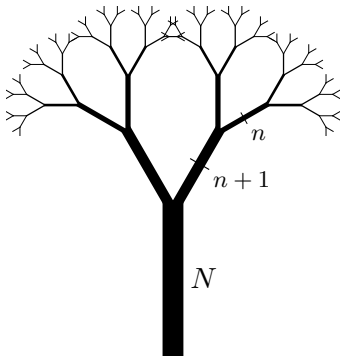

Figure 2.5: Idealized branched system: finite iterated tree and corresponding notations.

obtained in non-dimensional form as

$$\sigma_n = C_Y \lambda^{\frac{1-\beta}{\beta}N} \left(A\lambda^{\frac{\beta-1}{\beta}n} + B\lambda^{\frac{n}{2}} + C\lambda^{\frac{\beta-1}{2\beta}n} \right), \tag{2.7}$$

where the Cauchy number C_Y is defined as

$$C_Y = \left[\frac{8}{\pi} \left(\frac{L_N}{D_N} \right)^2 \right] \frac{\rho C_D U^2}{\Sigma_c}, \tag{2.8}$$

and A, B and C are functions of β and λ only. The detailed derivation of Equation (2.7) as well as the expression of A, B and C can be found in Appendix A.2.

A systematic numerical exploration of the (λ, β) parameter space shows that when $\beta < 1$ the stress always increases from top to bottom (Figure 2.6a). Conversely, for $\beta > 1$, the stress reaches a maximum at branch level n_c and then decreases from top to bottom, provided that $N > n_c$, where n_c depends on λ and β. This dependence is given in Figure 2.6b. This analysis with a finite tree model gives a criterion consistent with that of the infinite tree model, namely $\beta > 1$. Moreover, the other parameter, λ, is found to affect only the location of possible breakage. This suggests that branching is not a key factor in the occurrence of trunk or branch breakage. In the next section we explore a simpler model of the slenderness effect.

2.4 The slender cone model

2.4.1 Flow-induced stress

The simplest model that allows one to take into account a relation between diameters and lengths through a slenderness exponent is a cone. This formulation is related to MacMahon and Kronauer's equivalent geometry of a tree, a tapered beam with a rectangular cross-section of dimensions varying as power laws of the height (McMahon 1975, McMahon & Kronauer 1976).

The geometry considered here is a slender cone with a circular cross-section, Figure

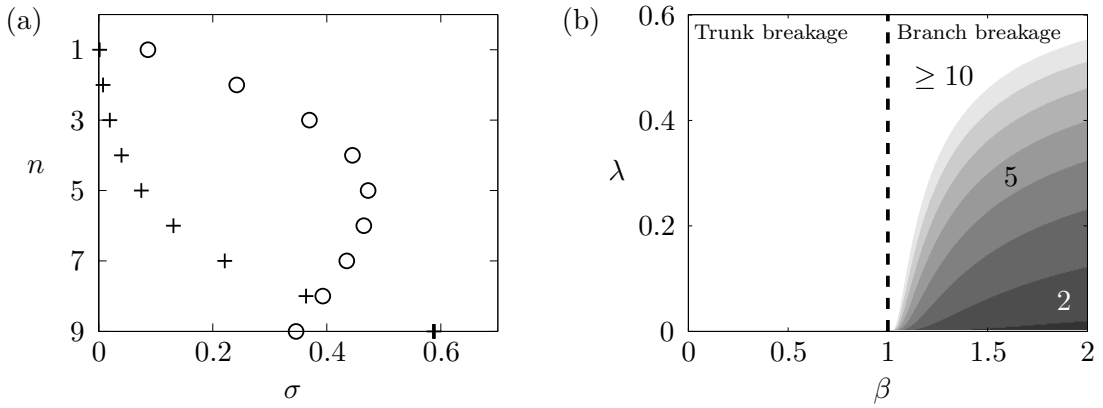

Figure 2.6: (a) Stress profile in an idealized tree model under uniform cross-flow for two values of the slenderness exponent: $\beta = 0.75$ (+) and $\beta = 1.5$ (∘), and the branching parameter $\lambda = 0.3$. The symbols correspond to the maximum stress at each branch level n. (b) Location of the maximum of stress as a function of β and λ. The location is given in the form of the number of branching levels counted from the top of the tree, Figure 2.5. For $\beta \leq 1$, breakage occurs directly at the base of trunk.

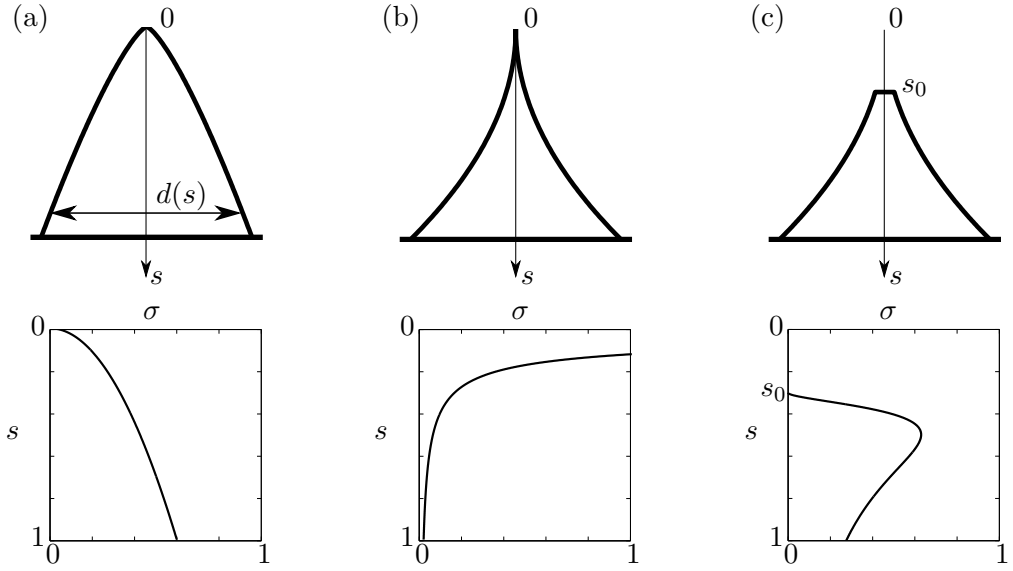

Figure 2.7: The slender cone model: geometry and stress profile under uniform cross flow. (a) cone with $\beta < 1$ (here 0.75), showing a maximum of stress at the base; (b) cone with $\beta > 1$ (here 2), showing a maximum at the top; (c) cone truncated arbitrarily at $s_0 = 0.3$ showing a local maximum.

2.7a, and we follow the same mechanical approach as for the previous geometries. Let H be the cone height, $d_B = D_B/H$ the dimensionless diameter at the base and s the vertical coordinate which is oriented downwards in this section, as opposed to the height z introduced previously. The cone dimensionless diameter is given by

$$d(s) = d_B s^{\beta}. \tag{2.9}$$

Using the same formulation as in the previous section, the stress state along the cone is obtained as

$$\sigma(s) = C_Y s^{2(1-\beta)}, \tag{2.10}$$

where the Cauchy number is defined here as

$$C_Y = \left[\frac{16}{(1+\beta)(2+\beta)\pi d_B^2}\right] \frac{\rho C_D U^2}{\Sigma_c}. \tag{2.11}$$

From Equation (2.10), we readily observe that for $\beta = 1$, the constant stress case of Bejan *et al.* (2008) is found. Otherwise, for $\beta < 1$ the stress increases with s and is therefore maximum at the base, as sketched in Figure 2.7a, whereas for $\beta > 1$ the stress decreases with s, and the maximum, discussed further, is not at the base, Figure 2.7b-c. These results are consistent with the condition for branch breakage in the previous section.

Note that the expression of the Cauchy number in Equation (2.11) provides a physical interpretation of the Cauchy number. It is in fact the ratio between the flow-induced bending moment at the base M_B and the critical bending moment M_c, which scale respectively as

$$M_B \sim \rho C_D U^2 D_B H^2, \quad M_c \sim D_B^3 \Sigma_c. \tag{2.12}$$

The Cauchy number represents therefore the fluid effect on the structure with respect to breakage, similarly to the elastic Cauchy number introduced in Section 1.2.1.

In order to avoid the singular case of infinite stress at $s = 0$ for $\beta > 1$, we use a cone truncated at $s = s_0$, Figure 2.7c. The truncation s_0 corresponds to the first breakage occurring as soon as $U \neq 0$; its value is chosen arbitrarily. The corresponding stress state is then

$$\sigma(s) = C_Y \left[s^{2(1-\beta)} - (2+\beta)s_0^{1+\beta} s^{1-3\beta} + (1+\beta)s_0^{2+\beta} s^{-3\beta}\right], \tag{2.13}$$

which reduces to Equation (2.10) when $s_0 = 0$. The detailed derivation of this equation is given in Appendix B. For $\beta > 1$, the stress shows a maximum before decreasing downwards, as illustrated in Figure 2.7c. The limit case $s_0 = 0$ is in fact equivalent, in the ideal tree model of Section 2.3, to the limit as N goes towards infinity, which would lead to a vanishing diameter at the tip. There is therefore an analogy between the cone truncation and the ideal tree with a finite number of branching levels.

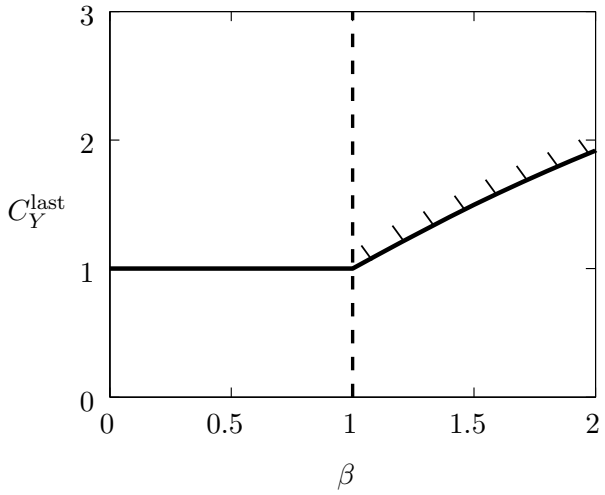

Figure 2.8: Maximum fluid load that the cone can support as a function of the slenderness exponent. Note that for $\beta > 1$ the curve is the lower bound of all possible evolutions.

2.4.2 Sequence of breaking events

Considering now the generic case of the truncated cone, Figure 2.7c, we analyze the sequence of breaking events resulting from an increasing fluid-loading C_Y. The stress σ increases linearly with C_Y up to the point where its maximum value reaches the limit of breakage, $\sigma = 1$. This defines the first breaking event at $C_Y = C_Y^1$ occurring at $s = s_1$. It results in a new truncated cone, and the process is repeated as C_Y is further increased. Eventually, when the cone becomes truncated close to the base, the maximum stress may be reached at the base itself, resulting finally in base breakage. Note that the stress state follows a self similar evolution with the truncation height, and the location of breakage s_1/s_0 is only a function of β (see details in Appendix B.2.2). This property is analogous to the breakage location in the finite ideal tree model of Section 2.3.2: n_c, counted from the top, is only a function of the geometric parameters.

This sequence of breaking events may be analyzed in terms of the maximum acceptable fluid-loading C_Y^{last}. As illustrated in Figure 2.8, this is strongly dependent on β. When $\beta < 1$, the first breaking event is at the base so that $C_Y^{\text{last}} = 1$. Conversely when $\beta > 1$, breaking occurs progressively as C_Y is increased, and the base breakage is delayed, $C_Y^{\text{last}} > 1$. The precise value of C_Y where the base breaks depends on the initial truncation s_0, but is always higher than a lower bound that can be computed from Equation (2.13), which is shown in Figure 2.8. We observe a significant increase of the ability of the system to sustain fluid-loading when $\beta > 1$.

In terms of base moment, the sequence of breaking events can be easily computed, Figure 2.9. For $\beta < 1$ the base moment increases linearly with C_Y until base breakage occurs, $m_B = 1$ for $C_Y = 1$. For $\beta > 1$ the sequence of breaking events results in sudden drops in base moment followed by linear increase up to the next breaking, as illustrated in Figure 2.9. Since the sequence of breaking events is a discrete process that depends

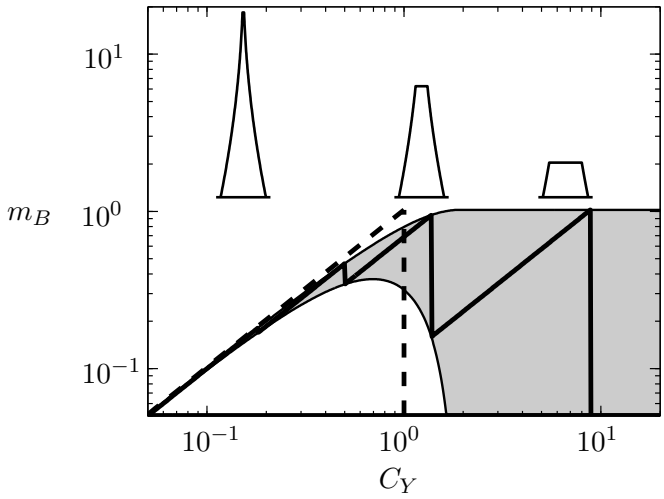

Figure 2.9: Moment at the base of the cone as the fluid-loading is increased. (- - -) direct base breakage occurring when $\beta < 1$; (—) progressive breaking for $\beta > 1$ (here $\beta = 2$). The shaded region shows all possible values depending on the initial truncation z_0. The cone state for $\beta > 1$ is shown for three values of C_Y.

on the initial truncation s_0, there exists, for a given Cauchy number C_Y, a wide range of acceptable cone heights and thereby a wide range of corresponding base moments. In practice, for all possible values of s_0, the evolution of m_B remains bounded between its values for the shortest and highest cone that can exist at each Cauchy number. This is represented by the shaded region in Figure 2.9. Some additional informations on the determination of the envelopes defining the shaded region are provided in Appendix B.2.2.

These results show that the simple cone model contains the key elements to understand the effect of geometry on (i) the stress profile, (ii) the sequence of breaking events and (iii) the consequences on the evolution of base load when the fluid velocity is increased. Here again, the essential criterion concerns the slenderness exponent β.

2.5 Discussion and conclusions

Starting from the case of a full walnut tree geometry, we have used models of increasing simplicity. This allowed us to point out the role of various parameters on the process of breakage under fluid-loading. The first issue that had to be addressed was that of the flow-induced stress distribution. As noted by other authors, the stress is not necessarily maximum at the base (Niklas & Spatz 2000, Bejan *et al.* 2008). In the walnut tree of Section 2.2, the stress has a local maximum at about mid height. Using the ideal tree model in Section 2.3, we have shown that the existence of this maximum is related to the value of the slenderness exponent, β, being larger than one: in fact this allometry parameter is about 1.37 for this particular walnut tree (Rodriguez *et al.* 2008). Following

Bejan *et al.* (2008), we recover the critical value of $\beta = 1$ for a uniform stress profile in the simplest model, that of a cone in Section 2.4.

Actually, some refinement is needed here to understand the precise location of the maximum of stress. We have shown in Section 2.3 that the location of this maximum was also dependent on the branching parameter λ, in the form of the parameter n_c, which is the number of branching levels from the top to this maximum point. For our walnut tree, where $\lambda \simeq 0.25$, we obtain $n_c = 6$ using Figure 2.6. This is smaller than the total number of branching levels in the walnut tree which is about 8 (Sinoquet *et al.* 1997). A local maximum of stress is therefore expected in the branches, and is actually observed in Figure 2.2.

The second issue was that of the sequence of breaking events occurring when the fluid-loading C_Y is increased. Using a brittle fracture model for the walnut tree in Section 2.2, we have shown that most large branches broke in a short range of flow velocity, and that breakage of the trunk occurred at much higher flow velocity. The large size of broken branches can be explained by the value of $n_c = 6$ found above. All large branches do not break exactly at the same value of the Cauchy number. This is due among other reasons to some variability in the allometry parameters λ and β within the tree. It can also be explained by the different branch orientations within the tree, as it will be discussed in Section 3.3.2 in the next Chapter. Once all large branches are broken, the remaining tree shape, C in Figure 2.3a, does not have enough branching levels to have a local maximum in the branches, and the next breaking event occurs at the base of the trunk. Note that the process of branch breakage in the walnut tree allowed the tree to have a much larger acceptable Cauchy number before breakage of the trunk. This can also be analyzed using the cone model as in Section 2.4, where the critical Cauchy number for base breakage is clearly dependent on β (Figure 2.8).

The third issue was that of the evolution of the load at the base of the tree. For the walnut tree, Figure 2.3b, the sequence of successive breakage of the large branches results in a significant decrease of the flow-induced moment at the base. This can be understood using the cone model, where the sequence of breaking event and corresponding drops of base moment can be tracked, Figure 2.9. We may therefore state that the essential characteristics of branch breakage and corresponding load evolution in the walnut tree can be understood using our simple ideal tree model and cone model.

The analytical results of Sections 2.3 and 2.4 were obtained considering that all parameters have self-similar variations. However, this was not the case for the walnut tree computations of Section 2.2, which suggests that the behaviors pointed out in this study can be generalized to structures that do not necessarily have self-similar variations of their parameters. Moreover, the ideal tree and cone models can be easily extended to incorporate other features of the problem, such as a dependence of all parameters with s: the flow velocity U, the material properties through the critical parameter Σ_c, and even the drag coefficient C_D, which allows one to take easily into account the additional drag of leaves. This results in modified criteria for branch breakage, which involve then β and the corresponding parameter related to the additional s-dependence.

Considering the simplicity of the criterion that we have found for branch breakage,

Ref.	Tree	Slenderness exponent β	Branching parameter λ	Total orders of branching N	Predicted branch breakage level n_c	Predicted breakage type
Sinoquet *et al.* (1997) Rodriguez *et al.* (2008)	Walnut Tree *Juglans Regia L.*	1.37	0.25	> 8	6	Branch
McMahon & Kronauer (1976)	Red Oak *Quercus Rubra*	1.51	0.41	> 6	7	Branch or trunk
- -	White Oak 1 *Quercus Alba*	1.41	0.28	> 6	6	Branch
- -	White Oak 2 *Quercus Alba*	1.66	0.29	> 6	5	Branch
- -	Poplar Tree *Populus Tremoloides*	1.5 (estimated)	0.29	> 6	5	Branch
- -	Pin Cherry *Prunus Pensylvanica*	1.5	0.24	> 4	5	Branch or trunk
- -	White Pine *Pinus Strobus*	1.37	0.24	> 5	5	Branch

Table 2.1: Predicted breakage type using the results of Section 2.3. Branch breakage is predicted when $n_c \leq N$.

we can test whether it is generally satisfied. McMahon & Kronauer (1976) have noted that β is usually larger than 1 and typically around 1.5, while λ is typically close to 0.25. This leads to a maximum stress located at a branching level $n_c = 5$ counting from top down. This is clearly in the branches as trees generally have more than 5 orders of branching. We may therefore state that branch breakage can be expected in most sympodial trees. This is illustrated in Table 2.1, where the values of parameters are given for several trees. Bertram (1989) measured the values of the slenderness exponent on a silver maple (*Acer saccharinum*), and noted that peripheral branches have a slenderness exponent β of 1 or less than 1, whereas the non-peripheral ones have a value around 1.5. This interesting property suggests that not all elements in a tree will undergo the same type of reconfiguration under flow. This idea will be discussed further in the next Chapter when the different reconfiguration strategies will be considered.

Clearly the possibility of branch breakage is favorable in terms of survival of an individual tree in the face of extreme fluid-loading. It may also be favorable in terms of tree development by removing the less vigorous branches. The question then arises as to whether this implies new constraints on the geometry of the tree. It appears from our results that the constraint $\beta > 1$ is not incompatible with other constraints such as the optimal resistance to buckling under gravity, which requires $\beta = 3/2$ (McMahon 1975). The same result was obtained considering the wind effect on trees but for an overcrowded tree canopy (Larjavaara 2010). Similarly $\beta > 1$ is compatible with a constraint for optimal dissipation, that modal frequencies have a ratio of less than two, requiring that $\beta > 1$ for $\lambda = 0.25$ (Rodriguez *et al.* 2008, Theckes *et al.* 2011).

The particular case of branched corals (Madin 2005, Tunnicliffe 1981, Highsmith 1982) is somewhat different. The segments are similar in length and diameter, so that $\lambda \simeq 1$ and $\beta \simeq 1$ in our variables, but with a number of branches emerging from one branching not equal to $1/\lambda$. An analysis similar to that of Section 2.3 shows that breakage is expected at the bottom. This is the case in most isolated corals.

More generally we may place these results in the overall context of reconfiguration, as introduced by Vogel (1989). This originally referred to the reduction of loading made possible by elastic deformation. For a plant, it is a crucial mechanism to survive heavy fluid-loading. But plant tissues are not all very elastic, and plant parts are not all very flexible. Our results on the role of branch breakage in reducing the loads show that, in parallel with elastic reconfiguration, there exists a mechanism of brittle reconfiguration. There are therefore two distinct strategies to overcome critical events. The first is evidently reversible in the short term by elasticity. The second is also reversible by re-growth, but only in the long term. Thus flow-induced pruning is possibly a widespread mechanism in plants or benthic organisms that support heavy loading by the surrounding fluid environment.

A question then arises about the robustness of this reconfiguration mechanism when the deformations before breakage become significant. The issue of the combination of deformation and breakage is now investigated in the next Chapter.

Chapter 3

Combination of bending and pruning reconfiguration strategies

In addition to the traditional reconfiguration by elastic deformation, a second reconfiguration strategy has been identified in the previous Chapter. This second strategy, which we will refer to as reconfiguration by pruning, was studied in the absence of elastic reconfiguration – reconfiguration by bending. While the bending strategy is common to any deformable structure, be it a linear elastic material or not, pruning is related to tapered geometries, therefore reducing the range of application of this kind of reconfiguration to specific geometries.

The actual mechanical behavior of a plant under external flow being a combination of deformation and breakage, a question remains about the effect of coupling bending and pruning strategies on drag reduction and survival. Indeed, one can expect deformations to modify the stress state leading to breakage. We are therefore interested in the effect of deformations on reconfiguration by pruning, in order to understand the different reconfiguration strategies that exist in plants.

After presenting the mechanical model used for studying the combination of deformation and breakage under flow in Section 3.1, the reconfiguration of the ideal cone model introduced previously is studied in Section 3.2. The results will then be extended to more elaborate geometries representing realistic plants (Section 3.3). Finally, a discussion and conclusions are given in Section 3.4.

3.1 Model

3.1.1 Mechanical model

Throughout this Chapter, we place ourselves in a similar scenario as that of the pruning study in Chapter 2, by considering a uniform cross flow over the entire structure, not affected by the presence of the solid body, in the two-dimensional case. The main difference here relies on the fact that the structure can now deform significantly. For this study, we consider first the simplest model that has the key characteristics for both

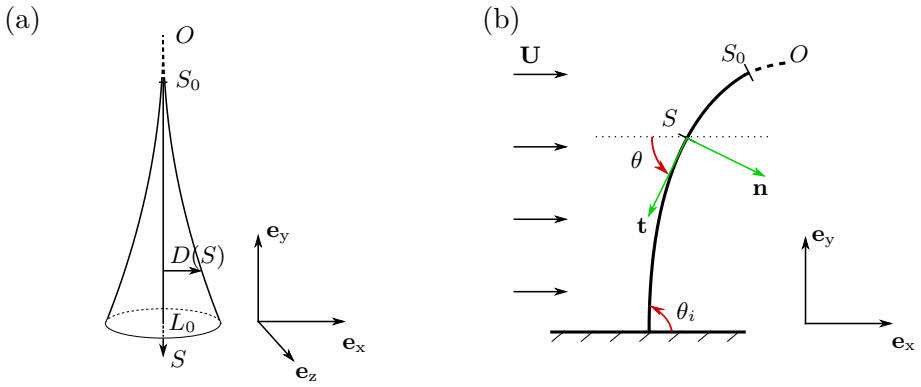

Figure 3.1: Cone model and parametrization: (a) Cone without flow; (b) Cone axis under flow and parameters of the beam description.

reconfiguration strategies, an elastic slender cone model. The general parametrization is shown in Figure 3.1. As the deformations of the body will not be negligible, we introduce a local referential $(\mathbf{t}, \mathbf{n})$, and the curvilinear axis is oriented downwards as in Section 2.4. The cone diameter reads here

$$D(S) = D_0 \left(\frac{S}{L_0} \right)^{\beta}, \tag{3.1}$$

where D_0 is the base diameter, L_0 the cone length, S the curvilinear coordinate and β the slenderness exponent (positive).

The external fluid force that is applied on the structure results from a normal pressure drag oriented along the normal to the branch axis,

$$\mathbf{F} = \frac{1}{2} \rho C_D \left[U \sin\theta(S) \right]^2 D(S) \mathbf{n}, \tag{3.2}$$

where ρ is the fluid density, U the fluid velocity, $\theta(S)$ the local orientation of the cone axis and C_D the drag coefficient. Similarly to the previous analysis, the high slenderness of the cone allows us to consider a standard Euler-Bernoulli beam theory. In the two-dimensional case, the equations for the shear force $\mathbf{V}$ and the bending moment M read

$$\frac{\mathrm{d}\mathbf{V}}{\mathrm{d}S} + \mathbf{F} = \mathbf{0}, \quad \frac{\mathrm{d}M}{\mathrm{d}S} + V = 0, \quad EI \frac{\mathrm{d}\theta}{\mathrm{d}S} - M = 0, \tag{3.3}$$

where E is the Young modulus and I the second moment of inertia in the bending direction (Gere & Timoshenko 1990, Salençon 2001). The moment of inertia reads $I = \pi D^4/64$ for a cone with circular cross-section. The cone is held by a perfect clamping at its base ($\theta(S = L0) = \pi/2$) and free at the top; the free angle $\theta(S = S_0)$ is therefore unknown. The truncation at S_0 is introduced consistently with the analysis of Section 2.4.2. As for the pruning analysis, the breakage criterion relies on the bending stress Σ

compared to the critical yield stress Σ_c; the bending stress reads

$$\Sigma = \frac{MD}{2I} = \frac{32M}{\pi D^3}. \tag{3.4}$$

Finally, the breaking sequence is dealt as in Chapter 2.

3.1.2 Non-dimensional parameters

The Euler-Bernoulli Equations (3.3) can be expressed in a non-dimensional form, by using as reference length scale the cone length L_0 and reference force and moment EI_0/L_0^2 and EI_0/L_0 respectively, where I_0 is the second moment of inertia at the base of the cone. According to these notations, by considering the shear force decomposition on the $(\mathbf{t}, \mathbf{n})$ referential, V_t and V_n, the non-dimensional equations read

$$v_n' + \theta' v_t + (1+\beta)(2+\beta) C_Y \varepsilon_c \sin^2\theta s^\beta = 0, \tag{3.5}$$
$$v_t' - \theta' v_n = 0, \tag{3.6}$$
$$\theta'' + 4\beta s^{-1}\theta' + s^{-4\beta} v_n = 0, \tag{3.7}$$

where the lower-case letters correspond to non-dimensional quantities, and $'$ denotes the derivative with respect to the non-dimensional curvilinear coordinate s. More details about the non-dimensionalization are provided in Appendix B. The scaling term that appears in Equation (3.5) is intentionally decomposed into two non-dimensional parameters which read

$$C_Y = \frac{16}{(1+\beta)(2+\beta)\pi}\left(\frac{L_0}{D_0}\right)^2 \frac{\rho C_D U^2}{\Sigma_c}, \quad \varepsilon_c = 2\frac{L_0}{D_0}\frac{\Sigma_c}{E}. \tag{3.8}$$

With this decomposition, the Cauchy number C_Y is the same as that introduced in Chapter 2; note that the parameter d_B in Equation (2.11) is replaced here by D_0/L_0. The interpretation of the second non-dimensional parameter ε_c results from the scaling of the strain in a beam when its reconfiguration through bending is important. In that case, the beam is bent along its entire length, and its curvature is of order $1/L$. The resulting strain scales then as the beam radius multiplied by the curvature, $D/2L$. On the other hand, the ratio Σ_c/E is the strain at breakage. The non-dimensional number ε_c is thus a normalized critical strain, i.e. the ratio between the strain at breakage and the strain when bending becomes important. For commodity, ε_c will be referred to as the critical strain in the following.

This parameter ε_c is therefore the relevant one for characterizing the structure reconfiguration strategy. Indeed, if the critical strain ε_c is much lower than 1, the structure will break while the bending effect is negligible, whereas if it is much greater than 1 breakage will occur at very large deformations. We see therefore that pruning corresponds to the limit when the critical strain tends to zero, and bending when ε_c tends to infinity.

In order to have a common framework between bending and pruning, the repre-

sentation chosen here for the load evolution under flow is that of the reconfiguration curves $\mathcal{R}(C_Y)$ as introduced in Section 1.2. The reconfiguration number corresponds to the actual drag normalized by the drag the same body would experience if it were not deformable, and in this case, also not breakable. As this is a purely theoretical and numerical study, there is no Reynolds effect while increasing the fluid velocity, which would modify the drag coefficient. Therefore, the reference drag of a non-reconfigurable body is proportional to the Cauchy number. Note that this framework differs from that of Chapter 2 since we considered then the evolution of the base bending moment instead of the drag. As we consider here large deformations, there is no analytical solution to the non-dimensional Euler-Bernoulli equations (3.5), (3.6) and (3.7). The system is therefore solved numerically using a standard Runge-Kutta algorithm and a shooting method for the free angle at the top, as in Gosselin *et al.* (2010).

3.2 Bending and pruning of a slender cone

We consider in this section the general reconfiguration of the elastic slender cone of Figure 3.1. Since it was shown in Section 2.4 that in the pruning limit the cone will break at $s_0 > 0$ as soon as the Cauchy number is non-zero, we consider here a truncated cone. In order to keep a general description for a model geometry, we first consider that s_0 can take random values, but satisfies $s_0 \ll 1$ (in non-dimensional coordinates).

3.2.1 Particular cases

Condition for pruning

It was established in Chapter 2 that flow-induced pruning can occur only if the slenderness exponent of the structure β is greater than 1. Since this condition was found in the non-deformable case, a question arises as to whether this condition still holds when the structure can undergo significant deformations. We address this question first by solving the problem for different values of the slenderness exponent.

The flow-induced stress profile is computed for two values of the slenderness β in Figure 3.2. We readily observe that when $\beta < 1$ the stress is maximal at the base of the structure, whereas it reaches a maximum in the structure when $\beta > 1$ (Figure 3.2a and b). This result shown for two particular values of β is in fact recovered for any values of the slenderness exponent greater than 1. Thus, a remarkable result is that the condition on β holds, i.e. the stress reaches a maximum within the structure for $\beta > 1$ (see Figure 2.7 for comparison). However, one can note that the location of this maximum is now dependent on the Cauchy number (Figure 3.2b and c). This was not the case for the pruning analysis, where the deformations were considered to be negligible. We see here an important effect of bending which moves the location of the maximum stress to the bottom as the Cauchy number is increased.

As the location of the maximum stress is Cauchy-dependent, there is a limiting Cauchy number above which breakage will occur at the base even if the slenderness β is greater than 1. In other words, if the critical strain is high enough, breakage will occur

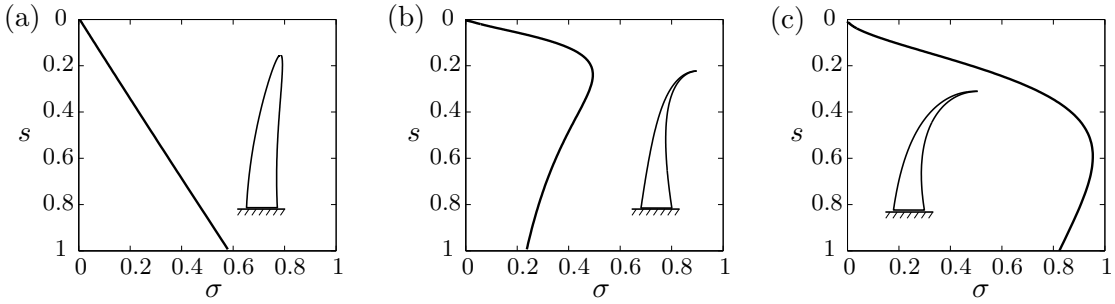

Figure 3.2: Flow-induced non-dimensional stress σ along the cone axis for two values of the slenderness exponent β: (a) $\beta = 0.5$, (b) $\beta = 1.5$. (c) Stress profile in the cone $\beta = 1.5$ at a higher Cauchy number.

at the base of the structure. One can therefore point out a condition on the critical strain for pruning. The maximum stress in the cone increases with the Cauchy number; its value when it is first located at the base corresponds to a limit value for the critical yield stress, or equivalently for the critical strain. If the critical strain ε_c is greater than this value, noted $\varepsilon_c^{\text{prun}}$, breakage will occur at the base. We have therefore a second necessary condition for pruning

$$\varepsilon_c < \varepsilon_c^{\text{prun}}, \tag{3.9}$$

where $\varepsilon_c^{\text{prun}}$ is the minimum value of the critical strain so that the maximum of stress is reached at the base of the cone. The stress profile is dependent on the slenderness β, hence the limit value $\varepsilon_c^{\text{prun}}$ is also dependent on the slenderness exponent, as shown in Figure 3.3. One can readily observe that $\varepsilon_c^{\text{prun}}$ tends to 0 as β tends to 1; indeed, there is no pruning if β is lower or equal to 1. For higher values of β, $\varepsilon_c^{\text{prun}}$ is of order 1; this validates the scaling of the critical strain in Equation (3.8).

To summarize, in addition to the geometrical condition for pruning found in the absence of deformations, a second necessary condition for pruning is identified; this condition characterizes the mechanical properties of the body. This threshold value gives an important information on the reconfiguration strategy: for lower values of the critical strain pruning can occur, whereas for higher values only bending can be observed.

Reconfiguration curves

We consider now the reconfiguration of a cone satisfying the geometrical condition for pruning, namely $\beta > 1$ (here $\beta = 1.5$), in order to investigate the effect of bending on the reconfiguration process. As stated above, the parameter characterizing the type of reconfiguration is the critical strain ε_c. Therefore, we first look at the reconfiguration curves of the cone at low, medium, and high critical strain ε_c, for different truncations of the cone (Figure 3.4).

We observe different behaviors depending on the value of the critical strain ε_c. For low

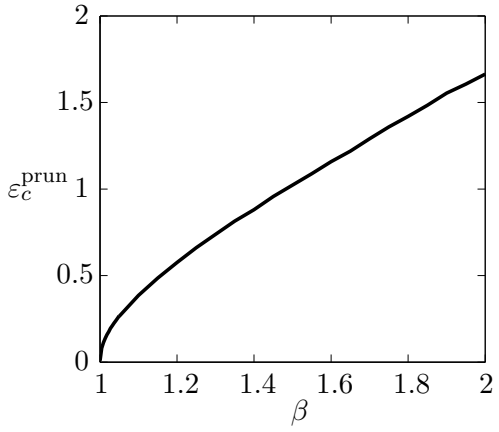

Figure 3.3: Limit value of the critical strain $\varepsilon_c^{\text{prun}}$ for base breakage as a function of the slenderness exponent β. For higher values of the critical strain, only base breakage is observed under an increasing flow.

values of ε_c, the pruning reconfiguration is recovered, and it is not affected by bending. When the critical strain is of order 1, which corresponds to the limit value $\varepsilon_c^{\text{prun}}$ for that cone, bending becomes important; both bending and pruning can be observed. Finally, for high values of ε_c, there is no pruning, only bending is observed; a single breaking event occurs at the base, defining the limit value for the Cauchy number C_Y^{last} at which the structure is entirely broken.

A first result is that pruning reconfiguration holds at low deformation, and in this case we recover a similar behavior than in the pruning limit studied previously, up to $\varepsilon_c \sim 0.5$. As expected from the results of the previous Chapter, the truncation s_0 plays a significant role in the reconfiguration by pruning. However, once the deformations are large enough, this effect is no longer visible, and the different curves merge into one single curve.

When the critical strain is of order 1, one can observe a combination of bending followed by pruning as the Cauchy number increases. It seems therefore that the two strategies can be observed in this case, albeit with little drag reduction due to bending. In the cone model this situation appears to be observable in a narrow range of the critical strain ε_c, between the critical strain at which the effect of s_0 is no longer visible and $\varepsilon_c^{\text{prun}}$. The critical strain at which the reconfiguration curves are not dependent on s_0 (Figure 3.4 b) is in fact dependent on the choice of the maximal value for s_0 (see Appendix B.3.2 for details). Hence this particular threshold is more likely to be a singularity of the model rather than a relevant parameter. The cone model appears to give a poor insight of this region where both bending and pruning are observable; this will be discussed further with more elaborate models in Section 3.3.

Since these curves show complex behaviors depending on the different parameters of the problem, we will focus now on characterizing the general pattern of reconfiguration, first by describing the asymptotic reconfiguration regimes found in the limits of low and

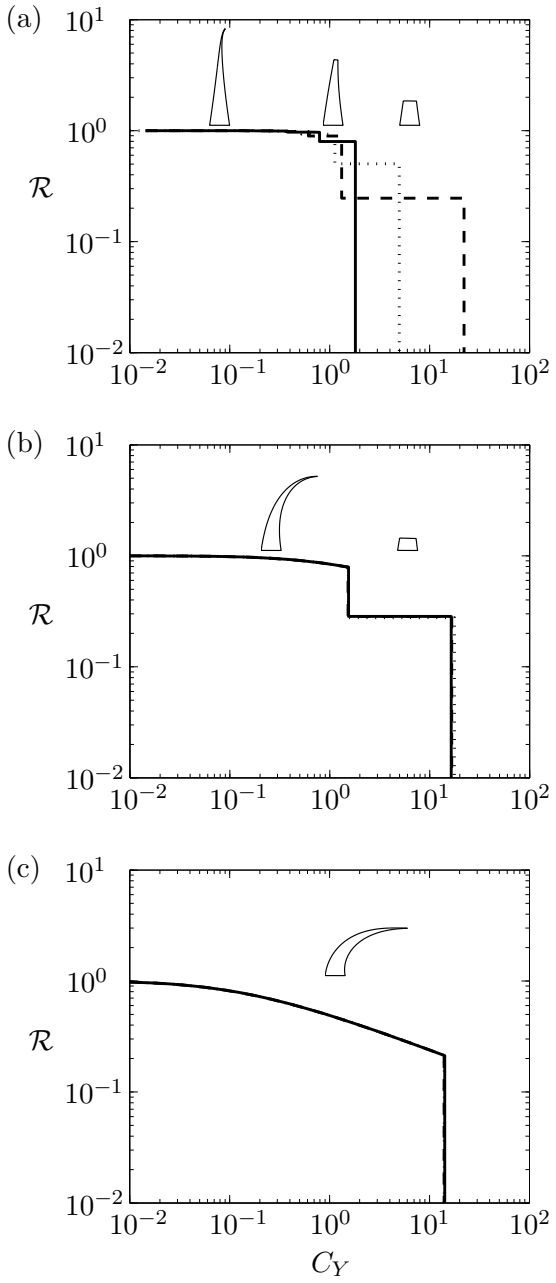

Figure 3.4: Reconfiguration number as a function of the Cauchy number for different values of the critical strain: (a) $\varepsilon_c = 0.1$, (b) $\varepsilon_c = 1$ and (c) $\varepsilon_c = 10$. The different curves correspond to different truncations: $s_0 = 0.02$ ($\cdots$), $s_0 = 0.035$ (- - -) and $s_0 = 0.05$ (—).

high critical strain, and then by considering the overall gain of reconfiguration.

3.2.2 The scaling of drag reduction for the limit strategies

For a better understanding of the drag reduction resulting from pruning and bending, we consider the limits of pruning and bending only. In order to remove the dependency on s_0 observed at low ε_c, we consider, at a given Cauchy number, the maximum drag obtained by varying s_0. This leads to the upper envelope curve presented in Figure 2.9, but computed here for the drag instead of the bending moment. For high values of the critical strain ε_c, this dependency vanishes, therefore we compute the reconfiguration curve directly for a given truncation $s_0 \ll 1$. Note that in the bending limit, the yield stress is not relevant in the reconfiguration process. We consider therefore a rescaled Cauchy number noted $\widetilde{C_Y}$. For the limit behaviors, the two Cauchy numbers are strictly equivalent; more details about the scaling of the equations in the bending limit are provided in Appendix B.

The two limit reconfiguration curves are plotted in Figure 3.5. These curves show significant drag reduction once reconfiguration is occurring. It is remarkable that in both cases an asymptotic regime is clearly visible, and scaling laws for the drag reduction by reconfiguration by pruning or bending can be found.

In the pruning asymptotic regime (Figure 3.5a), the length of the cone is reduced by the breaking events as the Cauchy number is increased. Once this length is small enough compared to the initial length, we can consider that the tapering effect is lost; indeed, the variations of diameter occur on a length equal to the cone initial length. If we consider a non-tapered beam, the drag scales as $C_Y D_0 L$, the bending moment as $C_Y D_0 L^2$ and the maximum non-dimensional stress σ as $C_Y L^2/D_0^2$. The maximum drag is obtained for the highest cone, i.e. the largest value of L so that the bending stress reaches its limit value $\sigma = 1$. This leads to $L \propto D_0 C_Y^{-1/2}$. We find therefore the scaling for the maximum drag in the pruning scenario,

$$\mathcal{R}_{\text{pruning}} \sim \frac{C_Y D_0 L}{C_Y D_0 L_0} \propto C_Y^{-1/2}, \tag{3.10}$$

which is verified numerically in Figure 3.5a. This scaling is independent of the value of the slenderness exponent β, provided it is greater than 1 (necessary condition for pruning).

We can note that the scaling law found for pruning is equal to that resulting from the perfectly plastic limit of a non-linear elastic model (de Langre *et al.* 2012). In that case, the stress reads $\Sigma = A\varepsilon^{1/N}$, where ε is the strain, and the perfectly plastic limit corresponds to the limit $N \to \infty$. The analysis in de Langre *et al.* (2012) leads to a scaling law for the drag which is a function of the parameter N; the corresponding Vogel exponent reads

$$\nu = -\frac{2N}{2N+1}. \tag{3.11}$$

In the limit $N \to \infty$, this is identical to that of Equation (3.10). In fact, there is

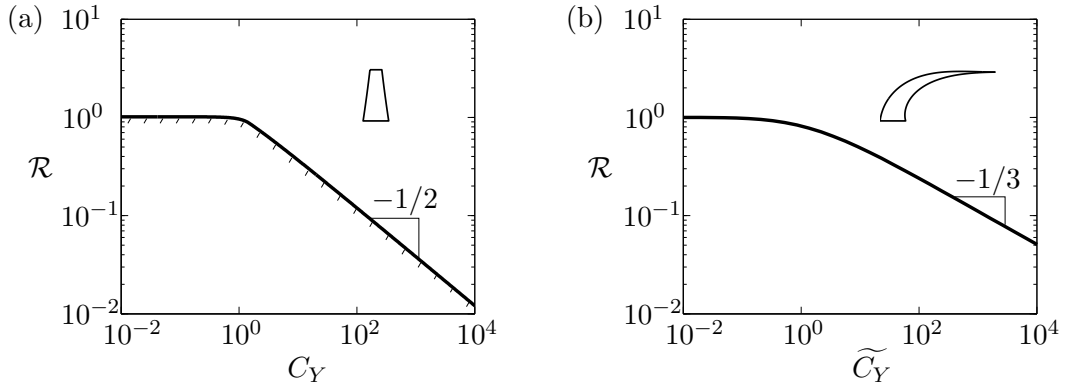

Figure 3.5: Reconfiguration curves of the slender cone model: (a) pruning limit, $\varepsilon_c \to 0$ and (b) bending limit, $\varepsilon_c \to \infty$. In the pruning limit, the curve is an upper bound of the reconfiguration number, whereas in the bending limit the curve represents the exact evolution of the reconfiguration number.

an analogy between a brittle behavior and a perfectly plastic one, when there are no tangential forces on the cone due to the fluid. In the brittle case, the upper part of the body is removed, and in the perfectly plastic case it is fully bent and aligned with the flow, thereby not contributing to the drag either. The limit $N \to \infty$ for the non-linear elastic model can be seen as a continuous approach of the brittle behavior.

The scaling for drag reduction by bending can be understood using an argument similar to that used for pruning: in the highly reconfigured state, the beam length no longer plays a role in scaling the flow-induced drag. This is in fact the same argument than that used in the dimensional analysis in Gosselin *et al.* (2010). Similarly to the pruning asymptotic analysis, one may assume therefore that in the highly reconfigured state the tapering should no longer affect the drag, leading to a scaling independent of β. The dimensional analysis is then identical to that of Gosselin *et al.* (2010), and leads to

$$\mathcal{R}_{\text{bending}} \propto \widetilde{C_Y}^{-1/3}. \tag{3.12}$$

This scaling is verified numerically, in Figure 3.5b.

Two important results are obtained here in the pruning and bending limit. The first one is the existence of an asymptotic reconfiguration regime at high Cauchy number in both cases. Moreover, the slenderness exponent β does not affect these asymptotic regimes, be it by pruning or bending. The second result is that pruning leads to a stronger drag reduction than bending. In terms of drag dependence with the flow velocity, the scaling laws found above lead to a drag linear with U for pruning (Vogel exponent $\nu = -1$), and proportional to $U^{4/3}$ for bending ($\nu = -2/3$).

The two scaling laws found for bending and pruning are similar to the general reconfiguration scalings observed in a wide variety of systems (de Langre *et al.* 2012). From a biological point of view, the fact that pruning leads to a stronger drag reduction than

bending can be seen as a balance to the cost of pruning, since parts of the plant are lost in the flow-induced pruning process.

3.2.3 Reconfiguration through bending and pruning

We want now to analyze the reconfiguration of a cone under flow in the general case of finite critical strain. For that purpose, we turn now to the second representation of reconfiguration introduced in Chapter 2, that of the gain in acceptable Cauchy number before base breakage, C_Y^{last}. As it was observed in the previous Chapter, we can only get a lower bound of C_Y^{last} in the pruning limit. This lower bound is due to the role of the truncation s_0; see the discussion in Appendix B.3.2. We consider therefore for each set of parameters (ε_c, β) the minimum Cauchy number at which base breakage occurs for all values of the truncation. Conversely, in the bending limit the initial truncation s_0 does not affect the reconfiguration process, thereby allowing us to compute the exact value of C_Y^{last}.

The evolution of the maximum sustainable Cauchy number C_Y^{last} as a function of the critical strain ε_c is shown in Figure 3.6, for two values of the slenderness exponent. When the slenderness β is lower than 1 (Figure 3.6a), there is no pruning, only bending can be observed. The curve corresponds therefore to the exact value of C_Y^{last}. As expected from the physical meaning of the critical strain ε_c, at low values of this parameter there is almost no reconfiguration, and the maximum sustainable Cauchy number is approximatively constant, equal to 1. The value $C_Y^{\text{last}} = 1$ is reached in the limit of ε_c equal to 0, as in Figure 2.8. As the critical strain increases, C_Y^{last} starts increasing significantly; the gain due to bending is clearly visible.

When the geometrical condition for pruning is satisfied (Figure 3.6b), the change of reconfiguration strategy is clearly visible in terms of gain in acceptable fluid velocity. In the pruning regime – when ε_c is lower than the limit value $\varepsilon_c^{\text{prun}}$, shown in dashed line – C_Y^{last} is almost constant, whereas it increases significantly with ε_c in the bending regime. However, we must emphasize that the left part of the curve (for $\varepsilon_c < \varepsilon_c^{\text{prun}}$) corresponds to the lower bound of the maximum sustainable Cauchy number before base breakage; the right part of the curve corresponds to the exact value of C_Y^{last}. One can observe that the maximum sustainable Cauchy number is almost independent of the critical strain in the pruning limit. Indeed, when the deformations are negligible, reconfiguration by pruning is not affected by the strain at breakage, but only by the geometry through β, as shown in Chapter 2. It is remarkable though that this property holds in the entire pruning region, and as long as ε_c is lower than the limit value $\varepsilon_c^{\text{prun}}$, pruning dominates the reconfiguration strategy. The limit value of C_Y^{last} when $\varepsilon_c \to 0$ corresponds in fact to that of the pruning limit shown in Figure 2.8.

At high values of the critical strain ε_c, the bending asymptotic regime is reached before base breakage. The scaling of the maximum sustainable Cauchy number C_Y^{last} can then be extracted from the analysis made in the previous Section for the bending asymptotic regime, leading to

$$C_Y^{\text{last}} \propto \varepsilon_c^2, \tag{3.13}$$

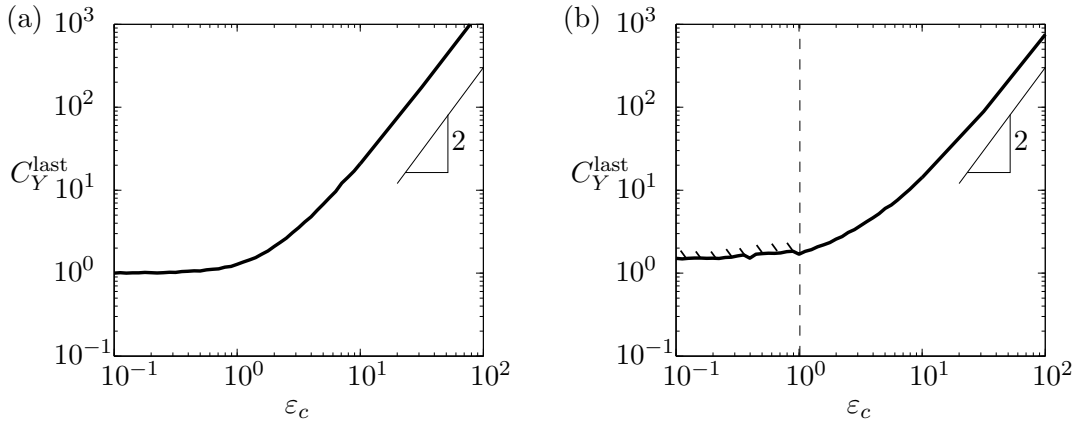

Figure 3.6: Evolution of the maximum sustainable Cauchy number C_Y^{last} as a function of the critical strain ε_c: (a) for $\beta = 0.5$, (b) for $\beta = 1.5$. The dashed line in (b) represents the limit value $\varepsilon_c^{\text{prun}}$ after which there is no pruning. Note that for $\varepsilon_c < \varepsilon_c^{\text{prun}}$ the curve is the lower bound of C_Y^{last}.

which is observed for high ε_c values (see details in Appendix C.1). Note that this behavior is independent of the slenderness β, as expected from the previous arguments concerning the asymptotic regimes. The gain in maximum acceptable Cauchy number therefore increases significantly with the critical strain.

From the evolution of the gain in maximum acceptable Cauchy number C_Y^{last}, we can therefore identify three types of behavior, that are summarized in Figure 3.7. The first one corresponds to the absence of reconfiguration (zone I). When the pruning conditions are not satisfied and the critical strain is low, neither pruning nor bending occur. The structure breaks at its base for an approximatively constant Cauchy number, $C_Y^{\text{last}} \approx 1$. The second behavior is that of pruning (zone II) when the slenderness exponent β is greater than 1 and the critical strain ε_c lower than the limit value for pruning $\varepsilon_c^{\text{prun}}$. In that case, pruning dominates the reconfiguration strategy, and the maximum sustainable Cauchy number is bounded by a lower value which is almost independent of the critical strain ε_c, $C_Y^{\text{last}} \approx C_Y^{\text{last}}(\beta)$. Finally, bending reconfiguration is observed as the critical strain gets larger than 1 (zone III). Only bending is observed, and the effect of the slenderness exponent β on the reconfiguration process vanishes. The maximum sustainable Cauchy number is then only a function of the critical strain, $C_Y^{\text{last}} \approx C_Y^{\text{last}}(\varepsilon_c)$. The exact evolution of the maximum sustainable Cauchy number as a function of the two cone parameters is shown in Appendix C.2.

The slender cone model provides therefore a general description of the reconfiguration under flow due to flow-induced pruning and elastic deformation of the structure. Figure 3.7 summarizes the different strategies, depending on the cone parameters. The different reconfiguration processes described here can be extrapolated to a large variety of systems, and each reconfiguration strategy has been linked to the mechanical and geometrical

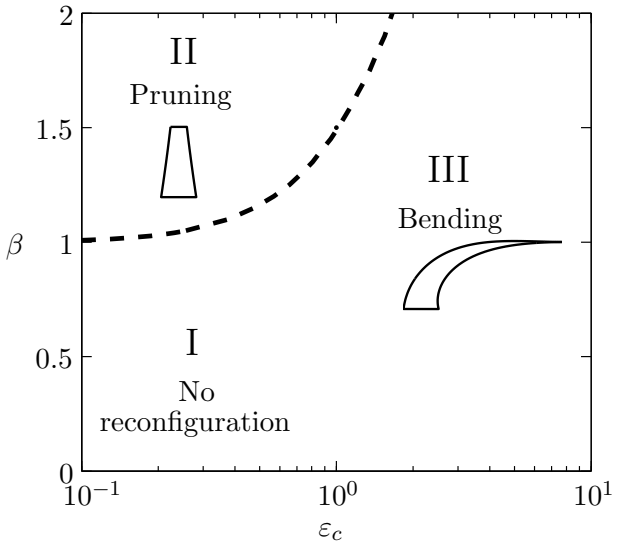

Figure 3.7: Reconfiguration strategy sketched as a function of the two parameters describing the material behavior and the geometry, ε_c and β. The dashed line represents the threshold value $\varepsilon_c^{\text{prun}}(\beta)$ after which only bending occurs.

properties of the body. However, the cone model cannot take into account more complex effects as branching or branch orientation, that are observed in tree-like structures. Moreover, this model suggests that the structure can undergo either pruning or bending, but not both. In the next Section, we turn to more elaborate models in order to determine the validity and range of application of these results.

3.3 Generalization to tree-like geometries

In this Section, we will take into account more elaborate geometrical features observed in plants. Similarly to the cone model analysis, we keep the representation simple and as general as possible. The first geometrical change that will be investigated is branching in tree-like structures, and the second will be the orientation of the branches in a plant.

3.3.1 Branching effect

Beam model for branching effect

The cone model was introduced in Section 2.4 by arguing that the essential parameter for flow-induced pruning is the slenderness exponent β. By doing so, the role of the second key parameter defining an ideal sympodial tree – parameter λ, Equation (2.3) – was not considered. This parameter characterizes branching, through the diameter evolution at a branching point. A simple way for taking branching into account is therefore to keep the parameter λ in the continuous model of a tree.

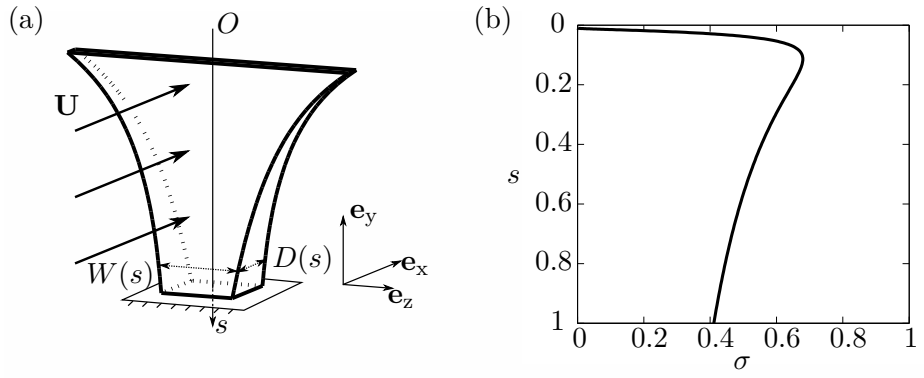

Figure 3.8: Slender beam model: (a) geometry and parametrization; (b) flow-induced stress profile for $\beta > 1$, with Leonardo's rule $\alpha = -\beta$.

In fact, considering branching for the continuous model consists in changing the dimension on which the fluid load is applied, by multiplying the force on a branch by the number of branches at the same level. This leads to modifying the cone model by adding a second dimension transverse to the flow. Hence, the resulting geometry is a slender beam with rectangular cross-section, and the transverse dimension (width noted W, see Figure 3.8a), corresponds to the local diameter multiplied by the number of branches at that height. The width reads then

$$W(s) = D_0 s^\alpha, \quad \alpha = \beta \left(1 + 2\frac{\ln p}{\ln \lambda}\right), \tag{3.14}$$

where p is the number of branches emerging from one branch at a branching point. The details showing the equivalence between the ideal sympodial tree model and this beam model are provided in Appendix A.3. As it was mentioned in Section 2.3, p is typically equal to $1/\lambda$, in order to verify Leonardo's rule. For the beam model this property yields

$$\alpha = -\beta. \tag{3.15}$$

The slender beam geometry was first introduced by McMahon (1975) as a tree model in order to analyze the gravity effect. More recently, Eloy (2011) considered this beam model to characterize the wind-induced loads and to model the size effect on the possibility of breakage under flow, showing good agreement with more elaborate models in computing the flow-induced loads.

The mechanical computation is identical to that of the cone, except for the fluid load which is now proportional to the width W instead of the diameter D in Equation (3.2). This modification leads to an obvious singularity of this model, since the parameter α is typically negative, thereby inducing a diverging fluid force at the top of the cone. This raises the question of the reference length scale chosen for the non-dimensionalization in Section 3.1.2; in that case the truncation s_0 might play a significant role in scaling

the loads and thereby the reconfiguration process. In fact, the Cauchy number and the normalized critical strain have to be rescaled by the truncation so that the value 1 has the same meaning as introduced in Section 3.1.2. However, since we are interested here in considering qualitatively the effect of adding branching to the slender cone model, the consequences of this new scaling on the equations are purposely not discussed here, but are thoroughly detailed in Appendix B.3.1.

Consequences on reconfiguration

As expected from the finite ideal tree of Section 2.3.2, the necessary condition for flow-induced pruning to occur, $\beta > 1$, still holds for the slender beam model, as shown in Figure 3.8b. This can be easily pointed out by running an analysis similar to that of the cone model in Section 2.4, see Appendix B.2.2. Therefore, one expects a very similar reconfiguration of this geometry under flow for different values of the critical strain ε_c. The corresponding reconfiguration curves are shown in Figure 3.9 in the regimes of pruning only (a), bending and pruning (b) and bending only (c).

We recover with this model the different patterns identified previously for the cone model, showing almost no effect of branching on the reconfiguration process. The high ε_c limit shows a power law dependency of the reconfiguration number identical to that found for the cone, which validates the idea that in the highly reconfigured state the tapering effect on the wind-induced loads is lost.

The curves shown in Figure 3.9b present situations where both bending and pruning are observed, and both mechanisms lead to significant drag reduction. This was not the case for the slender cone model where the drag reduction through bending was quite small (see Figure 3.4b). Indeed, a consequence of branching is that the loads are important all along the structure, as the width increases towards the top of the beam. Therefore, when reconfiguring through bending, a significant reduction of the flow-induced loads is observed before pruning starts. Moreover, this occurs in a significant range of ε_c values.

This result provides an interesting insight into the combination of bending and pruning. In this case, bending acts as a transition from no reconfiguration to pruning when the Cauchy number increases. Whereas bending is reversible on the short term and has a low biological cost, the resulting drag reduction might be insufficient to overcome excessive fluid-loading. The second mechanism, involving breakage, can then occur, resulting in a stronger drag reduction, but with a higher biological cost and only reversible in the long term.

By considering the effect of branching on the reconfiguration under flow, we showed that both bending and pruning reconfiguration can be observed in a tree-like structure. In addition to the pruning and bending regimes that were pointed out using the cone model, we were able to identify cases where the two mechanisms occur successively: first bending and then pruning. As a result, the transition from pruning behavior at low critical strain to bending behavior at high ε_c is regular. As the critical strain is increased, the range of Cauchy number for reconfiguration through bending becomes larger, and that of pruning is reduced.

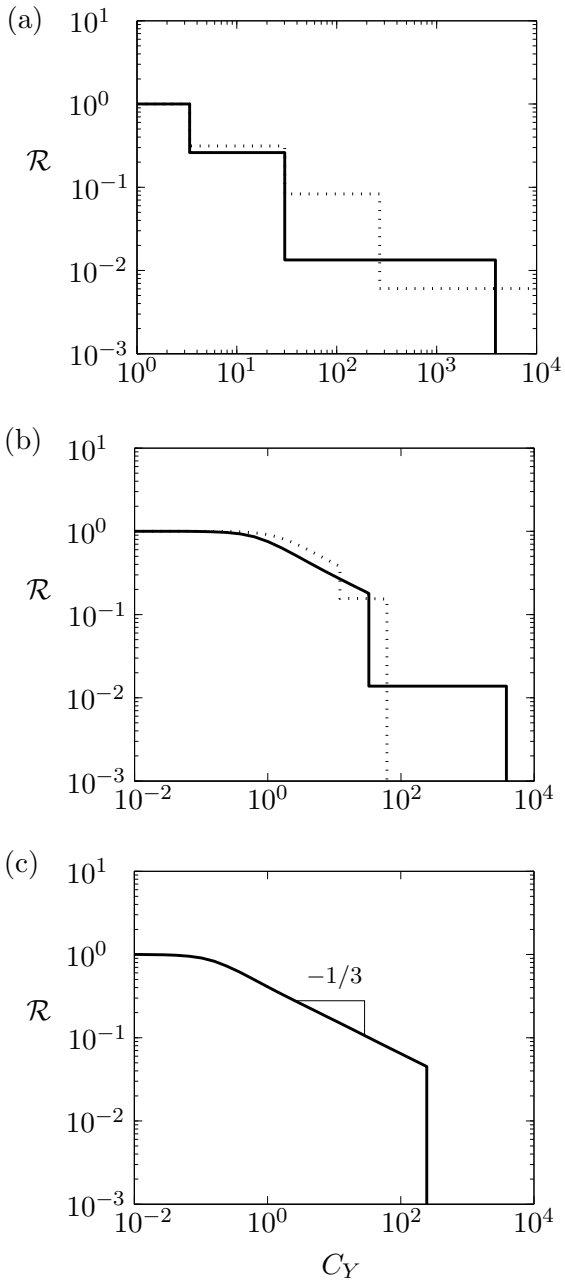

Figure 3.9: Reconfiguration curves of a slender beam satisfying Leonardo's rule ($\beta = 1.5$) in the different reconfiguration regimes: (a) flow-induced pruning ($\varepsilon_c = 0.1$), for two random values of $s_0 \ll L_0$; (b) bending and pruning, for $\varepsilon_c = 1$ ($\cdots$) and 5 (—); (c) bending only, for $\varepsilon_c = 10$.

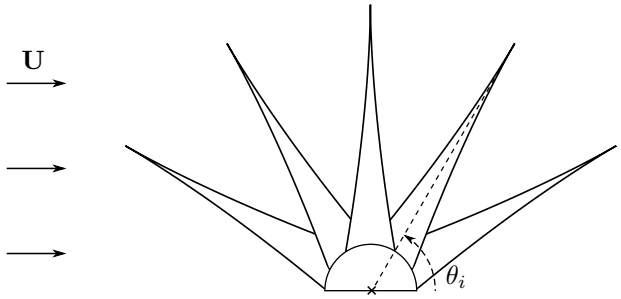

Figure 3.10: Radial bundle of cones under cross flow. Each cone is identical to that of Figure 3.1a, with a varying clamping angle at the base θ_i.

3.3.2 Angle effect

The second feature we consider is the branch orientation with respect to the flow, and more precisely the effect of combining branches of different orientations in a single structure. The simplest model to investigate this issue is a bundle of slender cones with different clamping angles, as sketched in Figure 3.10. This geometry, inspired from the poroelastic system of Gosselin & de Langre (2011), can be seen as a model for bushes or tree crowns. Moreover, by considering slender beams as introduced in the previous Section for the branching effect instead of cones, this model can represent a ramified system with different orientations. In order to look only at the angle effect we consider only slender cones as that of Figure 3.1a.

In this system, porosity effects can become significant, and the framework of a uniform cross-flow that has been used throughout this work might seem dubious. However, Gosselin & de Langre (2011) showed that when the porosity effects are non-negligible the drag is even more significantly reduced in the bending regime, from $\mathcal{R} \propto C_Y^{-1/3}$ to $\mathcal{R} \propto C_Y^{-1/2}$. We assume therefore that neglecting the porosity effects will give an overestimation of the drag and possibly of the scaling of reconfiguration in the bending regime, but will not affect the reconfiguration pattern that the structure will follow. Thus, only a two-dimensional geometry needs to be considered.

The reconfiguration curves of this radial bundle of cones are shown in Figure 3.11, for the same values of the critical strain ε_c than in Figure 3.4. Similarly to the single cone study, the different regimes (bending, pruning, or both) are observed. However, the pruning reconfiguration curve is smoothened compared to that of a single cone. In the pruning limit, all cones follow the same reconfiguration curve but for a change in Cauchy number: their reconfiguration is driven by the effective Cauchy number, namely $C_Y \sin^2\theta_i$, as the loads depend on the normal velocity $U \sin\theta_i$. Hence the different cones do not break at the same Cauchy number but at the same effective Cauchy number. This leads to a continuous reconfiguration curve even in the pruning limit. In fact, the curve in Figure 3.11a reproduces the pattern observed in Figure 2.3 for the pruning of a walnut tree, hence indicating a possible correlation between the branches' orientation and the pruning region where the bending moment is reduced as the Cauchy number increases

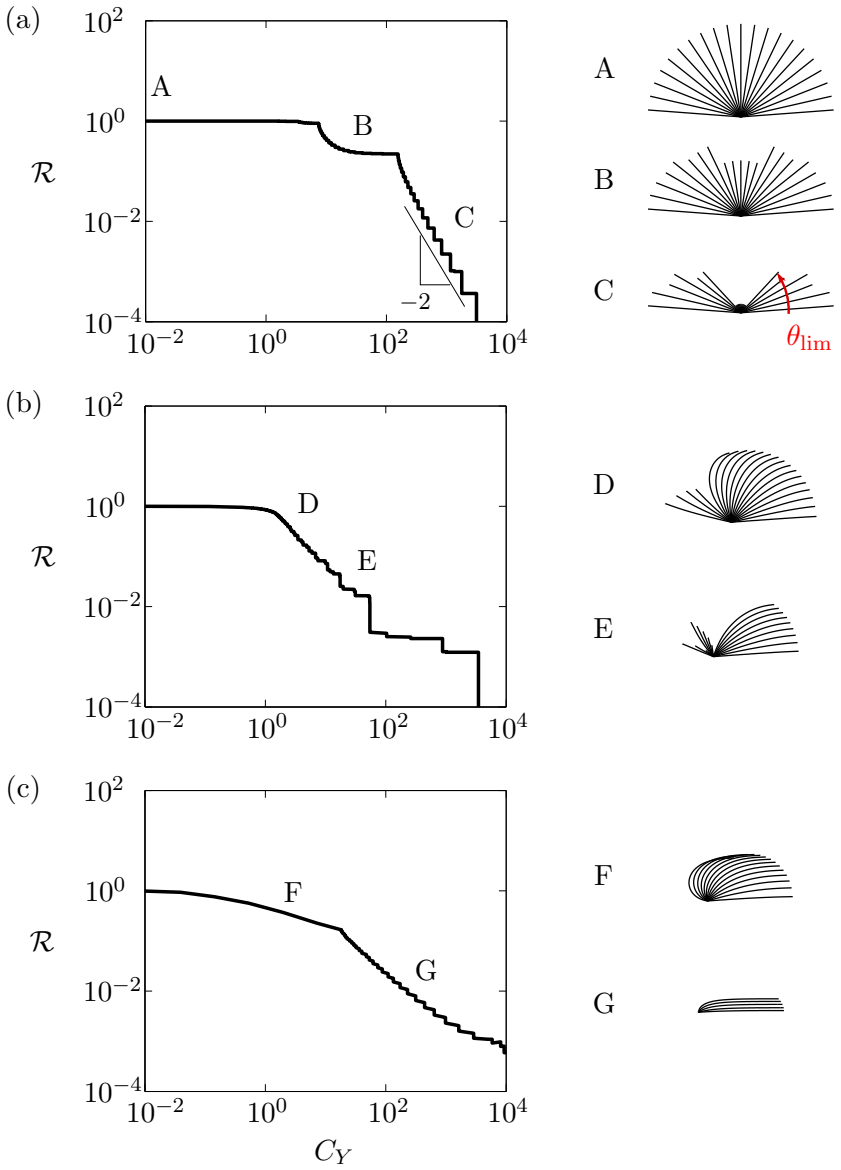

Figure 3.11: Reconfiguration curves of a radial bundle of cones under flow, and the corresponding geometries: (a) $\varepsilon_c = 0.1$, (b) $\varepsilon_c = 1$ and (c) $\varepsilon_c = 10$. The axis of the cones are sketched on the right side for different Cauchy numbers.

(region II in Figure 2.3). The corresponding geometries of the cone bundle along the reconfiguration curve show how pruning propagates upstream and downstream from the middle of the structure as the Cauchy number increases.

As the critical strain increases, the reconfiguration pattern evolves significantly, and shows non trivial behaviors. For $\varepsilon_c \sim 1$, a combination of both bending and pruning is clearly observed, as some cones (oriented upstream) undergo several breaking events while those oriented downstream only break at their base (sketches D and E). The resulting reconfiguration curve is quite complex, but a major result of these computations is the fact reconfiguration is significant over a wide range of Cauchy number. The combination of bending and pruning is even more visible at high ε_c values, for which a clear bending regime can be identified, followed by a particular regime where all cones break at their base. In that case, as opposed to the behavior observed at low ε_c, breakage propagates downstream, the first cones to be broken at their base being the upstream-facing ones.

An asymptotic regime appears at high Cauchy number when the critical strain is much lower than 1 (Figure 3.11a, sketch C). In that case, the center cones are being broken at their base, and an empty region propagates from the center of the bundle. The scaling of drag reduction in that case can be determined using the scaling found for a single cone in the pruning limit (Equation (3.10)), leading to

$$\mathcal{R} \sim C_Y^{-2}, \tag{3.16}$$

which is verified from the numerical computations at low critical strain and high Cauchy number, Figure 3.11a. The detailed derivation of this scaling law is provided in Appendix C.3. This power law leads to a remarkable result, as it implies a drag proportional to $1/U^2$, or equivalently a Vogel exponent of -4. In that particular case, the drag diminishes as the flow velocity is increased. The evolution of the drag with respect to the flow velocity is plotted in Figure 3.12, showing an original reconfiguration curve.

The study of this model geometry gives therefore interesting informations on the effect of having branches of different orientations in a tree-like structure submitted to flow. In a similar way than the effect of branching, we see that for any value of the critical strain reconfiguration occurs in a wide range of Cauchy number, leading to an important load reduction. For that geometry, the structure reconfigures first through bending, and then trough pruning as the Cauchy number increases. The range of Cauchy number for bending reconfiguration is negligible at very low critical strain, and increases with ε_c.

These models provide a better description of the coupling of bending and pruning when the critical strain is of order 1, compared to the single cone model. We see that the reconfiguration of tree-like structures will follow similar patterns for any value of the critical strain. Thus, we can assume that the study of the limit behaviors provides enough elements for characterizing the reconfiguration of any structure under flow.

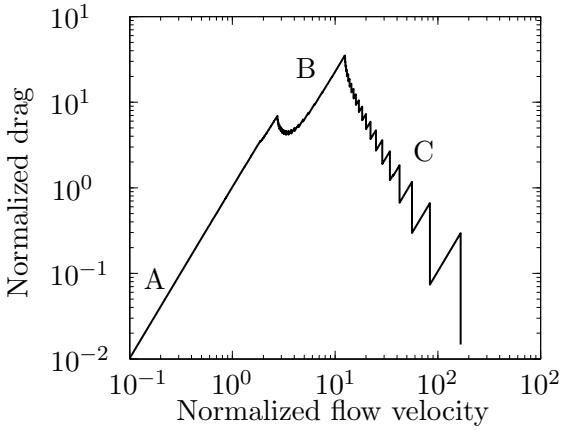

Figure 3.12: Normalized drag of a radial bundle of cones under flow, as a function of the normalized flow velocity, when the critical strain is much lower than 1. An asymptotic regime of drag diminution is clearly visible.

3.4 Discussion and conclusions

In this Chapter, we investigated the effect of combining two drag reduction strategies observed in plants, bending and pruning. Using simple models, as introduced in Chapter 2, we were able to characterize the effect of coupling deformations and breakage to reduce the flow-induced loads.

A first issue was that of the influence of bending on pruning. It was shown that the geometrical condition on the slenderness exponent β for pruning holds even when the deformations are large. However, a second necessary condition for pruning was pointed out. This conditions relies on the mechanical parameter characterizing breakage compared to deformation. This threshold value $\varepsilon_c^{\text{prun}}$ is dependent on the slenderness β, but it is of order 1. Hence pruning will generally be observed when the critical strain ε_c is lower than 1. This provides a criterion for determining which kind of reconfiguration a structure will undergo.

The slender cone model has provided insightful results on the reconfiguration process depending on the critical strain. In the limits of low and high critical strain, we showed that both bending and pruning follow an asymptotic regime. In this asymptotic regime, which is independent of the slenderness exponent β, pruning leads to a more significant drag reduction than bending. The cone model suggested that bending and pruning were not likely to be observed in the same structure. We turned therefore to more elaborate models that enabled us to take into account other geometrical parameters characterizing tree-like structures, essentially branching and branch orientation. In that case, it was shown that the different reconfiguration strategies are very similar, for any values of the critical strain. The reconfiguration of a tree-like structure under flow will follow first bending, then pruning, if the Cauchy number still increases. The range of Cauchy number over which each strategy occurs is related to the critical strain: at low critical

strain, bending effect is negligible, while pruning cannot occur at high critical strain.

Clearly, the different types of reconfiguration of tree-like structures are similar. The evolution of the reconfiguration pattern as the different parameters change is regular, and leads to equivalent consequences in terms of load reduction and gain in maximum acceptable Cauchy number. Therefore, the cone model, even if it cannot capture well the occurrence of both bending and pruning in the same structure, provides accurate predictions for estimating the reconfiguration strategy and the gain for the structure. Figure 3.7 can be considered as a universal "map" of reconfiguration; the gain in acceptable Cauchy number can be generalized to a wide variety of reconfiguration types, and the limit behaviors capture the key ingredients of reconfiguration under an external flow.

We can therefore give an overall picture of reconfiguration in plants as a function of the critical parameters β and ε_c, the first one describing the geometry of the plant, and the second describing its mechanical properties. We represent in Figure 3.13 the different evolutions of the drag with respect to the flow velocity, depending on the parameters β and ε_c. The three regions pointed out in Figure 3.7 are represented, summarizing the different drag reduction strategies and drag scaling. In the bending and pruning region, the drag follows first the bending regime and then the pruning one. The range of Cauchy number for each strategy depends on the critical strain.

When comparing with the actual values of these parameters found in plants, it can be pointed out that plants verifying $\beta < 1$ are typically one-beam plants, such as cereal crops, for which $\varepsilon_c \sim 50$ (Crook *et al.* 1994, Baker 1995). This results in a significant drag reduction by bending before breakage at the base. On the other hand, common values of ε_c in trees are found to be between 10^{-1} and 1 (Beismann *et al.* 2000, Rosner *et al.* 2007, Bjurhager *et al.* 2008, Butler *et al.* 2012), whereas leaves have ε_c values greater than 10 (Balsamo *et al.* 2003). Trees experience therefore essentially pruning, or bending and pruning, while leaves are more likely to bend under flow. Younger trees, which do not necessarily verify the geometrical condition for pruning, have much lower values of the Young Modulus (Rodriguez *et al.* 2008). This can possibly increase their strain at breakage, allowing them to reconfigure through bending. As it was already mentioned in Section 2.5, in this (ε_c, β) map stony corals are in fact in the no reconfiguration region, i.e. $\beta \leq 1$ and low critical strain ε_c (Madin 2005, Tunnicliffe 1981, Highsmith 1982). However, these particular organisms are capable of reattaching after breakage, therefore propagating through breakage. This ability to reattach can be seen as a ultimate survival strategy in a region submitted to high external fluid-loads. The results of this study are therefore consistent with the observation in nature.

The analysis of the effect of having several branches at different orientations, which is the case in most ramified plants, can provide additional informations on the morphology of plants. It was pointed out that depending on their orientation and the value of ε_c, some branches are more likely to break, protecting the rest of the plant. This gives new ideas for explaining some particular geometries as the flag trees mentioned in Chapter 1. Indeed, a possible explanation of these geometries could be that the branches growing upwind, with high ε_c while growing, would be the first to break, as shown in Figure

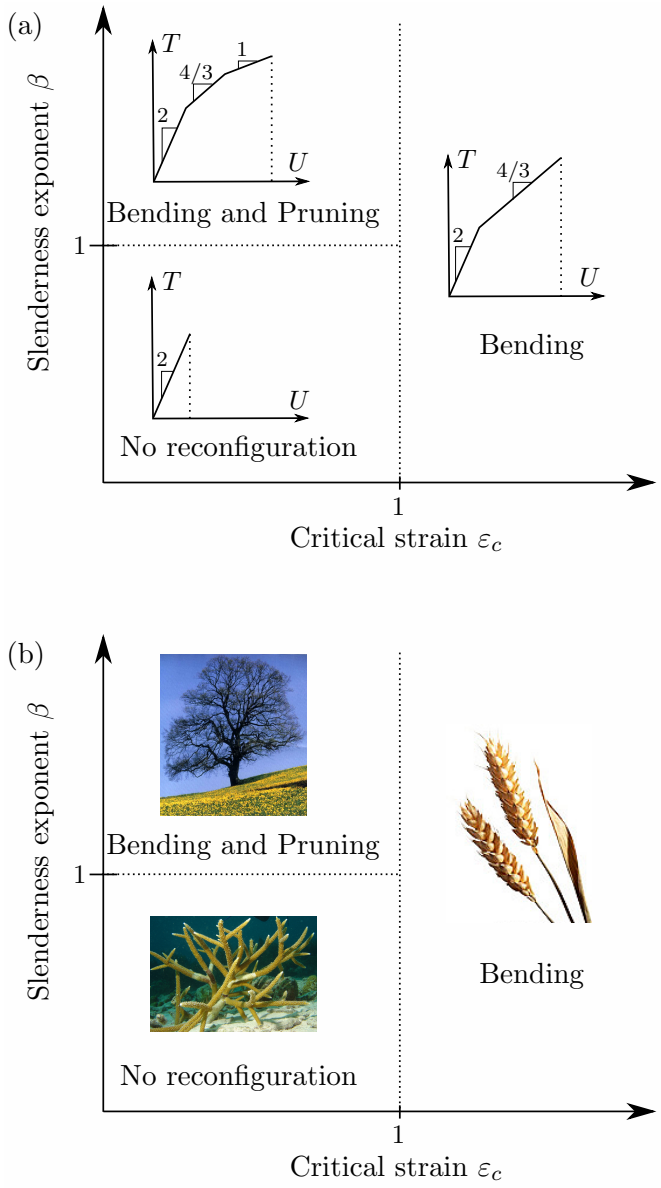

Figure 3.13: Reconfiguration under flow by bending and pruning: (a) drag evolution with respect to the flow velocity (on logarithmic scales), sketched as a function of the mechanical parameter ε_c and the slenderness exponent β; (b) pictures of plants are shown in their respective locations in this (ε_c, β) map.

3.11c, sketch G. This could result in a tree whose branches would be mainly oriented downwind. Such theory could be validated by coupling these results on breakage with a tree growth model.

From these results, one can conclude that reconfiguration, be it by pruning, bending or both, results in similar drag reduction, and leads to a significant gain in maximum sustainable fluid velocity. The combination of the two mechanisms consists in a two-step strategy. Firstly, the structure reconfigures through elastic deformation, leading to a small drag reduction, reversible in the short term. Secondly, reconfiguration occurs through breakage, more expensive and reversible only in the long term. The resulting drag reduction is then more significant, with some cases of even drag diminution with an increasing flow velocity.

Chapter 4

Application: homogenization of tree-like structures under flow

4.1 Introduction

The two previous chapters showed how plants behave under steady fluid-loading in the general case. These results were obtained considering idealized models for isolated plants, and allowed us to identify the essential parameters that drive reconfiguration. We are now interested in the application of these results in order to compute easily the effect of the flow on various types of vegetation. We want now to develop a simple continuous model capturing the basic elements of the reconfiguration of plants under flow. This model will be based on a small number of parameters, and the continuous domain corresponding to the plants will be defined directly from the parameters of the problem.

An essential result from the previous analyses is the similarity between pruning and bending as reconfiguration strategies. Indeed, both behaviors lead to a significant drag reduction and allow the plant to survive higher flow velocities. When both bending and pruning are observed, bending only delays pruning; reconfiguration at high Cauchy number is still driven by pruning. We can therefore consider that the essential features of reconfiguration of a plant are well captured by the study in the pruning limit. As a result, we will focus in this Chapter on the pruning limit, which corresponds to a low-deformation analysis. Thus, the configuration is known, and, as the mechanical problem is isostatic, the stress state is completely defined by the initial configuration.

We want to build a model that will allow us to take into account the fully coupled fluid-structure interaction problem while modeling the key elements of the geometry of plants, essentially branching and the slenderness of the branches. Since the fluid equations in a porous medium have been abundantly studied, the main objective here is to characterize the solid behavior in a continuous manner. A standard way for obtaining governing equations for the solid is to determine homogenized mechanical parameters, like elasticity coefficients, through energy balances on a representative volume (Lene 1984, Chapelle *et al.* 2010). Such homogenization techniques provide good models for composite materials and saturated porous media, allowing one to consider large defor-

mations and unsteady behaviors. However, as we place ourselves in the low-deformation case, the model does not require homogenized constitutive equations for the solid. It is thus possible to avoid the homogenization of the material coefficients in this limit.

The model developed hereafter, inspired from standard homogenization techniques, will provide a continuous volume representation of a tree-like structure submitted to an external load. The model will be developed in the next section, and in Section 4.3 a validation will be provided by considering the flow-induced pruning of the tree-like structures introduced previously. Finally in Section 4.4 we will present an application of this model where the continuous domain representing the plant is generated directly from a small number of parameters. A general discussion and conclusion about this model's scope will be given in Section 4.5.

4.2 Model construction

4.2.1 Derivation of the volume equations

Fundamental equations and definitions

The geometries of interest are typically slender and ramified structures under an external forcing (Figure 4.1a). For such geometry, the problem is isostatic, and the base equations that govern the mechanical response of the structure are the Euler-Bernoulli beam equations introduced in the previous Chapters. We consider here these equations in their general three-dimensional form

$$\frac{\mathrm{d}\mathbf{V}}{\mathrm{d}s} + \mathbf{F} = \mathbf{0}, \quad \frac{\mathrm{d}\mathbf{M}}{\mathrm{d}s} + \mathbf{t} \wedge \mathbf{V} = \mathbf{0}, \tag{4.1}$$

where $\mathbf{V}$ and $\mathbf{M}$ are the internal forces, derived along the curvilinear coordinate s, and $\mathbf{t}$ is the tangent vector (Salençon 2001). The internal force $\mathbf{V}$ is the sum of the normal and shear forces, and $\mathbf{M}$ is the total moment resulting from twisting and bending. The external forcing $\mathbf{F}$ is here the fluid force, and there is no external moment applied on the structure. For the present analysis, these equations describe completely the problem. By performing a projection on the $(\mathbf{e}_\mathrm{x}, \mathbf{e}_\mathrm{y}, \mathbf{e}_\mathrm{z})$ basis (see Figure 4.1a) all equations can be written under a general scalar form

$$\frac{\mathrm{d}Q}{\mathrm{d}s} + G = 0, \tag{4.2}$$

where Q denotes any mechanical variable defined along the beam and G a forcing term independent of Q. At a branching point, the conservation of Q reads

$$Q^- = \sum Q^+, \tag{4.3}$$

where $-$ (resp. $+$) denotes before (resp. after) branching.

In order to get volume equations for the structure behavior, we first consider a representative volume Ω (Figure 4.1b) in which there is enough solid volume fraction

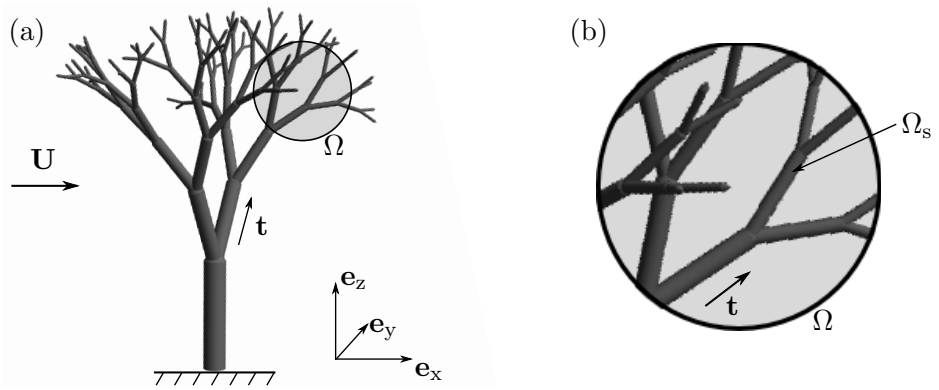

Figure 4.1: (a) Typical tree-like geometry; (b) Averaging volume and corresponding notations.

$\varphi = \Omega_s/\Omega$ for the average values to have a meaning (Whitaker 1999). Due to the high slenderness of the solid, the typical length scale of such volume Ω is at least of the order of the length of the branch segments, in order for Ω to be representative. We use a standard average operator, noted $\langle . \rangle$, which reads

$$\langle . \rangle = \frac{1}{\Omega} \int_{\Omega} . \mathrm{d}\Omega, \tag{4.4}$$

and we define the average over the solid volume, noted with the index s, which for a quantity Q defined in the solid verifies $\langle Q \rangle = \varphi \langle Q \rangle_s$. The volume average of a spatial divergence is related to spatial divergence of a volume average through

$$\langle \nabla . \mathbf{Q} \rangle = \nabla . \langle \mathbf{Q} \rangle + \frac{1}{\Omega} \int_{\mathcal{S}_i} \mathbf{Q} . \mathbf{n}_i \mathrm{d}\mathcal{S}_i, \tag{4.5}$$

where $\mathcal{S}_i$ is the solid/fluid interface inside Ω, and $\mathbf{n}_i$ denotes the normal to the interface oriented towards the solid (Whitaker 1999).

Averaging method

One main problem of the solid equations is that they are piecewise equations, with specific jumping relations at the nodes. In order to overcome this issue, we want to modify the beam description and have continuous quantities defined in the solid volume. The beam is thus considered to have a volume Ω_s which results from taking into account the branch cross-section $A(s)$ normal to the beam axis. For any quantity $Q(s)$ we define in Ω_s a continuously differentiable function $q(s, \mathbf{p})$, where $\mathbf{p}$ describes the cross-section $A(s)$; q is defined in the branches by

$$q(s, \mathbf{p}) = \frac{Q(s)}{A(s)}. \tag{4.6}$$

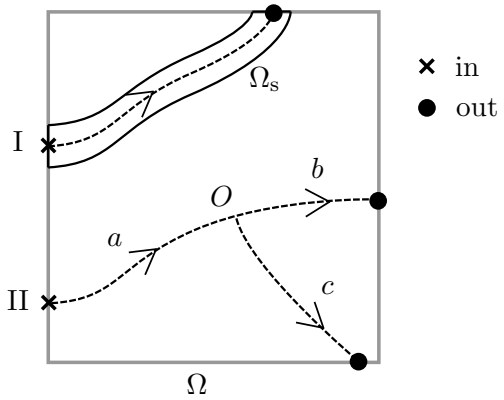

Figure 4.2: Averaging method: model geometry and corresponding notations.

This definition leads to some singularities at the branching points and at the borders of the averaging volume. Due to the high slenderness of the beams, these singularities are easily overcome without loss of generality; these technical points are discussed in Appendix D.

We consider the sketch of Figure 4.2 for obtaining volume equations. We denote Q^{in} the sum of Q where the branches go into Ω, and respectively Q^{out} where the branches go out of Ω. According to the previous notations and hypothesis, we can write for branch I in Figure 4.2

$$Q_I^{\text{out}} - Q_I^{\text{in}} = \oint_{\partial\Omega_{\text{s}}I} \frac{Q}{A}\mathbf{t}.\mathbf{n}_{\Omega_{\text{s}}}\mathrm{d}\mathcal{S} = \oint_{\partial\Omega_{\text{s}}I} q\mathbf{t}.\mathbf{n}_{\Omega_{\text{s}}}\mathrm{d}\mathcal{S} \tag{4.7}$$

Since the function q is continuously differentiable in Ω_{s}, we can apply the divergence theorem. By introducing the average operator as defined in Equation (4.4), the sum over each independent branch (here noted I and II) results in

$$Q^{\text{out}} - Q^{\text{in}} = \Omega_{\text{s}}\langle\nabla.(q\mathbf{t})\rangle_{\text{s}}. \tag{4.8}$$

Using the averaging operator property of Equation (4.5), we can re-write the previous expression

$$Q^{\text{out}} - Q^{\text{in}} = \frac{\Omega_{\text{s}}}{\varphi}\nabla.\langle q\mathbf{t}\rangle. \tag{4.9}$$

This first relation between Q_I^{in} and Q_I^{out} has to be completed using the equation for Q along the branches given in Equation (4.2). For branch I of Figure 4.2 this leads to

$$Q_I^{\text{out}} - Q_I^{\text{in}} = -\int_{\text{in}_I}^{\text{out}_I} G\mathrm{d}s = -\int_{\Omega_{\text{s}}I} g\mathrm{d}\Omega. \tag{4.10}$$

The same analysis can be done on branch II, using the relation $Q_b^O + Q_c^O - Q_a^O = 0$ at

the branching point. This leads in the general case to

$$Q^{\text{out}} - Q^{\text{in}} = -\int_{\text{in}}^{\text{out}} G\mathrm{d}s, \tag{4.11}$$

where the integration from "in" to "out" represents the summation along every oriented branch in Ω. By neglecting the effect of the branching region (see Appendix D), we can write in the general case

$$Q^{\text{out}} - Q^{\text{in}} = -\Omega_{\text{s}}\langle g\rangle_{\text{s}}. \tag{4.12}$$

By combining Equations (4.9) and (4.12), we get the volume equation on q, resulting from Equations (4.2) and (4.3) for any scalar quantity Q,

$$\nabla.\left(\varphi\langle q\mathbf{t}\rangle_{\text{s}}\right) + \varphi\langle g\rangle_{\text{s}} = 0. \tag{4.13}$$

If we consider now the general beam equations Equation (4.1), the same analysis can be done on the projection of these equations on the basis $(\mathbf{e}_{\text{x}}, \mathbf{e}_{\text{y}}, \mathbf{e}_{\text{z}})$, and the resulting average equations can be expressed as a set of vectorial equations

$$\nabla.\left(\varphi\langle \mathbf{v}\otimes\mathbf{t}\rangle_{\text{s}}\right) + \varphi\langle \mathbf{f}\rangle_{\text{s}} = \mathbf{0}, \tag{4.14}$$

$$\nabla.\left(\varphi\langle \mathbf{m}\otimes\mathbf{t}\rangle_{\text{s}}\right) + \varphi\langle \mathbf{t}\wedge\mathbf{v}\rangle_{\text{s}} = \mathbf{0}, \tag{4.15}$$

where $\otimes$ denotes the tensorial product.

The above equations were obtained using only the high slenderness property of the beams constituting the solid body. At this point, Equation (4.13) is a general form of the volume equations resulting from a one-dimensional description as that of Equation (4.2). The coupling of Equations (4.14) and (4.15) is not straightforward, since the internal force that plays as a forcing term in the moment equation is not directly correlated to the one given by the first equation. In the next Section, a closure of Equations (4.14) and (4.15) is provided.

4.2.2 Equations of the homogenized model

First order approximation

The previous equations can be decomposed using the spatial fluctuation defined as

$$Q'_{\text{s}} = Q - Q_{\text{s}}, \tag{4.16}$$

where $\langle Q\rangle_{\text{s}}$ is noted Q_{s} for commodity in the following. The resulting equations read

$$\nabla.\left(\varphi\mathbf{v}_{\text{s}}\otimes\mathbf{t}_{\text{s}}\right) + \varphi\mathbf{f}_{\text{s}} + \nabla.\left(\varphi\langle \mathbf{v}'_{\text{s}}\otimes\mathbf{t}'_{\text{s}}\rangle_{\text{s}}\right) = \mathbf{0} \tag{4.17}$$

$$\nabla.\left(\varphi\mathbf{m}_{\text{s}}\otimes\mathbf{t}_{\text{s}}\right) + \varphi\mathbf{t}_{\text{s}}\wedge\mathbf{v}_{\text{s}} + \nabla.\left(\varphi\langle \mathbf{m}'_{\text{s}}\otimes\mathbf{t}'_{\text{s}}\rangle_{\text{s}}\right) + \varphi\langle \mathbf{t}'_{\text{s}}\wedge\mathbf{v}'_{\text{s}}\rangle_{\text{s}} = \mathbf{0} \tag{4.18}$$

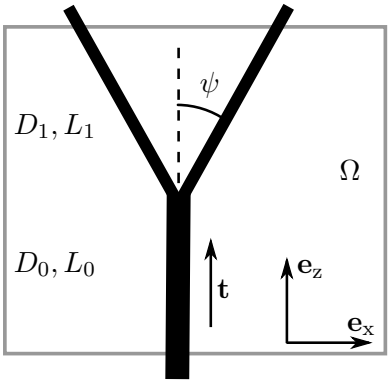

Figure 4.3: Example of averaging over a Y-shaped geometry.

The first order approximation that is done here consists in considering that the fluctuating terms are negligible compared to the corresponding mean values,

$$\|Q'_s\| \ll \|Q_s\|. \tag{4.19}$$

Equivalently, this consists in modeling the solid quantities by their average value in the solid volume,

$$Q \equiv Q_s. \tag{4.20}$$

In order to get an idea of the meaning of this hypothesis, we can consider a Y-shaped branch with an opening angle at branching ψ (see Figure 4.3). For that geometry, the solid volume average of vector field $\mathbf{t}$ reads

$$\mathbf{t}_s = \frac{D_0 L_0 + 2 D_1 L_1 \cos\psi}{D_0 L_0 + 2 D_1 L_1} \mathbf{e}_z, \tag{4.21}$$

whereas $\mathbf{t}$ is equal to $\mathbf{e}_z$ in the first level, and then $\cos\psi \mathbf{e}_z \pm \sin\psi \mathbf{e}_x$. When the angle ψ is small, this hypothesis is justified, and it is exact when $\psi = 0$. Under this assumption, a new form of the volume equations is found

$$\nabla.\,(\varphi \mathbf{v}_s \otimes \mathbf{t}_s) + \varphi \mathbf{f}_s = \mathbf{0} \tag{4.22}$$

$$\nabla.\,(\varphi \mathbf{m}_s \otimes \mathbf{t}_s) + \varphi \mathbf{t}_s \wedge \mathbf{v}_s = \mathbf{0}, \tag{4.23}$$

which is now a closed system of equations, with six unknowns in the general three-dimensional case. These field equations can be solved directly. In this case, only the average fluid force field, the solid volume fraction and the average branch direction field have to be known for solving the problem. We present hereafter a particular solution technique that simplifies the solid equations to a set of one-dimensional equations.

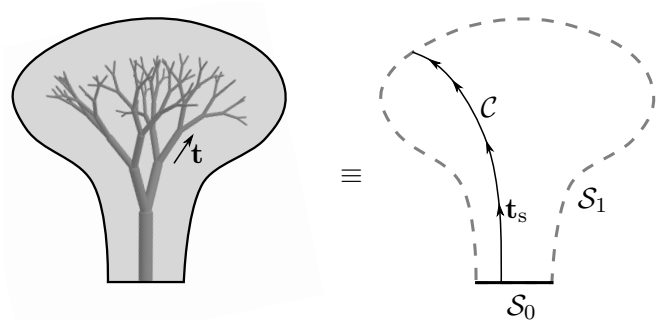

Figure 4.4: Sketch of a characteristic curve used for solving the homogenized problem.

Solution on characteristic curves

By expending the divergence of the tensorial product in Equations (4.22) and (4.23), and using the fact that $\mathbf{t}_\mathrm{s}.\nabla$ corresponds to the derivative with respect to the curvilinear coordinate x_s along the curve $\mathcal{C}$ tangential to $\mathbf{t}_\mathrm{s}$, we can write Equations (4.22) and (4.23) as one-dimensional equations along $\mathcal{C}$

$$\|\varphi\mathbf{t}_\mathrm{s}\|\frac{\mathrm{d}\mathbf{v}_\mathrm{s}}{\mathrm{d}x_\mathrm{s}} + \mathbf{v}_\mathrm{s}\nabla.\varphi\mathbf{t}_\mathrm{s} + \varphi\mathbf{f}_\mathrm{s} = \mathbf{0} \tag{4.24}$$

$$\|\varphi\mathbf{t}_\mathrm{s}\|\frac{\mathrm{d}\mathbf{m}_\mathrm{s}}{\mathrm{d}x_\mathrm{s}} + \mathbf{m}_\mathrm{s}\nabla.\varphi\mathbf{t}_\mathrm{s} + \varphi\mathbf{t}_\mathrm{s}\wedge\mathbf{v}_\mathrm{s} = \mathbf{0}. \tag{4.25}$$

The model equations can therefore be solved considering Equations (4.24) and (4.25) on characteristic curves that are streamlines of the vector field $\mathbf{t}_\mathrm{s}$, as sketched in Figure 4.4. Such curves are oriented from the ground $\mathcal{S}_0$ to the border of the domain $\mathcal{S}_1$, free of loads.

We obtain a set of one-dimensional equations, defined on characteristic curves that only depend on the average branch direction vector field $\mathbf{t}_\mathrm{s}$. The resulting continuous volume equations are one-dimensional, as the Euler-Bernoulli equations (4.1), but with the advantage that they are defined everywhere continuously. The branching and geometric effects are held in the $\nabla.\varphi\mathbf{t}_\mathrm{s}$ term, which is zero for cylindrical beams but non-zero when branching or tapering occurs, for instance.

The equivalent continuous medium for a tree-like structure is thus a bundle of fibers, on which the mechanical computation can be solved from Equations (4.24) and (4.25). One needs only the fiber shape through the vector field $\mathbf{t}_\mathrm{s}$ and the solid volume fraction φ. In order to compute the actual internal forces in the structure we need also an information on the cross-sectional area, which is taken here to be the field $\mathcal{A}_\mathrm{s}$ defined by

$$\mathcal{A}_\mathrm{s} = \langle\frac{1}{A}\rangle_\mathrm{s}. \tag{4.26}$$

The actual internal forces resulting from the fluid load can be then derived through $Q \equiv q_\mathrm{s}/\mathcal{A}_\mathrm{s}$.

4.3 Model validation on flow-induced pruning

4.3.1 Mechanical analysis

In order to validate the homogenized model, we consider now the brittle scenario defined in Chapter 2, in the two-dimensional case. The brittle structure is held by a perfect clamping at the base, and the flow-induced stress state is computed on the initial configuration. Similarly to the previous Chapters, the breakage criterion relies on the bending stress, which is related to the bending moment M through $\Sigma = 32M/\pi D^3$.

The present model is compared to finite element computations on exact geometries. In that case, the breaking events are treated as in Chapter 2. For the homogenized model, the same procedure is applied on the equivalent fibers, and breakage occurs on the local fiber on which the breakage criterion is reached. The fluid velocity is further increased until a new breaking event occurs. In the present model, base breakage is characterized by considering the fraction of fibers broken at their base; when this fraction reaches a limit fraction, here 10%, the structure is considered to be broken at its base. This analysis is carried out in the two-dimensional case, therefore Equation (4.25) is a scalar equation, and the cross section A is equal to the diameter D. The bending stress is then modeled by

$$\Sigma \equiv \frac{32}{\pi} {\mathcal{A}_{\mathrm{s}}}^2 m_{\mathrm{s}}. \tag{4.27}$$

Similarly to the previous analysis, the structure is submitted to a uniform flow $\mathbf{U} = U\mathbf{e}_{\mathrm{x}}$. The local fluid force results from the normal pressure drag oriented along the normal to the branch axis,

$$\mathbf{F} = \frac{1}{2}\rho C_D D|\mathbf{U}.\mathbf{n}|(\mathbf{U}.\mathbf{n})\mathbf{n}, \tag{4.28}$$

where ρ is the fluid density, $\mathbf{U}$ the fluid velocity and C_D the drag coefficient. Using the assumption of Equation (4.20), the volume forcing can be modeled by

$$\mathbf{f}_{\mathrm{s}} \equiv \frac{1}{2}\rho C_D U^2 |\mathbf{e}_{\mathrm{x}}.\mathbf{n}_{\mathrm{s}}|(\mathbf{e}_{\mathrm{x}}.\mathbf{n}_{\mathrm{s}})\mathbf{n}_{\mathrm{s}}, \tag{4.29}$$

where $\mathbf{n}_{\mathrm{s}} = \mathbf{e}_{\mathrm{z}} \wedge \mathbf{t}_{\mathrm{s}}$ in 2D. Finally, we consider the same definition for the non-dimensional fluid-loading, i.e. the Cauchy number,

$$C_Y = \frac{\rho C_D U^2}{\Sigma_c} G, \tag{4.30}$$

where G is a geometric factor introduced as in Chapter 2 for comparison purpose between the different computations. As base breakage is defined differently for the homogenized model, the scaling of G that was used in Chapter 2 cannot be applied to these computations. Hereafter, the scaling of G is such that the first breaking event occurs at $C_Y = 1$. Similarly to the flow-induced pruning analysis of Chapter 2, we consider here the base bending moment as a relevant flow-induced load for studying the reconfiguration. How-

ever, for a better visualization of the results, we will consider here reconfiguration curves, where the reconfiguration number $\mathcal{R}$ is defined as the bending moment at the base normalized by its value without reconfiguration. In the case of the homogenized model, the base bending moment will be taken to be the mean value at the base.

4.3.2 Comparison with direct computations on idealized trees

Parameters and average fields

The first geometry used for validation is the ideal tree model introduced in Section 2.3. For the present study, we consider, in addition to the two parameters λ and β, the branching angle ψ as defined in Figure 4.3. Reconfiguration by pruning is first computed using a standard finite element software (CASTEM v.3M); this computation will be referred to as FEM in the following. The fields $\{\mathbf{t}_\mathrm{s}, \varphi, \mathcal{A}_\mathrm{s}\}$ that are needed for the homogenized model (HM) computation are obtained numerically by averaging over the tree. The representative averaging surface (in two dimensions) has a typical dimension of the order of the length of the first branches after the trunk. Of course, applying the averaging method along the trunk can be dubious, but, in order to keep the model free of a matching condition between the trunk and the tree crown, the same model is used throughout the entire structure. The model equations (4.24) and (4.25) are then solved using a standard explicit algorithm on characteristic curves $\mathcal{C}$ computed as streamlines of the vector field $\mathbf{t}_\mathrm{s}$.

Flow-induced pruning curves

The reconfiguration curves obtained by FEM and HM computations are shown in Figure 4.5a. The general behavior is recovered, and the two curves follow the same pattern: (i) an important diminution of the reconfiguration number once pruning starts at $C_Y = 1$, (ii) a plateau where small base moment reductions occur, (iii) base breakage at the maximum sustainable Cauchy number C_Y^{last}. These regimes were already observed for the walnut tree in Section 2.2. The first reduction of $\mathcal{R}$ is quite accurately predicted by the HM computations, giving a good estimation of the fluid load reduction by pruning. The Cauchy number at which base breakage occurs C_Y^{last} is slightly overestimated. This will be discussed further, as the branching angle and the tree symmetry seem to play an important role in this value. The HM curve exhibits a smoothened behavior compared to that resulting from the FEM, which shows sudden drops in base moment as branches are broken. Indeed the homogeneous description provides a continuous reconfiguration process.

The ideal tree model being a particular case with important symmetries, the same comparison is held on a tree with random variations of its parameters (λ, β, ψ) of 10% (Figure 4.5b). Such random variations can represent more realistic geometries, as actual trees do not have a single value of its allometric parameters. In that case the smooth curve given by the HM computation reproduces well the behavior of a realistic tree, and the overestimation of C_Y^{last} is reduced. Indeed, the geometrical variability leads to a

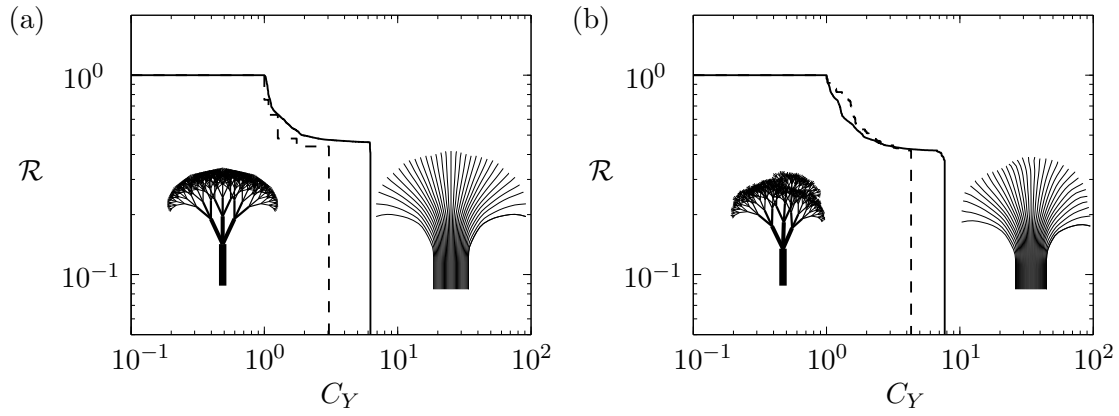

Figure 4.5: Reconfiguration curves of a tree ($\lambda = 0.3, \beta = 1.5, \psi = 25°$) under uniform cross-flow: (a) comparison between finite element method (- - -) and homogenized model (—) for the ideal tree; (b) same comparison for a tree with random variation of its parameters.

smoother curve, as that of the walnut tree in Section 2.2. Not all symmetric branches will break at the same Cauchy number, therefore the variability can help increasing the maximum sustainable Cauchy number C_Y^{last}. Furthermore, the homogeneous description provides very similar curves for the ideal and random trees, whereas the FEM shows significant differences between the two reconfiguration curves. This is shown in Figure 4.6, where the reconfiguration curves of eight random trees – with the same reference parameters – are superimposed with the reference tree curve. We can observe that all curves follow almost a single curve. The homogenization is naturally expected to reduce the effect of variability within the structure, it is therefore consistent to see similar curves for the ideal tree and the same tree with random variations.

Despite some errors – mainly on the maximum sustainable Cauchy number – the homogenized model provides accurate predictions of the reconfiguration. Moreover, the errors made in the HM computations are reduced in the case of realistic geometries. The homogenized model provides therefore a good estimation of the flow-induced pruning of realistic trees.

Parameter dependency

In order to provide a general validation of the homogenized model for various geometries, we can look at the effect of varying the parameters (λ, β, ψ) for the tree studied above. We consider the maximum Cauchy number C_Y^{last} that the structure can sustain before base breakage for validating the present model. The evolution of C_Y^{last} as a function of the different parameters is shown in Figure 4.7. The general influence of each parameter is recovered, with some slight differences.

The effect of λ is consistent with the size of broken branches presented in Section 2.3.2, since for these computations, due to numerical limitations, the trees are limited

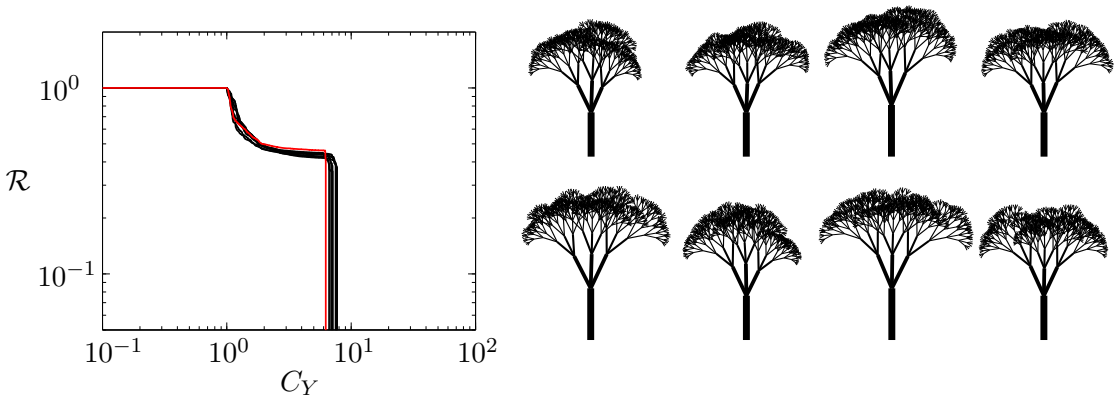

Figure 4.6: Reconfiguration curves of 8 random trees obtained by the homogenized model. The reconfiguration curve of the reference tree is shown in red ($\lambda = 0.3, \beta = 1.5, \psi = 25°$).

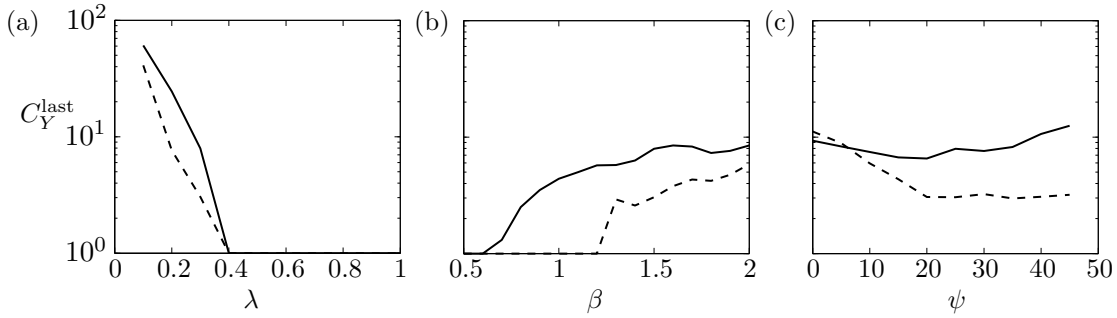

Figure 4.7: Maximum sustainable Cauchy number before base breakage as a function of the tree parameters: (a) diameter reduction at branching λ, (b) slenderness exponent β, and (c) angle at branching ψ, using FEM (- - -) and HM (—).

to 7 orders of branches. Therefore, once λ is larger than ~ 0.4 there is no flow-induced pruning of the structure. Before this threshold the HM computations show very good results. The role of β, which has to be larger than 1 for pruning to occur in the ideal tree is not exactly recovered, due to the fact that the model relies on internal forces divided by the cross-sectional area. Therefore the role played by β is clearly modified, as it can be seen in Equation (4.29) where the fluid force does not depend on the average diameter. The field chosen for the cross-sectional dimension $\mathcal{A}_s$ plays also a role, as the bending stress is dependent on this choice. However, the general evolution of C_Y^{last} is consistent with the previous results and the FEM, and its augmentation for higher β values is recovered.

The effect of the branch angle ψ is consistent with the hypothesis made for this model in the previous section. For small values of ψ the HM computation matches very well with the FEM computations, whereas a difference appears at higher ψ values.

The neglected terms in the model can become important for high ψ; thus, the present model underestimates the flow-induced loads, and the Cauchy number at which base breakage will occur is overestimated. Nonetheless, this shows very good agreement with the FEM computations, and at first order the model developed here provides a good estimation of the flow effect on the structure and the resulting reconfiguration curve.

Fields reactualization

As the structure can break under flow, there is an issue about the average quantities initially defined. The previous results were obtained without taking into account any modification of the initial fields $\{\mathbf{t}_\mathrm{s}, \varphi, \mathcal{A}_\mathrm{s}\}$, therefore computing the reconfiguration curve of each equivalent fiber independently. We present hereafter a possible way for considering a modification of the solid volume fraction φ. Since the discretization in characteristic curves (or equivalent fibers) is only a mean to solve the equations, there is no direct link between one fiber and the volume it represents. A way of modeling the solid volume change when breakage occurs is to consider, in a volume equal to the averaging volume, the ratio between the length of broken fiber and the total length of fibers in that volume. This ratio r characterizes the broken fiber volume fraction, which is then taken into account for reducing the solid volume fraction through

$$\varphi \to \varphi(1 - r). \tag{4.31}$$

The result of that modification is shown in Figure 4.8. In this computation, the solid volume fraction was modified after each breaking event in the region affected by this event. A first observation is that this modification has little effect on the general trend of the reconfiguration curve. A major difference is the occurrence of a vertical drop of $\mathcal{R}$, similar to that observed in the FEM curves. This is in fact due to an unstable situation after a breaking event, in the sense that the fibers neighboring the broken one experience a higher stress level after the breaking event. This results in a propagation of fracture within a certain area in the continuous domain, at the same Cauchy number. This behavior can be interpreted as the equivalent breakage of an entire branch. However, apart from this effect, the general pattern is the same, as well as the maximum Cauchy number C_Y^{last}.

Taking into account modifications in the average fields after breakage is delicate, since the actual geometry is purposely lost in the homogeneous description, thereby making it difficult to recompute the fields afterwards. The computation presented above when modifying the solid volume fraction after breakage showed no major modifications in the reconfiguration by pruning, therefore suggesting that this would have a second order effect on the structure response under flow.

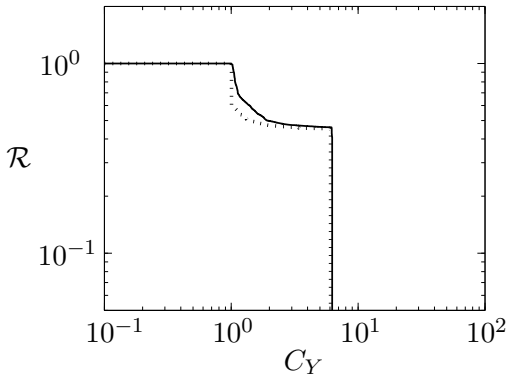

Figure 4.8: Effect of a modification of the solid volume fraction after a breaking event in the homogenized model: no modification (—), with modification ($\cdots$).

4.4 Direct construction of the equivalent homogeneous domain

In the analysis of the previous section, the average fields $\{\mathbf{t}_\mathrm{s}, \varphi, \mathcal{A}_\mathrm{s}\}$ were obtained by numerically averaging over a given structure. Such procedure can be possible for the study of a single plant. However, in order to model a forest, generating a large number of random trees and then proceeding to an averaging process over the forest would be quite long. Moreover, once the exact geometry is generated, the direct computation on the structure might be faster than using the present homogenized model, and lead to more accurate results. An interesting application of this model would be therefore to avoid the averaging process and model directly the structure by fields defined analytically. Modeling directly the equivalent homogeneous domain would allow much faster computations that could be coupled with existing models for the flow.

The present model consists in solving one-dimensional equations on particular fibers describing the structure. On the other hand, the cone and beam models of the previous Chapters – which are one-dimensional models – provide consistent results for modeling reconfiguration by pruning. It seems therefore that there is a link between these two descriptions. Coupling these different model should enable us to get analytical expressions for the average fields $\{\mathbf{t}_\mathrm{s}, \varphi, \mathcal{A}_\mathrm{s}\}$ and avoid the averaging process. By doing so, one could model a part of a plant – or an individual plant – by a cone, and combine it with the present homogenized model in order to represent a single plant or a group of plants, depending on the scale of interest.

As the fields will be determined analytically in that case, one has to be careful that they actually model a plant. The vector field $\mathbf{t}_\mathrm{s}$ that describes the direction of the branches must be such that every region in the domain is reached by a streamline going from the ground $\mathcal{S}_0$ to the free border of the domain $\mathcal{S}_1$ as defined in Figure 4.4. The corresponding characteristic curves are therefore similar to that shown in Figure 4.4. These conditions on $\mathbf{t}_\mathrm{s}$ correspond to the fact that the equivalent homogeneous domain

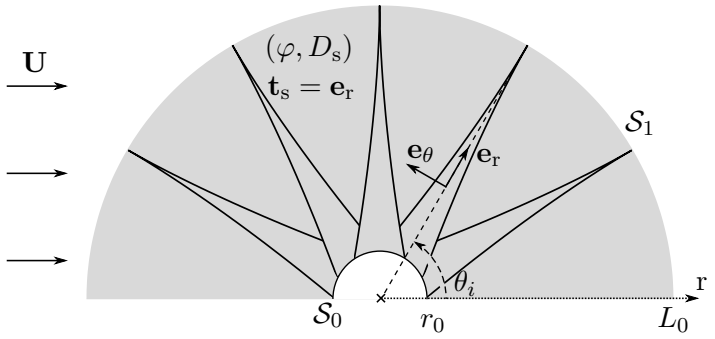

Figure 4.9: Continuous geometry (radial bundle of cones) where the average fields are defined analytically, and corresponding notations.

is a bundle of fibers, held by a perfect clamping on $\mathcal{S}_0$ and with their free end on $\mathcal{S}_1$.

In order to validate the combination of the slender cone model and the present homogenized model, we consider hereafter the radial bundle of cones introduced in Section 3.3.2; the diameter of each cone reads

$$D(r, \theta_i) = D_0 \left(\frac{L_0 - r}{L_0 - r_0} \right)^\beta, \tag{4.32}$$

with a discrete radial distribution θ_i, Figure 4.9. The corresponding continuous medium is a radial two-dimensional geometry with standard cylindrical coordinates (r, θ), where the average fields read

$$\mathbf{t}_\mathrm{s}(r, \theta) = \mathbf{e}_\mathrm{r}, \tag{4.33}$$

$$\mathcal{A}_\mathrm{s}(r, \theta) = \frac{1}{D_0} \left(\frac{L_0 - r_0}{L_0 - r} \right)^{\beta+1}, \tag{4.34}$$

$$\varphi(r, \theta) = \varphi_0 \frac{r_0}{r} \frac{1}{D_0 \mathcal{A}_\mathrm{s}}, \tag{4.35}$$

where $\mathcal{S}_0$ is defined by $r = r_0$, D_0 a reference diameter and φ_0 the solid volume fraction on $\mathcal{S}_0$, and L_0 the length of the equivalent fibers.

The reconfiguration of this model geometry is shown in Figure 4.10, compared to the computation on the radial bundle of cones. The HM computation shows a very good agreement with the direct computation. The different reconfiguration number drops as well as the range of Cauchy number over which pruning occurs are well recovered. The comparison of the two geometries at different Cauchy numbers show similar patterns, with the same broken region that propagates downstream and upstream when increasing the flow velocity. On this simple example, the continuous domain is built analytically from the different models, and the computation using the homogenized equations on the radial characteristic curves models accurately the reconfiguration by pruning of the radial bundle of cones.

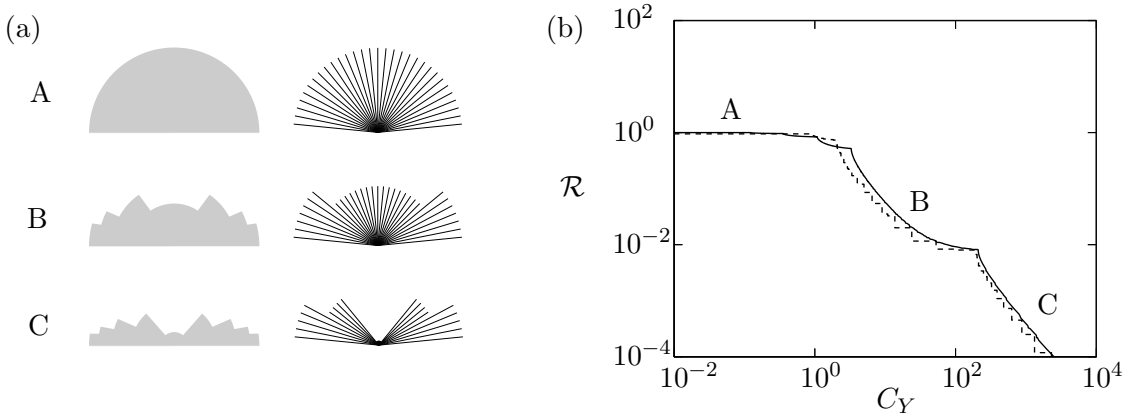

Figure 4.10: Flow-induced pruning of the continuous radial geometry and the corresponding cone bundle: (a) Geometries at three different stages of reconfiguration, homogeneous geometry (gray area) and cone bundle (cones axes in solid lines); (b) reconfiguration curves of the continuous radial geometry (—) and the cone bundle (- - -).

This second analysis provides another validation of the homogenized model, and shows a major application of this description combined with the beam model. In that case, the fields $\{\mathbf{t}_s, \varphi, \mathcal{A}_s\}$ do not result from an averaging process: the continuous domain is given directly. This suggests that a proper use of these models can be an accurate way for modeling complex ramified structures in a continuous manner. Since there is no averaging process, the computations are light and can be easily used for large domains.

4.5 Discussion and conclusions

It was established in Chapters 2 and 3 that reconfiguration by pruning is equivalent to any type of reconfiguration. From that result, the continuous model was developed in the pruning limit for the study of the static response of a brittle structure to an external fluid forcing. By considering the linear beam equations for slender branched structures, we derived a new formulation of the conservation laws in a ramified system. At that point, this model could be in fact applied to a wide variety of problems, like internal flows in a pipe network, or in fact the transport of any quantity through a branched network. The only characteristic needed on the network is that the initial problem is isostatic and has a one-dimensional description along the branches of the system.

In a first order approximation, it was considered that the quantities defined in the solid are equivalent to their average values in the solid volume. From this assumption, the model equations were reduced to a set of one-dimensional equations along characteristic curves $\mathcal{C}$, defined as streamlines of the average branch direction vector field $\mathbf{t}_s$. The equivalent medium is a bundle of fibers which satisfy mechanical equations similar to Euler-Bernoulli beam equations, with an additional term representing branching and tapering effects. The fields that are therefore needed to compute the mechanical loads

in the homogeneous medium are only the average branch direction $\mathbf{t}_s$, the solid volume fraction φ and a cross-sectional dimension $\mathcal{A}_s$. Since the equations are one-dimensional, the resulting computations are fast.

This model was then validated by comparison with finite element computations on idealized trees. It was shown that the homogenized model provides accurate predictions of the internal loads and resulting breakage under flow. The homogenization of the structure smoothens the breakage process, providing results that are closer to the behavior of an actual plant with some randomness in its geometry. An issue remains about recovering the condition for pruning, namely β greater than 1. This problem however occurs for values of β close to 1, and away from 1 the effect of β is consistent with the previous results. Furthermore, whereas for most trees $\beta > 1$ (see Section 2.5), plants that do not undergo flow-induced pruning are mostly cylindrical plants for which $\beta \approx 0$. The present model, though inaccurate on the close vicinity of the value $\beta = 1$, predicts consistent results for most biological structures. Despite the strong assumption made for the model closure, this homogenized method provides a good modeling tool for computing the mechanical response under flow.

The homogenized model developed here presents two major interests. The first one is to allow simple computations on a continuous domain: the general equations are first order ODEs. The second one is that it is possible to generate directly the equivalent homogeneous domain representing a plant or a canopy. Indeed, the one-dimensional description is naturally linked to the beam (or cone) model introduced in the previous Chapters. Moreover, the effect of variability between different elements is well captured by the homogenized model computations. Therefore, one can easily combine the continuous slender cone model and the present model. Such combination is simple to implement, and can lead to analytical expressions for the average fields; the resulting computations are therefore much simpler and faster.

The equivalent representation of any branched slender structure under flow is a bundle of fibers with independent behaviors. Only the three fields $\{\mathbf{t}_s, \varphi, \mathcal{A}_s\}$ are needed, and the refinement in terms of fibers can be adapted to the scale of interest. For instance, for a single tree study it makes sense to have a refinement on a length scale much lower than the trunk diameter, whereas for analyzing a forest the refinement length scale can be of the order of the distance between each individuals. Moreover, considering observations as that of Grant (1983) (see Section 1.2.2), one can adapt the spatial resolution of the problem depending on the flow conditions. This resolution is related to the choice of length scale for the slender cone model and the homogenized model. The representation of vegetation can therefore be done through a homogeneous medium of fibers that verify a particular system of one-dimensional equations, as opposed to previous models that used directly a cylindrical beam representation for each fiber.

Whereas the validation was performed in the particular case of reconfiguration by pruning under uniform flow, the present model can be used in a broader scope. The coupling of this model with a standard flow model should give additional insights on the interaction between a flow and vegetation. Models used for predicting wind damage to forests could be coupled with this homogeneous description, allowing possibly to describe

the type of damage that would occur in a forest under a storm. Taking large deformations into account might however be much more difficult. An idea would be to run the same analysis on the current configuration at each level of deformation, and combine it with an equation for the deformations. The resulting model may require different tools, and as pruning was shown to be robust in the presence of deformations this model can be considered as a generic model for the static response of vegetation to external load.

This model is a first step to a fully coupled flow-plant model, where the initial problem is isostatic. The applications of this model are restrained to static cases, but the simplicity of the resulting model equation present a great advantage. As opposed to most homogenized models that apply to cylindrical fibrous media and tubes (Jacquelin *et al.* 1996, Sigrist & Broc 2008), the complexity of the branched geometry is well captured and the resulting computations provide consistent results. The fully coupled fluid-structure interaction problem can now be considered with this new representation of plants as homogeneous media, and the present model allows one to simplify the study of flow through vegetation to the study of flow through an array of slender fibers or cones.

Chapter 5

Conclusion

5.1 Main contributions

The interactions between terrestrial plants or aquatic vegetation and their surrounding fluid raise major environmental and economic issues. In addition to their long-term adaptability, plants exhibit remarkable behaviors in response to the different type of loads they are submitted to. In this work, we focused on the response of plants to static loads, in order to characterize the different survival strategies in plants. We were interested in the issue of breakage, and for that purpose in modeling accurately the flow-induced loads.

5.1.1 Static reconfiguration of plants

Elastic reconfiguration, first introduced by Vogel (1984), has already been abundantly studied experimentally, numerically and theoretically. It is observed in any deformable structure, and leads to a significant reduction of the flow-induced load compared to that of a non-deformable body. We analyzed in this work whether breakage could act as a similar survival strategy, and be involved in a brittle reconfiguration process.

In order for breakage to be beneficial to the plant, a key condition is that breakage will not occur at the base of the plant. By considering a numerical experiment on an actual geometry, and simple theoretical models, we were able to point out a condition for breakage to occur not at the base of a plant-like structure, hence protecting the vital parts. This condition is a purely geometrical condition, relating the diameter and length of the structure through a slenderness exponent,

$$D \propto L^{\beta}, \quad \beta > 1. \tag{5.1}$$

This condition is in fact satisfied in most trees, for which the deformations are low and breakage is likely to occur under flow. In that case, a process of pruning induced by the flow occurs, where parts of the structure are broken as the fluid velocity increases. This is therefore a scenario of brittle reconfiguration: the structure changes its geometry under the flow, hence reducing the loads it experiences. The load reduction resulting

from pruning is actually more important than that due to bending,

$$T_{\text{bending}} \propto U^{4/3}, \quad T_{\text{pruning}} \propto U, \tag{5.2}$$

where T is the drag and U the flow velocity. Such a result can be seen as a balance to the higher biological cost of losing parts of the plant under flow. Equivalently, this process results in increasing the maximum fluid velocity the structure can sustain before breaking at its base.

In the general case, both deformation and breakage can occur, and the resulting reconfiguration pattern is not trivial. Using the simple models of the flow-induced pruning analysis, we investigated the combination of bending and pruning. In addition to the geometrical condition for pruning – which holds even in the presence of deformations – a mechanical condition was found determining which kind of reconfiguration the structure will undergo. This condition relies on the strain at breakage, compared to the strain at which elastic reconfiguration becomes important. This study showed that, in the case of low strain at breakage ε_c, bending has little effect on the reconfiguration by pruning, whereas in the case of high ε_c breakage affects the reconfiguration only through the maximum acceptable fluid velocity before base breakage.

Considering idealized tree-like geometries, it was shown that any type of reconfiguration – by bending, pruning, or both – leads to very similar drag reduction and gain in maximum sustainable fluid velocity. As the flow velocity increases, deformations occur first, and then breakage; the range over which the bending regime is observed increases with the critical strain. Therefore, in the general case, reconfiguration is a two-step strategy: first bending, and then pruning. Hence pruning drives the reconfiguration at high flow velocities. This suggests that the study of the pruning limit is sufficient for capturing the key features of the static response of plants to an external flow.

It was shown that breakage can act as a reconfiguration strategy, in the same perspective as that of elastic reconfiguration. The latter is clearly reversible in the short term, and has a low biological cost. Brittle reconfiguration, more expensive as the plant looses parts of its structure, is reversible only in the long term by re-growth. The reduction of load resulting from brittle reconfiguration is however more important than that of elastic reconfiguration, hence preserving efficiently the vital parts the plants.

5.1.2 Continuous model for tree-like structures

Modeling complex structures like trees is not trivial, and we were therefore interested in having accurate models for computing the flow-induced loads. Two continuous models were used: the slender cone (or beam) model, inspired from McMahon (1975), and a homogenized model developed in the present work. The cone model captures well the essential ingredients of the geometry of plants and tree-like structures, providing accurate results on the effect of an external flow. However, this model does not allow a fluid-structure interaction analysis.

Considering the results on reconfiguration showing that pruning is equivalent to bending, a continuous porous medium approach was developed in order to model tree-

like structures under flow. The initial problem is isostatic, and the homogenized model was established in the low-deformations case. It was possible to formulate the equations governing the solid behavior in a continuous way in the domain. The resulting equations of the equivalent porous medium showed that the equivalent medium is a bundle of fibers; the diameter of each fiber is related to the volume-averaged diameter. The resulting problem is isostatic, and the mechanical equations are similar to the beam equations, but for an additional term that models the variations in diameter and the branching pattern.

By combining the cone model and the homogenized model, we were able to generate directly the homogeneous domain equivalent to a tree-like structure. The resulting computations are fast and provide accurate results on static reconfiguration. Depending on the scale of interest, one can use the cone model for branches, a group of branches, or a full plant; the homogenized model can then be used for the plant or canopy computations.

This model is only a first step to a fully coupled fluid-structure model, but it holds the key characteristics that drive the structure behavior under flow. The volume description allows one to couple this plant model with a fluid model and provide accurate predictions of flow-plant interaction problems on various scales, from a single plant to a canopy or a forest.

5.2 Perspectives

5.2.1 Experimental validation

Whereas there have been many experimental studies on elastic reconfiguration, there has never been a systematic experimental campaign on flow-induced pruning. Such campaign would provide additional elements for validating the results discussed above, and give informations on possible ameliorations of the models used in this work. However, breaking structures in a controlled environment is a true experimental challenge, that we could not successfully overcome.

The first issue is to find a material that can be easily manipulated in order to generate the specific geometries that undergo pruning. The main problem is that this material should break in a wind tunnel or a flume. The order of magnitude of flow velocity required to break artificial structures is quite high; one must find a high speed wind tunnel or flume. A resin that is easy to manipulate was tested in our facility, but it was too resistant to break under wind flow (limited to 30m.s^{-1}). A solution might be to use foams; such structures can be very brittle – according to our definition – and can possibly break in the wind tunnel in LADHYX. The analysis of Chapter 3 provides informations on the mechanical and geometrical parameters for a test geometry.

A second issue is that one should be able to produce several identical test objects. Indeed, an experiment implying breakage can be conducted only once on a single body. In order for the experiments to be reliable, one should run a large campaign, and the objects should be easy to reproduce. A solution might be to use three-dimensional printing.

5.2.2 Extension of the models

The models and analyses presented in this work can be extended in future studies. The mechanical behavior of plants is not simply linear elastic, and the breakage process is actually more complex than the brittle model used here. Besides, the mechanical properties may vary within a single plant, resulting in different behaviors depending on the localization and biological function of the part of the plant. For instance, as it was mentioned in Section 2.5, the leaves are more likely to reconfigure through bending while the branches of a tree will undergo pruning. Such difference in mechanical response might be also part of a transition strategy, where first the deformable parts of the structure bend under flow, and, if the flow velocity increases further, the brittle parts start to break. Taking into account such extensions should not change significantly the reconfiguration patterns identified in this work, but may provide additional informations on the mechanical response of plants under extreme events. The results can be used for a better management of the risks related to such events. A better predictions of the effect of a storm on a forest might help managing it in a proper way (stand thinning, artificial pruning) and reduce the resulting damages.

The homogenized model developed in this work can first be easily coupled with a stationary flow profile, and in a second stage with a first order fluid model, typically stationary Euler equations with a volume forcing due to the solid. Modifying the medium porosity after a breaking event may become necessary in such applications in order get accurate predictions concerning the flow. On a more fundamental point of view, the continuous model developed in this work could be extended to a wide range of applications. The transportation of any quantity in a ramified network could be modeled using a similar approach. This original approach may be a good way for keeping the key features of the network with a simple model. A limitation of this model relies however in the absence of deformations. Although it was shown that the low-deformation analysis provides consistent results for the effect of the flow on the structure, the effect of drag reduction by clumping effect, as presented in Section 1.2.2, cannot be captured by the homogenized model of this work. Yet, from the results of Gosselin & de Langre (2011) one may assume that the changes in porosity have a second order influence on the loads, and as the porosity in such systems is typically high, the consequences of the solid deformations on the fluid may as well be of second order.

5.2.3 Survival strategy: biological and biomimetic applications

The geometry of a plant is the result of a complex optimization between light interception, resistance to gravity, and flow-induced loads, to cite a few. By combining qualitative observations on the reconfiguration process and systematic measurements of the parameters ε_c and β in various plants, one could get a better understanding on the choices in survival strategy in the context of the different constraints that are applied on plants. As the morphology of an isolated tree differs significantly from that of a tree growing in a forest, it could be interesting to understand how the mechanical constraint due to the wind play a role on the tree growth and development.

Considering how natural structures handle the different constraints that are applied on them, one can get ideas for man-made structures. The results on pruning may have interesting consequences for biomimetic structures, even if breakage is generally avoided. Indeed, a compromise should be found, as broken parts could no longer be used, but having a structure that could undergo both bending and pruning might be a solution for sustaining extreme events. In a first range of flow velocities, the structure would deform in a reversible way; at higher fluid velocities, parts of the structure would break, acting as fuses in order to protect key elements. Such fuses can be considered as a last solution before damaging major functional elements. As breakage in man-made structures is not reversible without intervention, this might be a solution for objects that are not easily accessible and cannot have permanent maintenance; this could be applied for instance to off-shore structures. Looking for inspiration in the survival strategies of plants might give us ideas for artificial structures submitted to similar constraints.

Appendix A

Ideal tree model and equivalent beam

We present in this Appendix the different details related to the ideal tree model introduced first in Section 2.3.

A.1 Finite ideal tree model

We recall here the definitions and notations concerning the ideal tree model of Section 2.3. This sympodial tree is made of cylindrical branches. It can be described using three parameters:
1. the branching ratio λ, giving the reduction of diameter through branching (typically $\lambda < 1$),
2. the slenderness exponent β, giving the relationship for length and diameter evolution in branch segments of the tree (typically $1 < \beta < 2$),
3. the number of branches p emerging from one branch at a branching point, which is typically equal to $1/\lambda$ (Leonardo's rule).

The resulting relations between the branches length and diameter through branching read

$$\lambda = \left(\frac{D_{k+1}}{D_k}\right)^2, \quad \frac{D_{k+1}}{D_k} = \left(\frac{L_{k+1}}{L_k}\right)^\beta, \tag{A.1}$$

where k is the branch level counted from the bottom (see Figure 2.4, p. 20). The expression of each branch segment's dimensions at a level k can be deduced from Equation (A.1),

$$D_k = \lambda^{k/2} D_0, \quad L_k = \lambda^{\frac{k}{2\beta}} L_0, \tag{A.2}$$

where D_0 and L_0 are the diameter and length of the first segment, i.e. the trunk.

A.2 Stress derivation in finite branched tree model

In order to compute the stress along the finite ideal tree, we label the branch levels from the top with an index n, as represented in Figure 2.5 (p. 21). This new notation is related to the label from the bottom k through

$$n = N - k + 1, \tag{A.3}$$

where N is the total number of levels. With these notations, the trunk is now the level N, and its diameter and length are respectively D_N and L_N. As shown in Equation (2.6), the diameter and length at level n read

$$D_n = \lambda^{\frac{N-n}{2}} D_N, \quad L_n = \lambda^{\frac{N-n}{2\beta}} L_N. \tag{A.4}$$

We introduce F_n the fluid force per unit length at level n, $F_n = \frac{1}{2}\rho C_D U^2 D_n$, with the same notations as Equation (2.1). At each level n, we consider two force components: (i) the shear force V_n in the flow direction and (ii) the bending moment M_n in the direction normal to the flow. The free condition at the top gives $V_0 = 0$ and $M_0 = 0$, and for $n \geq 1$

$$V_n = F_n L_n + p V_{n-1}, \tag{A.5}$$

$$M_n = \frac{1}{2} F_n L_n^2 + p\left(M_{n-1} + L_n V_{n-1}\right)., \tag{A.6}$$

The non-dimensional stress σ_n at level n reads

$$\sigma_n = \frac{32 M_n}{\pi \Sigma_c D_n^3} \tag{A.7}$$

By considering $p = 1/\lambda$, the integration of Equations (A.5) and (A.6) give the stress at each level,

$$\sigma_n = C_Y \lambda^{\frac{1-\beta}{\beta} N} \left(A \lambda^{\frac{\beta-1}{\beta} n} + B \lambda^{\frac{n}{2}} + C \lambda^{\frac{\beta-1}{2\beta} n} \right), \tag{A.8}$$

with

$$A = \frac{\lambda^{\frac{1-\beta}{2\beta}} + 1}{\left(\lambda^{\frac{1-\beta}{2\beta}} - 1\right)\left(\lambda^{\frac{2-\beta}{2\beta}} - 1\right)}, \tag{A.9}$$

$$B = \frac{\lambda^{\frac{1}{2\beta}} + 1}{\left(\lambda^{\frac{2-\beta}{2\beta}} - 1\right)\left(\lambda^{\frac{1}{2\beta}} - 1\right)}, \tag{A.10}$$

$$C = \frac{-2}{\left(\lambda^{\frac{1-\beta}{2\beta}} - 1\right)\left(\lambda^{\frac{1}{2\beta}} - 1\right)}, \tag{A.11}$$

and

$$C_Y = \left[\frac{8}{\pi}\left(\frac{L_N}{D_N}\right)^2\right]\frac{\rho C_D U^2}{\Sigma_c}. \tag{A.12}$$

A.3 Equivalent slender beam model

As introduced in Section 3.3.1, there is an equivalent continuous model representing this ideal tree, by adding to the slender cone model a second dimension W transverse to the flow. In this beam model, the width W corresponds to the total spanwise dimension of the tree at a level n, which is the branch diameter at level n multiplied by the number of branches at that level,

$$W_n = p^{N-n} D_n, \quad D_n = \lambda^{\frac{N-n}{2}} D_N. \tag{A.13}$$

These relations can be expressed in a continuous way through a curvilinear coordinate S, whose origin is located at the top of the infinitely iterated tree, S_0 being the coordinate of the top of the finite tree. The coordinate of level n reads

$$S_n = \sum_{i=1}^{n} L_i. \tag{A.14}$$

Using the relation for the length evolution, we get an expression of this coordinate as a function of n

$$\frac{S}{S_0} = \lambda^{\frac{-n}{2\beta}}. \tag{A.15}$$

We have therefore a continuous expression for $W(S)$,

$$W(S) \propto \left(\frac{S}{S_0}\right)^{\beta\left(1+2\frac{\ln p}{\ln \lambda}\right)}. \tag{A.16}$$

Therefore, in the equivalent slender beam the spanwise and streamwise dimensions read respectively

$$W(S) \propto S^{\alpha}, \quad D(S) \propto S^{\beta}, \quad \alpha = \beta\left(1 + 2\frac{\ln p}{\ln \lambda}\right). \tag{A.17}$$

In the case of section conservation (Leonardo's rule), we have $WD = \text{cst}$. This results in $\alpha = -\beta$, which is consistent with $\lambda = 1/p$. This model represents well the stress profile along the tree. An example is provided in Figure A.1, where we recover easily the levels at which breakage occurs computed in Section 2.3.2, p. 20.

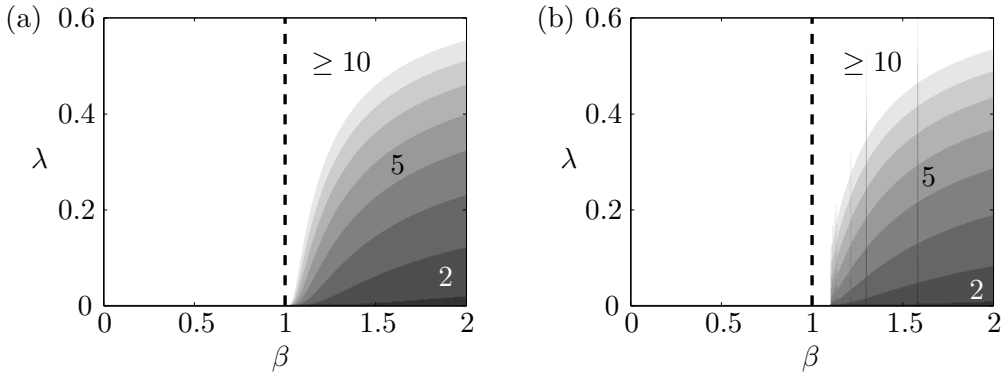

Figure A.1: Levels of maximum stress as a function of the tree parameters β and λ, computed (a) from the discrete tree model and (b) from the continuous beam model. The color levels are the same between the two plots.

Appendix B

Derivation of the beam equations

This appendix explains the derivation of the model equations that are used in Chapters 2 and 3. In order to present the general derivation of the equations, we will consider throughout this appendix the beam model presented in Figure 3.8a, the cone model being in fact a reduction of the beam model to the case $\alpha = \beta$, with a simple scaling resulting from the second moment of inertia.

B.1 General equations

We use here the parametrization presented in Figure 3.1 (p. 30). The beam width and diameter read

$$W(S) = D_0 \left(\frac{S}{L_0}\right)^{\alpha}, \quad D(S) = D_0 \left(\frac{S}{L_0}\right)^{\beta}, \tag{B.1}$$

with D_0 the base diameter, L_0 the cone length from $S = 0$. We keep voluntarily the notation with two different exponents α and β, in order to be able to represent the beam and the cone models. The parameter β is positive ($\beta > 1$ for pruning), but here α can be either negative or positive. The fluid force applied on the beam per unit length reads

$$\mathbf{F} = \frac{1}{2}\rho C_D \left[U \sin\theta(S)\right]^2 W(S)\mathbf{n}, \tag{B.2}$$

where ρ is the fluid density and C_D a constant drag coefficient. As it was presented in Section 3.1.1, the slender beam theory is used here and we have the Euler-Bernoulli equations for the shear force $\mathbf{V} = V_t\mathbf{t} + V_n\mathbf{n}$ and the bending moment M

$$\begin{aligned} &\frac{\mathrm{d}\mathbf{V}}{\mathrm{d}S} + \mathbf{F} = \mathbf{0}, \\ &\frac{\mathrm{d}M}{\mathrm{d}S} + V_n = 0, \\ &EI\frac{\mathrm{d}\theta}{\mathrm{d}S} - M = 0, \end{aligned} \tag{B.3}$$

where E is the Young modulus and I the second moment of inertia, which reads $\pi D^4/64$ for a circular section and $WD^3/12$ for a rectangular one. The bending stress is related to the bending moment through

$$\Sigma = \frac{MD}{2I}. \tag{B.4}$$

The beam is held by a perfect clamping at its base $S = L_0$ with an angle θ_i with respect to the flow, and the top at $S = S_0$ is free ($\mathbf{V} = \mathbf{0}, M = 0$).

In the following sections, the notations will be that of Chapters 2 and 3, small letters will represent non-dimensional values.

B.2 Non-dimensional equations

The details leading to the different non-dimensional equations presented in this work are summarized hereafter. The vectorial equation in Equation (B.3) can be decomposed along the two local vectors $(\mathbf{t}, \mathbf{n})$ (Figure 3.1, p. 30), using

$$\frac{\mathrm{d}\mathbf{t}}{\mathrm{d}S} = \frac{\mathrm{d}\theta}{\mathrm{d}S}\mathbf{n}, \quad \frac{\mathrm{d}\mathbf{n}}{\mathrm{d}S} = -\frac{\mathrm{d}\theta}{\mathrm{d}S}\mathbf{t}. \tag{B.5}$$

The non-dimensional formulation of the beam equations rely on different choices. The first choice is that of the reference length scale for the curvilinear coordinate, L_0 or S_0; the second on the reference mechanical parameter, E or Σ_c. The first will be taken to be L_0 in this Section, and the choice of the truncation length as a reference length scale will be the object of Section B.3.1. On the other hand, in order to provide interpretations of the equations in the pruning and bending limit, the resulting equations will be presented using both the modulus of elasticity E and the critical yield stress Σ_c as reference quantities.

B.2.1 Reference parameters and Cauchy number

In the pruning (and respectively bending) limit, the Young Modulus E (resp. the critical stress Σ_c) does not play any role. Therefore, it makes sense to use Σ_c as a reference load in the pruning limit, and E in the bending limit. We present in Table B.1 the non-dimensional equations in each limit. The scaling parameter that appears in the equation of the shear force v_n is called in both case "Cauchy number", as it contains all the scaling between the fluid load and the mechanical response of the body. The term noted I_0 corresponds to the second moment of inertia at the base of the beam.

When considering a cone with circular cross-section (and $\alpha = \beta$), the system leads exactly to the same set of equations, with a change in the Cauchy number due to the term I_0

$$C_Y^{\text{cone}} = \frac{16}{3\pi} C_Y^{\text{beam}}, \tag{B.6}$$

which is valid for both $\widehat{C_Y}$ and $\widetilde{C_Y}$, as defined in Table B.1.

	Pruning limit	Bending limit
Reference force	$\frac{2I_0\Sigma_c}{L_0 D_0}$	$\frac{EI_0}{L_0^2}$
Reference moment	$\frac{2I_0\Sigma_c}{D_0}$	$\frac{EI_0}{L_0}$
Equations	$v_n' + \widehat{C_Y}\sin^2\theta_i s^\alpha = 0$ $m' + v_n = 0$ $\sigma = m s^{-\alpha-2\beta}$	$v_n' + \theta' v_t + \widetilde{C_Y}\sin^2\theta s^\alpha = 0$ $v_t' - \theta' v_n = 0$ $\theta'' + (\alpha+3\beta)s^{-1}\theta' + s^{-(\alpha+3\beta)}v_n = 0$
Cauchy number	$\widehat{C_Y} = 3\frac{\rho C_D U^2}{\Sigma_c}\left(\frac{L_0}{D_0}\right)^2$	$\widetilde{C_Y} = 6\frac{\rho C_D U^2}{E}\left(\frac{L_0}{D_0}\right)^3$

Table B.1: Reference quantities and corresponding non-dimensional equations in the pruning and bending limit. The symbol $'$ denotes the derivative with respect to the non-dimensional curvilinear coordinate $s = S/L_0$.

The two Cauchy numbers identified in Table B.1 scale the reconfiguration process, be it by pruning or bending. When comparing the two expression, one can observe that the normalized critical strain ε_c introduced in Chapter 3 is in fact the ratio of these two Cauchy numbers,

$$\varepsilon_c = \frac{\widetilde{C_Y}}{\widehat{C_Y}}. \tag{B.7}$$

Hence, $\varepsilon_c \ll 1$ means that the Cauchy number scaling the pruning process is much higher than that of the bending process, the structure will undergo pruning before bending, as it was pointed out in Chapter 3.

B.2.2 Particular case of low deformations

In the pruning limit, the angle θ is constant, equal to the clamping angle θ_i. Therefore the equations can be integrated analytically, resulting in (for $\alpha \neq \{-1; -2\}$)

$$v_n = -\widehat{C_Y}\sin^2\theta_i \frac{s^{\alpha+1} - s_0^{\alpha+1}}{\alpha+1}, \tag{B.8}$$

$$m = \widehat{C_Y}\sin^2\theta_i \frac{s^{\alpha+2} - (\alpha+2)s_0^{\alpha+1}s + (\alpha+1)s_0^{\alpha+2}}{(\alpha+1)(\alpha+2)}, \tag{B.9}$$

$$\sigma = \widehat{C_Y}\sin^2\theta_i \frac{{s_0}^{2(1-\beta)}}{(\alpha+1)(\alpha+2)}\mathrm{P}\left[s/s_0\right], \tag{B.10}$$

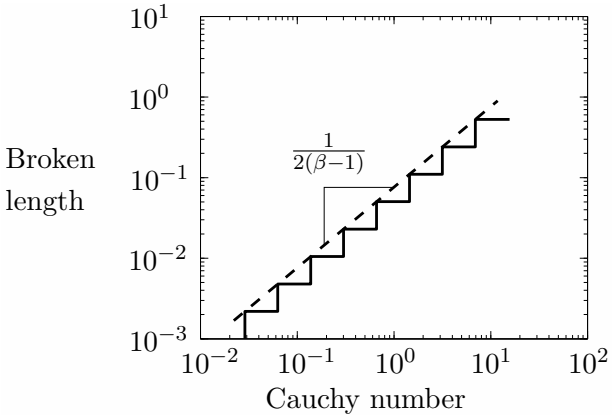

Figure B.1: Evolution of the broken length of the slender cone with respect to the Cauchy number. The solid line represents the exact evolution for a random initial truncation s_0.

where

$$\mathrm{P}\left[s/s_0\right] = \left(\frac{s}{s_0}\right)^{2(1-\beta)} - (\alpha+2)\left(\frac{s}{s_0}\right)^{1-\alpha-2\beta} + (\alpha+1)\left(\frac{s}{s_0}\right)^{-\alpha-2\beta}. \tag{B.11}$$

For a slender cone clamped with an angle $\theta_i = \pi/2$, Equation (B.10) leads to Equations (2.10), (2.11) and (2.13) in Section 2.4.1 (p. 23).

One can note from the previous equations that the case $s_0 = 0$ leads to a singularity if α is negative, as it is the case in the beam model. Thus, for $\alpha < 0$, the condition for the existence of a maximum of stress, located not at the base, cannot be easily identified as it was the case for the cone model. However, a numerical analysis on the expression of the stress shows that the necessary condition for pruning $\beta \geq 1$ still holds for the slender beam model, for any value of α. This is indeed consistent with the analysis of Section 2.3, showing that branching plays a role only in the location of the maximum of stress.

The general form of σ shows that the maximum of stress will be reached at a constant s/s_0 value noted ζ, which is only a function of α and β. Hence in the low deformation computations the flow-induced stress state follows self-similar solutions depending on the initial truncation s_0. The cone broken length (under the pruning process) will follow therefore a simple power law dependency with the Cauchy number, which is found by solving

$$\sigma\left(C_Y, s_0, s = \zeta s_0\right) = 1, \tag{B.12}$$

with s_0 as unknown. This scaling law – shown in Figure B.1 – provides a relation for the height of the shortest and highest beams that can exist at each Cauchy number, for the computation of the envelope curves in Figures 2.9 (p. 25) and 3.5 (p. 37).

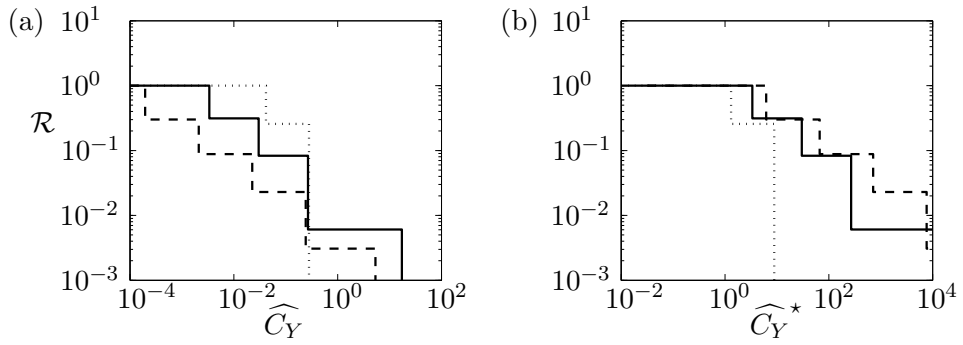

Figure B.2: Effect of considering S_0 as a reference length scale on the pruning reconfiguration curves, for three values of β, in the case $\alpha = -\beta$: $\beta = 1.25$ (dotted line), $\beta = 1.5$ (solid line) and $\beta = 1.75$ (dashed line). (a) Cauchy number scaled with L_0, (b) Cauchy number scaled with S_0.

B.3 Role of the truncation in the slender beam model

B.3.1 Reference length scale for non-dimensional equations

As mentioned in Section 3.3.1, the length scale chosen for the non-dimensional values deserves some discussion. Indeed, when α is negative the fluid force tends to infinity as S_0 tends to 0. Therefore, the internal loads are likely to be scaled by S_0 rather than L_0.

If the reference length scale is chosen to be the truncation S_0, the resulting equations in both pruning and bending limits are identical to that of Table B.1, but for a new Cauchy number noted with an exponent * which read

$$\widetilde{C_Y}^{\star} = \left(\frac{S_0}{L_0}\right)^{3(1-\beta)} \widetilde{C_Y}, \tag{B.13}$$

$$\widehat{C_Y}^{\star} = \left(\frac{S_0}{L_0}\right)^{2(1-\beta)} \widehat{C_Y}. \tag{B.14}$$

As it is shown in Figures B.2 and B.3, this scaling is actually the relevant scaling for the loads in the structure and thereby for scaling the reconfiguration. The reconfiguration by pruning starts for $\widehat{C_Y}^{\star} \sim 1$ and not $\widehat{C_Y} \sim 1$, and it is also the case for the reconfiguration by bending. Note that the asymptotic slope in the reconfiguration by bending is independent of β, as expected from the scaling found in Section 3.2.2

The normalized critical strain, which corresponds actually to the ratio of the Cauchy numbers of deformation and breakage, is also modified by the scaling of the equations with S_0, leading to

$$\varepsilon_c{}^{\star} = \frac{\widetilde{C_Y}^{\star}}{\widehat{C_Y}^{\star}} = \left(\frac{S_0}{L_0}\right)^{1-\beta} \frac{2L_0}{D_0}\frac{\Sigma_c}{E}. \tag{B.15}$$

In Section 3.3.1, the different results were presented with the Cauchy number $\widehat{C_Y}^{\star}$ and

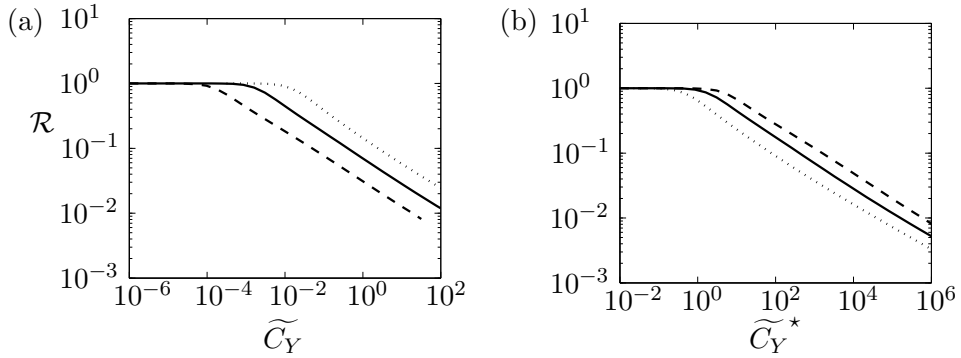

Figure B.3: Effect of considering S_0 as a reference length scale on the bending reconfiguration curves, for three values of β, in the case $\alpha = -\beta$: $\beta = 1.25$ (dotted line), $\beta = 1.5$ (solid line) and $\beta = 1.75$ (dashed line). (a) Cauchy number scaled with L_0, (b) Cauchy number scaled with S_0.

normalized strain at breakage $\varepsilon_c{}^\star$, though without changing the notations for clarity.

B.3.2 Influence of the truncation at finite critical strain

The effect of s_0 can be quite important. In Section 3.2.1, it is mentioned that above a particular critical strain, the effect of the truncation on the reconfiguration curves is not visible. In fact, this particular threshold is dependent on the choice of the maximum value of s_0. Figure B.4 shows the superimposition of 10 reconfiguration curves obtained for 10 values of the truncation s_0 from 0.05 to 0.5, at a critical strain $\varepsilon_c = 0.5$. We observe that for $s_0 \leq 0.2$, the reconfiguration curves follow almost a single curve. Therefore, at higher values of the critical strain, the reconfiguration curves for $s_0 \leq 0.2$ will be identical to that of the cone for which $s_0 = 0.2$. In that case, the variability induced by the truncation is lost, and the resulting curve is directly related to the arbitrary choice of the maximum value for the truncation.

When ε_c is close to $\varepsilon_c^{\text{prun}}$, a singular behavior can be observed: the location of maximum stress gets close to the bottom, and the structure will not break at the base. It is then possible to have a remaining structure as small as possible, leading to a value of C_Y^{last} as high as possible. Since this behavior is not physically relevant, we avoid this issue by varying s_0 over the total length of the cone, i.e. $s_0 \in [0; 1]$ for the computation of the maximum sustainable Cauchy number. The value of this Cauchy number is obtained by choosing for all values of s_0 the minimum value of the Cauchy number at which base breakage occurs.

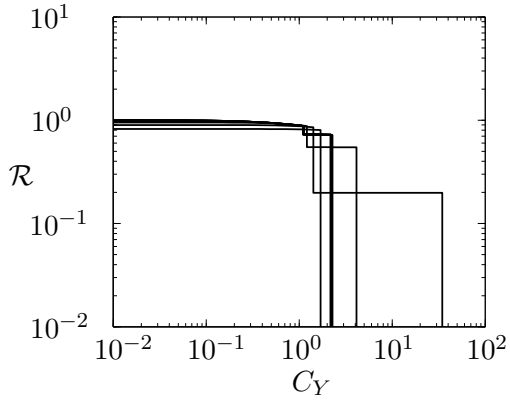

Figure B.4: Effect of the truncation on the reconfiguration curves, for $\beta = 1.5$ and $\varepsilon_c = 0.5$. The different curves correspond to different values of s_0, from 0.05 to 0.5. We observe that for $s_0 \leq 0.2$ the curves follow a single reconfiguration curve, whereas for higher values the curves are different.

Appendix C

Additional material to Chapter 3

C.1 Scaling of the maximum acceptable Cauchy number

In Figure 3.6, a clear asymptotic behavior is observable at high values of the critical strain ε_c. This corresponds to the case where the bending asymptotic regime is reached before the structure breaks at its base. By analogy with the scaling found in Section 3.2.2 for the reconfiguration number, we apply the analysis of de Langre *et al.* (2012) in the bending asymptotic regime. The bending moment scales therefore as

$$M_B \propto \widetilde{C_Y}^{1/3}. \tag{C.1}$$

The strain at the base is proportional to the bending moment at the base through a geometrical factor. One can therefore extract the scaling for the Cauchy number at which base breakage occurs with respect to ε_c, by writing

$$\varepsilon_c \propto \left(\widetilde{C}_Y^{\text{last}}\right)^{1/3}. \tag{C.2}$$

As $\widetilde{C_Y} \sim \varepsilon_c C_Y$ (see Appendix B.2), we obtain

$$C_Y^{\text{last}} \propto \varepsilon_c^2, \tag{C.3}$$

which is observed for high ε_c values.

C.2 Evolution of the gain in Cauchy number

The schematic view of the reconfiguration processes shown in Figure 3.7 is in fact a summary of the key features emerging from the evolution of the maximum sustainable Cauchy number as a function of the two parameters of the problem: the critical strain ε_c, which characterizes the structure mechanical behavior, and the slenderness exponent β that defines the cone geometry. The exact evolution of C_Y^{last} is shown in Figure C.1, where the contour lines correspond to a logarithmic scale.

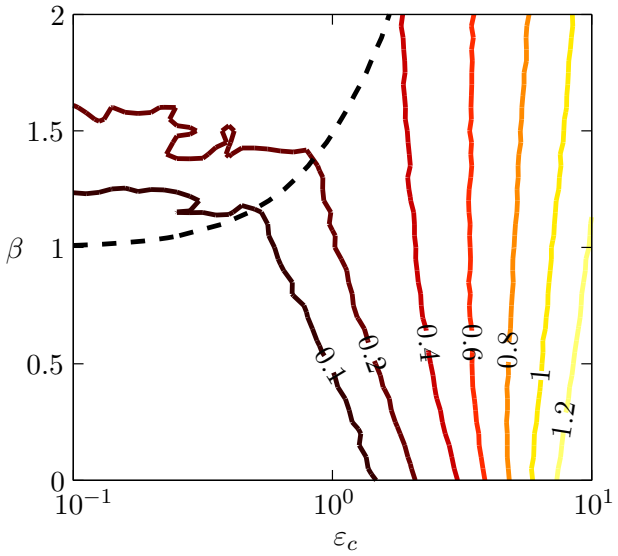

Figure C.1: Contour values of the maximum sustainable Cauchy number C_Y^{last} as a function of the two parameters describing the mechanical behavior and the geometry, ε_c and β. The contour values correspond to $\log_{10}(C_Y^{\text{last}})$. The dashed line represents the threshold value $\varepsilon_c^{\text{prun}}(\beta)$ after which only bending occurs. The curves of Figure 3.6 correspond to the evolution of C_Y^{last} along a horizontal line at $\beta = 0.5$ and $\beta = 1.5$.

We observe the different behaviors summarized in Figure 3.7. In the pruning region, the apparent fluctuations of the contour lines are only due to numerical limitations, as one need to find the minimum value of C_Y^{last} for all possible values of the truncation s_0. At high critical strain, the contours are not exactly vertical, as the slenderness β is in fact included in the Cauchy number.

C.3 Scaling of drag reduction for the cone bundle in the pruning limit

An asymptotic regime appears at high Cauchy number when $\varepsilon_c \ll 1$ (Figure 3.11a, sketch C). In that case, the center cones are being broken at their base, and an "empty" region propagates from the center of the bundle. The limit angle θ_{lim} of that inner region (see Figure 3.11 sketch C) can be determined considering the Cauchy number at which the cones break at their base, namely $C_Y^{\text{last}}(\theta_i)$. Since all cones are identical, all cones will break at the same effective Cauchy number. $C_Y^{\text{last}}(\theta_i)$ can therefore be expressed as a function of the Cauchy number for base breakage of the vertical cone $C_Y^{\text{last}}(\pi/2)$, as

$$C_Y^{\text{last}}(\theta_i)\sin^2\theta_i = C_Y^{\text{last}}\left(\frac{\pi}{2}\right). \tag{C.4}$$

The limit angle $\theta_{\lim}(C_Y)$ is such that the effective Cauchy number for the cone clamped at $\theta_i = \theta_{\lim}(C_Y)$ is equal to $C_Y^{\text{last}}(\pi/2)$, which leads to

$$\sin^2(\theta_{\lim}(C_Y)) = C_Y^{\text{last}}\left(\frac{\pi}{2}\right)\frac{1}{C_Y}. \tag{C.5}$$

On the other hand, in the pruning limit, the maximum drag of a cone clamped at $\theta_i = \pi/2$ is proportional to the flow velocity (see Section 3.2.2). This drag is in fact the shear force V_n at the base of the cone. For a cone clamped with an angle θ_i, we have the same dependence with the normal – or effective – flow velocity $U\sin\theta_i$,

$$V_n(\theta_i) \propto U\sin\theta_i. \tag{C.6}$$

The drag T_i of this cone (i.e. the fluid force in the flow direction) is the projection of $V_n(\theta_i)\mathbf{n}$ along the flow direction (note that in the pruning limit $V_t \equiv 0$)

$$T_i \propto U\sin^2\theta_i \sim C_Y^{1/2}\sin^2\theta_i. \tag{C.7}$$

At high Cauchy numbers, the angles are small, allowing us to write $\sin\theta \sim \theta$. The total drag of the cone bundle is therefore the summation over each cone of its drag, from $\theta = 0$ to $\theta_{\lim}$ (and symmetrically from $\theta = \pi$ to $\pi - \theta_{\lim}$), resulting in

$$T_{\text{bundle}} \sim \int_0^{\theta_{\lim}} C_Y^{1/2}\theta_i^2 \mathrm{d}\theta_i \sim C_Y^{1/2}\int_0^{C_Y^{-1/2}} \theta_i^2 \mathrm{d}\theta_i. \tag{C.8}$$

Since the reconfiguration number is proportional to the drag divided by the Cauchy number, we get

$$\mathcal{R} \sim C_Y^{-2}, \tag{C.9}$$

which is verified from the numerical computations at low critical strain and high Cauchy number, Figure 3.11a. This result provides a validation of the interest of looking at the upper bound of the drag in the pruning limit in order to get a general scaling of the reconfiguration by pruning.

Appendix D

Homogenization: technical points

We present here some issues on the model derivation of Chapter 4, and how they are overcome. These are related to the branching regions and averaging volume border.

When introducing a branch volume in the one-dimensional beam representation in Section 4.2.1, a singularity appears at the branching points, concerning the definition of the continuous quantity $q(s, \mathbf{p})$, Figure D.1a. In order to overcome that singularity, the branching point is extended to a region whose typical length scale is the diameter of the branches D. Over this region the branching relations are conserved between O^- and O^+ (see Figure D.1a). The function q is therefore unknown in the branching region. However, this region has a volume that scales as D^3, and $D \ll L$ (the branch length), due to the branch slenderness. The length scale of Ω being at least of the order of L, the volume represented by the branching regions is negligible compared to the solid volume Ω_s and the total volume Ω.

The initial model being that of a beam, considering the branches to have a non-zero volume is consistent only if any intersection between a plane and a branch occurs in the plane normal to the branch direction. Indeed, in the beam description, the quantity Q takes a single value at an intersection with a plane. However, if the angle between the plane and the beam is not $\pi/2$, q can take different values at the intersection. This is sketched in Figure D.1b, which shows this artifact of the three-dimensionalization

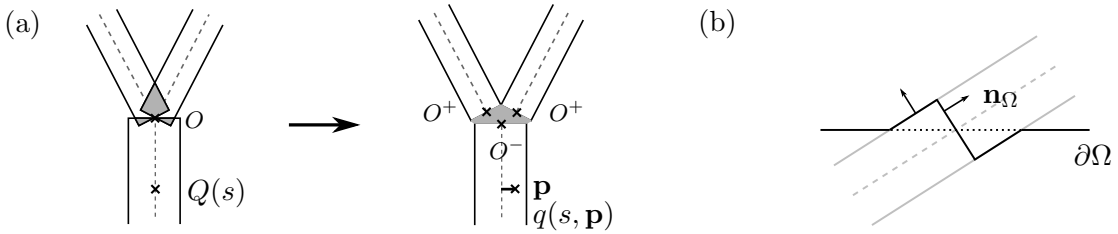

Figure D.1: Averaging notations and hypothesis: (a) branching point representation; (b) adapted averaging volume border $\partial\Omega$ in solid line, compared to the initial border in dotted line.

occurring at the borders $\partial\Omega$ of the averaging volume. This issue is bypassed considering a modified border, shown in solid line in the sketch of Figure D.1b. The modification in volume that this adaptability will add is again negligible compared to the total volume Ω, since it scales as D^2L.

Appendix E

Publication

Lopez, D., Michelin, S. & de Langre, E. 2011 Flow-induced pruning of branched systems and brittle reconfiguration. *Journal of Theoretical Biology* **284** (1), 117 – 124.

Journal of Theoretical Biology 284 (2011) 117–124

Contents lists available at ScienceDirect

Journal of Theoretical Biology

journal homepage: www.elsevier.com/locate/yjtbi

Flow-induced pruning of branched systems and brittle reconfiguration

Diego Lopez, Sébastien Michelin, Emmanuel de Langre *

Department of Mechanics, LadHyX, Ecole Polytechnique-CNRS, 91128 Palaiseau, France

ARTICLE INFO

Article history:
Received 29 March 2011
Received in revised form
7 June 2011
Accepted 22 June 2011
Available online 29 June 2011

Keywords:
Wind-loading
Allometry
Tree-like structure
Bending stress
Branch breakage

ABSTRACT

Whereas most plants are flexible structures that undergo large deformations under flow, another process can occur when the plant is broken by heavy fluid-loading. We investigate here the mechanism of such possible breakage, focusing on the flow-induced pruning that can be observed in plants or aquatic vegetation when parts of the structure break under flow. By computation on an actual tree geometry, a 20-yr-old walnut tree (*Juglans Regia L.*) and comparison with simple models, we analyze the influence of geometrical and physical parameters on the occurrence of branch breakage and on the successive breaking events occurring in a tree-like structure when the flow velocity is increased. We show that both the branching pattern and the slenderness exponent, defining the branch taper, play a major role in the breakage scenario. We identify a criterion for branch breakage to occur before breakage of the trunk. In that case, we show that the successive breakage of peripheral branches allows the plant to sustain higher flow forces. This mechanism is, therefore, similar to elastic reconfiguration, and can be seen as a second strategy to overcome critical events, possibly a widespread solution in plants and benthic organisms.

1. Introduction

Most living systems are surrounded by a fluid, be it air or water. When this fluid flows, it generates mechanical forces, that may have major consequences on growth as well as on reproduction or survival (Moulia et al., 2006; Koehl et al., 2008; de Langre, 2008). Typical cases are trees subjected to wind or corals subjected to water currents. In terms of flow-induced deformations, two typical behaviors can be pointed out. In the most common one, the solid undergoes large elastic deformations, for instance in crops or aquatic vegetation. In the second type, the system breaks before any significant deformation can occur; this will be referred to as brittle behavior in the following. The former has been abundantly studied, a key result being that of load reduction by elastic reconfiguration (Vogel, 1989; Gosselin et al., 2010). The latter has already been described in trees or corals (Koehl, 1984; Niklas and Spatz, 1999), but to the best of our knowledge the effect of branching has never been studied theoretically. Therefore, we shall focus hereafter on brittle branched slender systems, which are ubiquitous in nature: trees (McMahon, 1975), bushes, algae (Koehl, 1984), corals (Madin, 2005) and corallines (Martone and Denny, 2008), to list a few. In the following we refer mainly to trees under wind loading, with the understanding that these results are also applicable to a large variety of other biological systems under fluid-loading.

For a brittle branched system attached to a support, breakage under flow may occur in three distinct types: (i) base breakage, Fig. 1a, when the attachment to the ground is broken, as in uprooting, (ii) trunk breakage, Fig. 1b, when the main element is broken, and (iii) branch breakage, Fig. 1c, when an upper element breaks, as in flow-induced pruning.

In fact, the distinction between trunk and branch breakage has a biological relevance, since breakage of the trunk is likely to be fatal, while re-growth is often possible after branch breakage. Moreover, branch breakage does reduce loads on the trunk and the attachment, as in elastic reconfiguration, thereby delaying their breakage (Koehl, 1984; Niklas and Spatz, 2000). Finally, branch breakage can also be part of the asexual reproduction process by propagation. This is observed in terrestrial plants such as willows and poplars (Beismann et al., 2000), and in stony corals such as *Acropora Cervicornis* or *Acropora Palmata* (Tunnicliffe, 1981; Highsmith, 1982).

Breakage is the consequence of an unacceptable stress level; it is, therefore, directly related to the stress state in the structure (Niklas and Spatz, 2000; Gardiner and Quine, 2000). In particular, the issue of whether the stress level is uniform or not in the tree is crucial, as breakage is expected to occur at the point of maximal stress. For instance, Niklas and Spatz (2000) showed that in a cherry tree the stress level varies by one to two orders of magnitude within the tree and has a local maximum in the branches. On the other hand, Bejan et al. (2008) showed that the flow-induced stress is uniform for a tapered trunk when the taper is linear. In fact the stem taper is an important parameter regarding the stress distribution; see the discussion in Larjavaara (2010).

* Corresponding author.
E-mail addresses: lopez@ladhyx.polytechnique.fr (D. Lopez), sebastien.michelin@ladhyx.polytechnique.fr (S. Michelin), delangre@ladhyx.polytechnique.fr (E. de Langre).

0022-5193/$ - see front matter © 2011 Elsevier Ltd. All rights reserved.
doi:10.1016/j.jtbi.2011.06.027

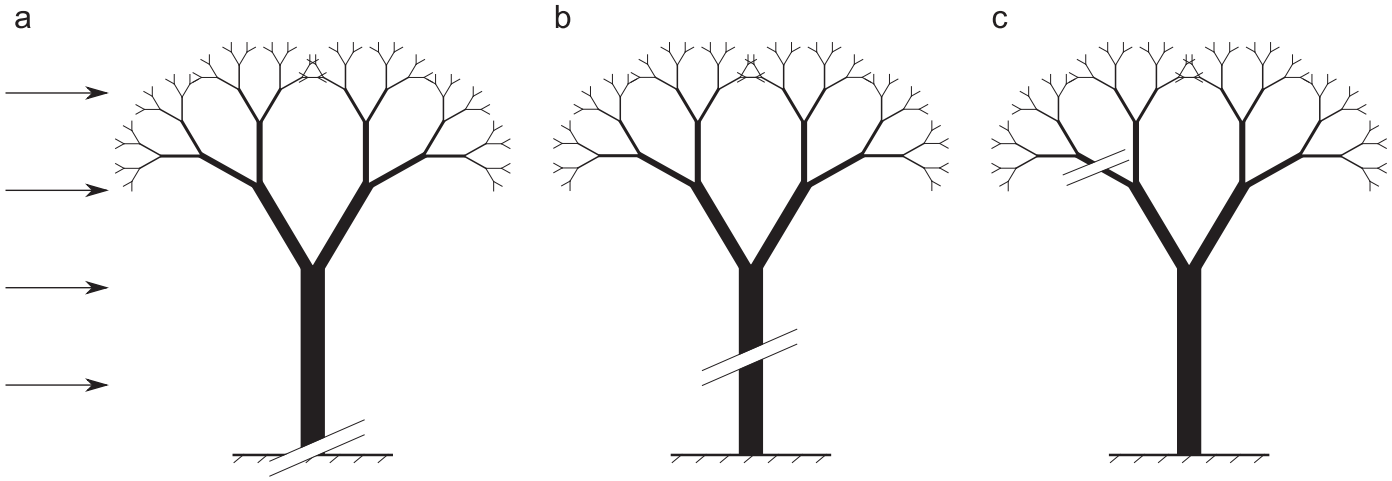

Fig. 1. Schematic view of breakage process in a branched brittle system under flow. (a) Base breakage, (b) Trunk breakage, (c) Branch breakage.

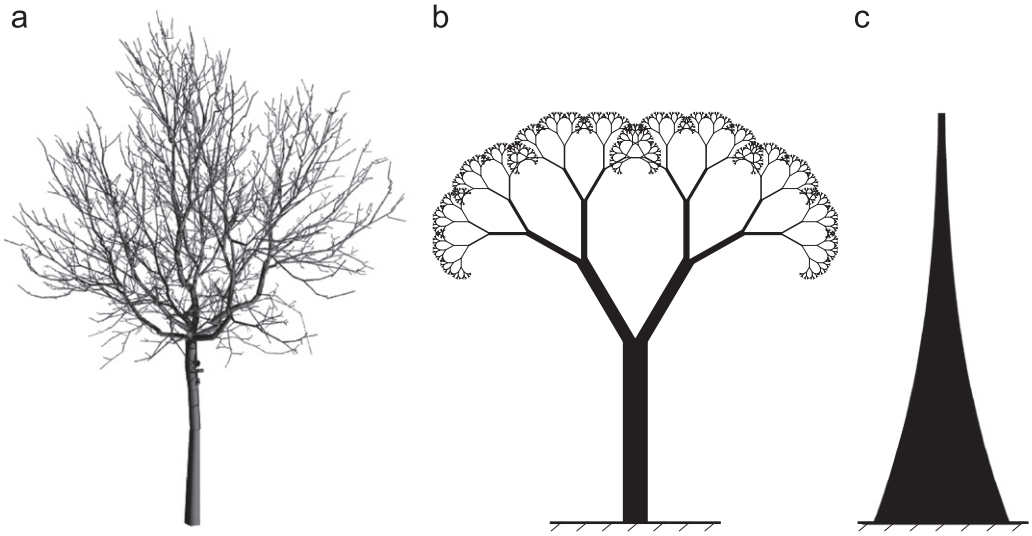

Fig. 2. Geometries of the models used in the paper: (a) Section 3: Walnut tree, as in Sinoquet et al. (1997); (b) Section 4: Idealized branched system, as in Rodriguez et al. (2008); (c) Section 5: Tapered beam, as in McMahon (1975) and Bejan et al. (2008).

Several questions remain, however, regarding the flow-induced breakage of tree-like structures: (i) what are the effects of the geometrical and physical parameters on the occurrence of branch breakage? (ii) How do the breaking events occur successively as the flow is increased? (iii) Assuming that branch breakage is favorable in biological terms, is it compatible with other constraints on the geometry? The aim of this paper is to address these questions, using simple numerical and analytical models for the mechanical behavior of slender and brittle structures. The modeling assumptions and framework used throughout the paper are first presented in Section 2. In Section 3, we compute the stress distribution and successive breaking events in a complex tree, using the geometry of an actual walnut tree. Using an idealized branched system, we derive conditions for branch breakage in Section 4. These are further analyzed for a tapered beam, here referred to as the slender cone model, in Section 5. The corresponding three geometries are sketched in Fig. 2. Finally a general discussion and conclusion are given in Section 6.

2. Mechanical model and parameters

Throughout the paper, we consider a cross-flow over the entire structure, uniform, as the dependence of the stress on the wind velocity profile was shown to be small (Niklas and Spatz, 2000). Also, only static loads are taken into account, and the corresponding fluid force magnitude f per unit length reads

$$f = \tfrac{1}{2}\rho C_D D U^2, \tag{1}$$

where U is the free stream velocity, ρ its density, D the local branch diameter and C_D the drag coefficient (de Langre, 2008; Madin and Connolly, 2006). The direction is assumed to be that of the flow velocity. The fluid load is here computed on a leafless branch, and the influence of leaves will be discussed in Section 6.

This load is applied on the whole branched system, which is held by a perfect clamping at the base. Because of the high slenderness of the system, we use a standard linear beam theory to derive the stress state, essentially the bending moment M. The maximum stress in the cross-section resulting from this bending moment is the skin stress, defined as $\Sigma = 32M/\pi D^3$ (Niklas, 1992; Gere and Timoshenko, 1990).

The brittle behavior is introduced as follows: (i) the deformations are assumed to be negligible, so the stress state is computed on the initial configuration, without elastic reconfiguration, (ii) when increasing the flow velocity U, breakage occurs when and where the local skin stress Σ reaches a critical value, Σ_c. Then, the broken branch is removed, and this results in a new flow-induced

stress state. Flow velocity may then be further increased until a new breaking event occurs.

Throughout the paper, the relevant dimensionless number to scale the fluid-loading $\rho C_D U^2$ with respect to the critical stress Σ_c is the Cauchy number, defined as

$$C_Y = \frac{\rho C_D U^2}{\Sigma_c} G, \tag{2}$$

where G is a geometrical factor introduced for comparison purpose and defined such that $\Sigma = \Sigma_c$ at the base of the intact structure when $C_Y = 1$. Note that this Cauchy number is similar in principle but differs from that used in the analysis of flow-induced elastic deformation, namely $C_Y = \rho C_D U^2 / E$ (de Langre, 2008; Gosselin et al., 2010); the critical stress Σ_c simply replaces here the Young modulus E.

The non-dimensional stress is defined as $\sigma = \Sigma / \Sigma_c$ and the non-dimensional bending moment as $m = M/M_c$, with $M_c = \Sigma_c \pi D_B^3/32$, D_B being the base diameter (Niklas, 1992). This latter scaling is chosen so that failure occurs at the base of the trunk when $m = 1$. The non-dimensional vertical coordinate z is defined using H, the height of the structure, as a reference length scale.

3. Flow-induced pruning of a walnut tree

The geometry of the branched system is expected to have a large influence on the stress state and thus on the location and timing of breaking events. We, therefore, first apply the procedure described above using the digitized geometry of an actual 20-yr-old walnut tree (*Juglans Regia L.*) described in Sinoquet et al. (1997) (Fig. 2a). This tree is 7.9 m high, 18 cm in diameter at breast height (dbh), and has a sympodial branching pattern (Barthelemy and Caraglio, 2007) and about eight orders of branching. The stress state under flow is computed using a standard finite element software (CASTEM v. 3 M, Verpeaux et al., 1988), and is presented in Fig. 3b for four different branching paths.

We observe that the stress level is not uniform but shows a maximum located in the branches, which is consistent with the results of Niklas and Spatz (2000) which are sketched in Fig. 3a. Note that since σ varies linearly with the fluid-loading C_Y, one needs only to focus on the critical situation where $\sigma = 1$ is first reached in the structure. In this tree, the criterion for breakage is satisfied first in a branch and not in the trunk. This corresponds to the mechanism of branch breakage, as defined in Section 1. If the fluid-loading is further increased after removal of the broken parts, successive breaking events are observed, in a flow-induced pruning sequence: Fig. 4a shows three states of the tree at increasing Cauchy number with branches progressively removed as they break off.

During the sequence of breakage, the bending moment at the base of the tree, m_b, evolves significantly with the Cauchy number, Fig. 4b. Up to the first breakage, the moment is proportional to the fluid-loading C_Y (zone I in Fig. 4b). Then, in a small range of load increase (zone II), all large branches are broken at an intermediate level, resulting in a significant decrease of the bending moment. Breakage then continues but to a much smaller extent (zone III), while the moment increases almost linearly up to the value $m_b = 1$ when the trunk breaks. Note that the benefit of this sequence of breaking events is that the critical value of the base moment $m_b = 1$ is reached only at $C_Y \simeq 10$ instead of $C_Y = 1$ if there was no branch breakage. This corresponds to more than a factor of 3 on the acceptable fluid velocity. For instance, for a critical stress $\Sigma_c = 40$ MPa, which is the order of magnitude of maximum acceptable bending stresses measured in trees (Beismann et al., 2000; Lundström et al., 2008), the maximum sustainable fluid velocity before trunk breakage is increased from $U \simeq 30\ \mathrm{m\,s^{-1}}$ without branch breakage to $U \simeq 100\ \mathrm{m\,s^{-1}}$ with branch breakage.

To summarize, this set of computations clearly shows that branch breakage can occur prior to trunk breakage, and that the sequence of flow-induced pruning results in a significant reduction in the load applied on the base of the tree, or equivalently, an increase in the sustainable fluid velocity. To further analyze this process, we turn to a simple model in the next section.

4. The ideal tree model

4.1. Infinite branched tree

To establish the relation between the parameters of the system and the flow-induced pruning process, we simplify the problem to its essential elements: the branched geometry and the slenderness of branches; we disregard here the effect of branch orientation relative to the flow. Similarly to Rodriguez et al. (2008),

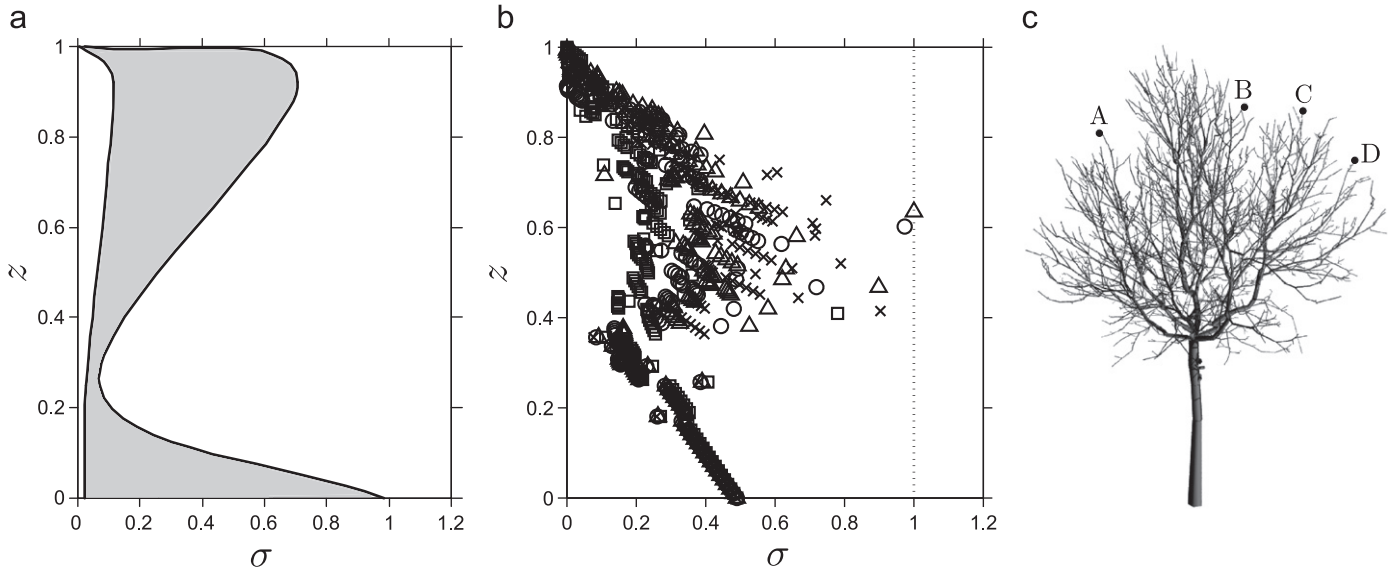

Fig. 3. Non-dimensional stress profile σ in a tree under cross-flow. (a) Schematic view of the stress profiles given by Niklas and Spatz (2000) for cherry trees, showing a local maximum near the top. (b) Computed stress profiles along four branching paths, A (×), B (□), C (△) and D (○) in the digitized tree geometry shown in (c).

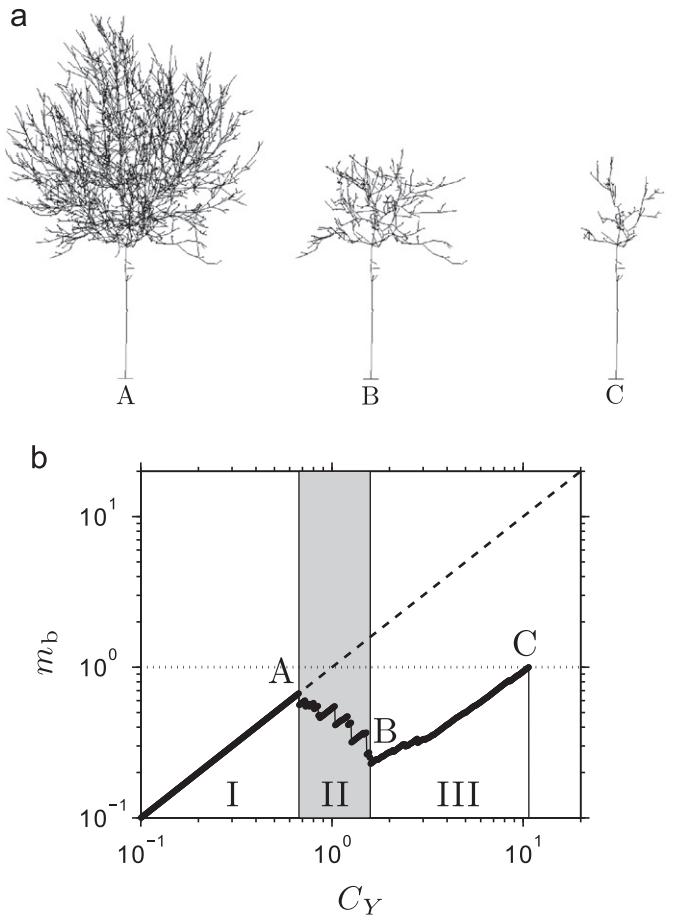

Fig. 4. Computed sequence of branch breakage in the walnut tree: (a) A: initial tree for $C_Y \leq 0.67$; B: after breakage in large branches, $C_Y = 1.7$; C: just before trunk breakage, $C_Y = 10.7$. (b) Corresponding evolution of the bending moment at the base of the tree m_b, in three distinct ranges. The dashed line shows the moment that would exist without breakage. The dotted line shows the critical value m_b that causes trunk breakage.

we consider first an infinitely iterated sympodial tree made of cylindrical branches (Fig. 5). Two parameters only are needed to describe this ideal tree: (i) the branching ratio λ, giving the reduction of diameter through branching, and (ii) the slenderness exponent β, giving the relationship between length and diameter in branch segments of the tree, so that

$$\lambda = \left(\frac{D_{k+1}}{D_k}\right)^2, \quad \frac{D_{k+1}}{D_k} = \left(\frac{L_{k+1}}{L_k}\right)^\beta, \tag{3}$$

where D_k and L_k are the diameter and length of a branch segment of order k, see Fig. 5a (Rodriguez et al., 2008). Typical values of these parameters are $\lambda < 1$ and $1 < \beta < 2$. Note that the number of branches emerging from a branching point is typically equal to $1/\lambda$ (Lindenmayer and Prusinkiewicz, 1996).

We use now a scaling argument similar to that of Rodriguez et al. (2008) for the dynamics of trees. On the ideal infinitely branched system of Fig. 5a, we can compare the stress level in branch $k=1$ (the trunk) and in branch $k=2$. The sub-tree labeled II in Fig. 5a is identical to the full tree, I, but for a change in length and diameter scales. All diameters (resp. lengths) in II are reduced by a factor $\lambda^{1/2}$ (resp. $\lambda^{1/2\beta}$). Let Σ_1 be the maximum skin stress in the trunk ($k=1$) under a given fluid-loading U, and Σ_2 the maximum skin stress in the branch $k=2$. The relations between the flow velocity and Σ_1 or Σ_2 are identical, but for the change of diameter and length scales. The dependence of the stress on

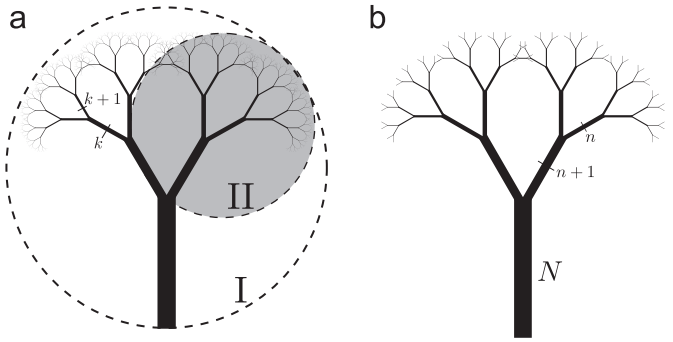

Fig. 5. Idealized branched system. (a) Infinite iterated tree. The sub-tree II is equivalent to the whole tree I but for a change of scales. (b) Finite iterated tree and corresponding notations.

diameter and length is the following: (i) Σ varies as M/D^3, where M is the bending moment, (ii) M varies as fL^2, where f is the norm of the local fluid force, Eq. (1), (iii) f varies as $\rho U^2 D$. Hence Σ varies as $\rho U^2 (L/D)^2$. We, therefore, may state that

$$\frac{\Sigma_2}{\Sigma_1} = \left(\frac{L_2}{D_2}\right)^2 \left(\frac{D_1}{L_1}\right)^2 = \lambda^{(1-\beta)/\beta}. \tag{4}$$

Since $\lambda < 1$, the condition for the stress to be higher in branches than in the trunk becomes

$$\beta > 1. \tag{5}$$

Here the only parameter controlling the possibility of branch breakage is the slenderness exponent, a classical parameter in the allometry of trees. As β is typically greater than 1 for trees, branch breakage is expected to occur. This simplistic approach now deserves to be improved, as the assumption of an infinite number of branching levels is very strong, and may not be compatible with the constraint that the tree area has to be finite.

4.2. Finite branched tree

Let us consider now the same idealized tree, but with a finite number of branching iterations (Fig. 5b). This structure has N levels, which are labeled in this section from the top to the bottom. Note that $n = N-k+1$, where k is the label of the previous section from the base of the tree. The trunk corresponds now to the last level, N. At each level n, we define the branch diameter D_n and length L_n, which can be expressed as a function of the trunk diameter and length D_N and L_N as

$$D_n = \lambda^{(N-n)/2} D_N, \quad L_n = \lambda^{(N-n)/2\beta} L_N. \tag{6}$$

By a simple integration of the fluid force on the branches, the moment at the base of a branch of order n may be derived, as well as the corresponding skin stress, which is obtained in non-dimensional form as

$$\sigma_n = C_Y \lambda^{N(1-\beta)/\beta} (A\lambda^{n(\beta-1)/\beta} + B\lambda^{n/2} + C\lambda^{n(\beta-1)/2\beta}), \tag{7}$$

where the Cauchy number C_Y is defined as

$$C_Y = \left[\frac{8}{\pi}\left(\frac{L_N}{D_N}\right)^2\right] \frac{\rho C_D U^2}{\Sigma_c}, \tag{8}$$

and A, B and C are functions of β and λ only. The detailed derivation of Eq. (7) as well as the expression of A, B and C can be found in Appendix A.

A systematic numerical exploration of the (λ,β) parameter space shows that when $\beta < 1$ the stress always increases from top to bottom. Conversely, for $\beta > 1$, the stress reaches a maximum at branch level n_c and then decreases from top to bottom, provided that $N > n_c$, where n_c depends on λ and β. This dependence is

given in Fig. 6. This analysis with a finite tree model gives a criterion consistent with that of the infinite tree model, namely $\beta > 1$. Moreover, the other parameter, λ, is found to affect only the location of possible breakage. This suggests that branching is not a key factor in the occurrence of branch or trunk breakage. In the next section we explore a simpler model of the slenderness effect.

5. The slender cone model

5.1. Flow-induced stress

The simplest model that allows one to take into account a relation between diameters and lengths through a slenderness exponent is a cone. This formulation is related to MacMahon and Kronauer's equivalent geometry of a tree, a tapered beam with a rectangular cross-section of dimensions varying as power laws of height (McMahon, 1975; McMahon and Kronauer, 1976).

The geometry considered here is a slender cone with a circular cross-section, Fig. 7a, and we follow the same mechanical approach as for the previous geometries. Let H be the cone height, $d_H = D_H/H$ the dimensionless diameter at the base and z the vertical coordinate which is orientated downwards in this section. The cone dimensionless diameter is given by

$$d(z) = d_H z^{\beta}. \tag{9}$$

Using the same formulation as in the previous section, the stress state along the cone is obtained as

$$\sigma(z) = C_Y z^{2(1-\beta)}, \tag{10}$$

where the Cauchy number is defined here as

$$C_Y = \left[\frac{16}{(1+\beta)(2+\beta)\pi d_H^2}\right]\frac{\rho C_D U^2}{\Sigma_c}. \tag{11}$$

From Eq. (10), we readily observe that: (i) for $\beta = 1$, the constant stress case of Bejan et al. (2008) is found; (ii) for $\beta < 1$ the stress increases with z and is, therefore, maximum at the base, Fig. 7a; (iii) for $\beta > 1$ the stress decreases with z, and the maximum, discussed further, is not at the base, Fig. 7b and c. These results are consistent with the condition for branch breakage in the previous section.

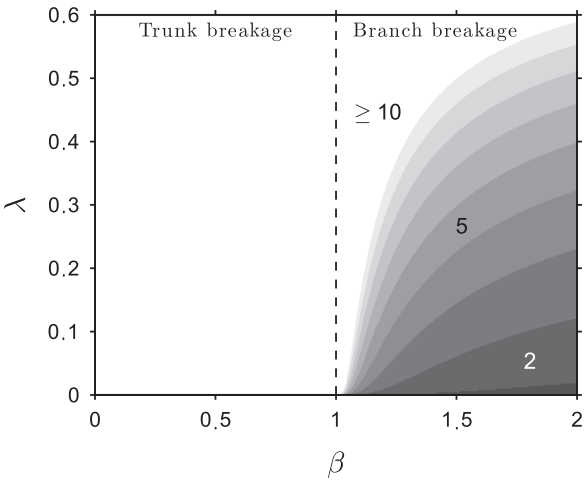

Fig. 6. Location of the maximum of stress under cross-flow in an idealized tree model, as a function of the slenderness exponent β and the branching parameter λ. The location is given in the form of the number of branching levels counted from the top of the tree, Fig. 5b. For $\beta \le 1$, the breakage is directly at the base of trunk.

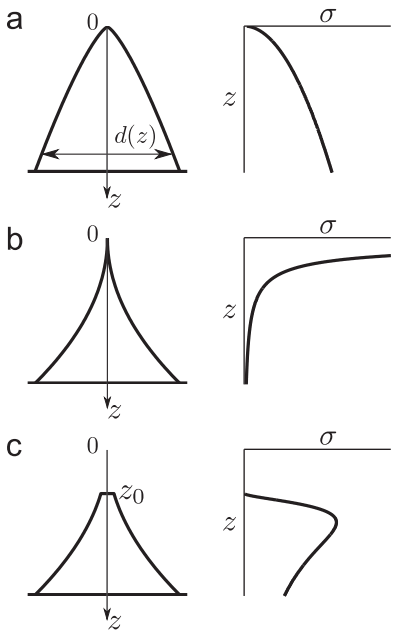

Fig. 7. The slender cone model: geometry and stress profile under uniform cross-flow. (a) cone with $\beta < 1$ (here 0.75), showing a maximum of stress at the base; (b) cone with $\beta > 1$ (here 2), showing a maximum at the top; (c) cone truncated arbitrarily at $z_0 = 0.3$ showing a local maximum.

To avoid the singular case of infinite stress at $z = 0$ for $\beta > 1$, we use a cone truncated at $z = z_0$, Fig. 7c. The truncation z_0 corresponds to the first breakage occurring as soon as $U \neq 0$, and its value is chosen arbitrarily. The corresponding stress state is then

$$\frac{\sigma(z)}{C_Y} = z^{2(1-\beta)} - (2+\beta)z_0^{1+\beta}z^{1-3\beta} + (1+\beta)z_0^{2+\beta}z^{-3\beta}, \tag{12}$$

which reduces to Eq. (10) when $z_0 = 0$. The detailed derivation of this equation is given in Appendix B. For $\beta > 1$, the stress shows a maximum before decreasing downwards, as illustrated in Fig. 7c. The limit case $z_0 = 0$ is in fact equivalent, in the ideal tree model of Section 4, to the limit as N goes towards infinity, which would lead to a vanishing diameter at the tip. There is, therefore, an analogy between the cone truncation and the ideal tree with a finite number of branching levels.

5.2. Sequence of breaking events

Considering now the generic case of the truncated cone, Fig. 7c, we analyze the sequence of breaking events resulting from an increasing fluid-loading C_Y. The stress σ increases linearly with C_Y up to the point where its maximum value reaches the limit of breakage, $\sigma = 1$. This defines the first breaking event at $C_Y = C_Y^1$ occurring at $z = z_1$. It results in a new truncated cone, and the process is repeated as C_Y is further increased. Eventually, when the cone becomes truncated close to the base, the maximum stress may be reached at the base itself, resulting finally in base breakage.

This sequence of breaking events may be analyzed in terms of the maximum fluid-loading $C_Y^{\max}$ that the cone can support before breaking at the base. As illustrated in Fig. 8, this is strongly dependent on β. When $\beta < 1$, the first breaking event is at the base so that $C_Y^{\max} = 1$. Conversely when $\beta > 1$, breaking occurs progressively as C_Y is increased, and the base breakage is delayed, $C_Y^{\max} > 1$. The precise value of C_Y where the base breaks depends on the initial truncation z_0, but is always higher than a lower bound that can be computed from Eq. (12), which is shown in

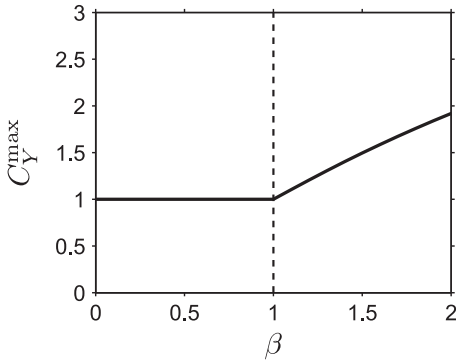

Fig. 8. Maximum fluid load that the cone can support as a function of the slenderness exponent. Note that for $\beta > 1$ the curve is the lower bound of all possible evolutions.

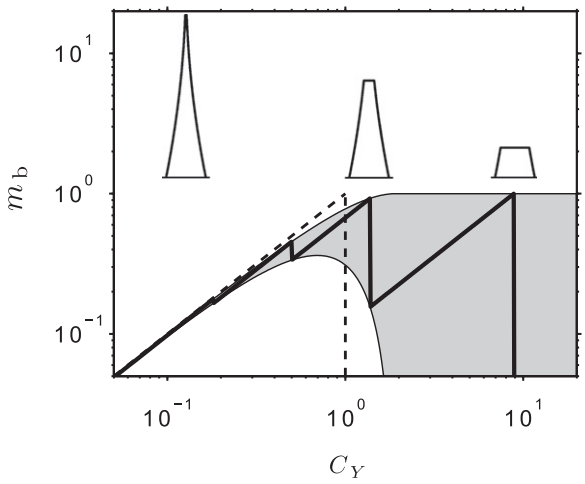

Fig. 9. Moment at the base of the cone as the fluid-loading is increased. (- -) direct base breakage occurring when $\beta < 1$; (—) progressive breaking for $\beta > 1$ (here $\beta = 2$). The shaded region shows all possible values depending on the initial truncation z_0. The cone state is shown for three values of C_Y.

Fig. 8. We observe a significant increase of the ability of the system to sustain fluid-loading when $\beta > 1$.

In terms of base moment, the sequence of breaking events can be easily computed, Fig. 9. For $\beta < 1$ the base moment increases linearly with C_Y until base breakage occurs, $m_b = 1$ for $C_Y = 1$. For $\beta > 1$ the sequence of breaking events results in sudden drops in base moment followed by linear increase up to the next breaking, as illustrated in Fig. 9. Since the sequence of breaking events is a discrete process that depends on the initial truncation z_0, there exists, for a given Cauchy number C_Y, a wide range of acceptable cone heights and thereby a wide range of corresponding base moments. In practice, for all possible values of z_0, the evolution of m_b remains bounded between its values for the shortest and highest cone that can exist at each Cauchy number. This is represented by the shaded region in Fig. 9.

These results show that the simple cone model contains the key elements to understand the effect of geometry on (i) the stress profile, (ii) the sequence of breaking events and (iii) the consequences on the evolution of base load when the fluid velocity is increased. Here again, the essential criterion concerns the slenderness exponent β.

6. Discussion and conclusions

Starting from the case of a full walnut tree geometry, we have used models of increasing simplicity. This allowed us to point out the role of various parameters on the process of breakage under fluid-loading. The first issue that had to be addressed was that of the flow-induced stress distribution. As noted by other authors, the stress is not necessarily maximum at the base (Niklas and Spatz, 2000; Bejan et al., 2008). In fact in the walnut tree of Section 3, the stress has a local maximum at about mid height. Using the ideal tree model in Section 4, we have shown that the existence of this maximum is related to the value of the slenderness exponent, β, being larger than one: in fact this allometry parameter is about 1.37 for this particular walnut tree (Rodriguez et al., 2008). Following Bejan et al. (2008), we recover the critical value of $\beta = 1$ in the simplest model, that of a cone in Section 5.

Actually, some refinement is needed here to understand the precise location of the maximum of stress. We have shown in Section 4 that the location of this maximum was also dependent on the branching parameter λ, in the form of the parameter n_c, which is the number of branching levels from the top to this maximum point. For our walnut tree, where $\lambda \simeq 0.25$, we obtain $n_c = 6$ using Fig. 6. This is smaller than the total number of branching levels in the walnut tree which is about 8 (Sinoquet et al., 1997). A local maximum of stress is, therefore, expected in the branches, and is actually observed in Fig. 3.

The second issue was that of the sequence of breaking events occurring when the fluid-loading C_Y is increased. Using a brittle fracture model for the walnut tree in Section 3, we have shown that most large branches broke in a short range of flow velocity, and that breakage of the trunk occurred much later. The large size of broken branches can be explained by the value of $n_c = 6$ found above. All large branches do not break exactly at the same value of the Cauchy number. This is due among other reasons to some variability in the allometry parameters λ and β within the tree. Once all large branches are broken, the remaining tree shape, C in Fig. 4a, does not have enough branching levels to have a local maximum, and the next breaking event occurs at the base of the trunk. Note that the process of branch breakage in the walnut tree allowed the tree to have a much larger acceptable Cauchy number before breakage of the trunk. This can also be analyzed using the cone model as in Section 5, where the critical Cauchy number for base breakage is clearly dependent on β (Fig. 8).

The third issue was that of the evolution of the load at the base of the tree. For the walnut tree, Fig. 4b, the sequence of successive breakage of the large branches results in a significant decrease of the drag-induced moment at the base. This can be understood using the cone model, where the sequence of breaking events and corresponding drops of base moment can be tracked, Fig. 9. We may, therefore, state that the essential characteristics of branch breakage and corresponding load evolution in the walnut tree can be understood using our simple ideal tree model and cone model.

The analytical results of Sections 4 and 5 were obtained considering that all parameters have self-similar variations. However, this was not the case for the walnut tree computations of Section 3, which suggests that the behaviors pointed out in this study can be generalized to structures that do not necessarily have self-similar variations of their parameters. Moreover, the ideal tree and cone models can be easily extended to incorporate other features of the problem, such as a dependence of all parameters with z: the flow velocity U, the material properties through the critical parameter Σ_c, and even the drag coefficient C_D, which allows one to take easily into account the additional drag of leaves. Preliminary results, not shown here for the sake of brevity, showed that the criterion for branch breakage takes the same form, but involves both β and the corresponding parameter related to the additional z-dependence. Taking into account a significant elastic deformation before load

fracture, or incorporating dynamical effects, would be much more complex.

Considering the simplicity of the criterion that we have found for branch breakage, we can test whether it is generally satisfied. McMahon and Kronauer (1976) have noted that β is usually larger than 1 and typically around 1.5, while λ is typically close to 0.25. This leads to a maximum stress located at a branching level $n_c=5$ counting from top down. This is clearly in the branches as trees generally have more than five orders of branching. We may, therefore, state that branch breakage can be expected in most sympodial trees. This is illustrated in Table 1, where the values of parameters are given for several trees.

Clearly the possibility of branch breakage is favorable in terms of survival of an individual tree in the face of extreme fluid-loading. It may also be favorable in terms of tree development by removing the less vigorous branches. The question then arises as to whether this implies new constraints on the geometry of the tree. It appears from our results that the constraint $\beta>1$ is not incompatible with other constraints such as the optimal resistance to buckling under gravity, which requires $\beta=3/2$ (McMahon, 1975). The same result was obtained considering the wind effect on trees but for an overcrowded tree canopy (Larjavaara, 2010). Similarly $\beta>1$ is compatible with a constraint for optimal dissipation (Rodriguez et al., 2008; Theckes et al., accepted), that modal frequencies have a ratio of less than two, requiring that $\beta>1$ for $\lambda=0.25$.

The particular case of branched corals (Madin, 2005; Tunnicliffe, 1981; Highsmith, 1982) is somewhat different. The segments are similar in length and diameter, so that $\lambda\simeq 1$ and $\beta\simeq 1$ in our variables, but with a number of branches emerging from one branching not equal to $1/\lambda$. An analysis similar to that of Section 4 shows that breakage is expected at the bottom. This is the case in most isolated corals.

More generally we may place these results in the overall context of reconfiguration, as introduced by Vogel (1989). This originally referred to the reduction of loading made possible by elastic deformation. For a plant, it is a crucial mechanism to survive heavy fluid-loading. But all plant tissues are not very elastic and all plants are not very flexible. Our results on the role of branch breakage in reducing loading show that, in parallel with elastic reconfiguration, there exists a mechanism of brittle reconfiguration. There are, therefore, two distinct strategies to overcome critical events. The first is evidently reversible in the short term by elasticity. The second is also reversible by re-growth, but only in the long term. Thus flow-induced pruning is possibly a widespread mechanism in plants or benthic organisms that support heavy loading by the surrounding fluid environment.

Acknowledgments

The authors gratefully acknowledge the help of Chris Bertram, from the University of Sydney, for stimulating discussions and useful corrections on the manuscript. The authors also acknowledge the interesting comments and useful suggestions from the anonymous reviewers. The first author was funded by the PhD scholarship program "AMX" at Ecole Polytechnique.

Appendix A. Stress derivation in finite branched tree model

In order to compute the stress along the finite ideal tree, we introduce f_n the fluid force per unit length at level n, $f_n=(1/2)\rho C_D U^2 D_n$, with the same notations as Eq. (1). At each level n, we consider two force components: (i) the shear force τ_n in the flow direction and (ii) the bending moment M_n in the direction normal to the flow. Due to the free condition at the top, $\tau_0=0$ and $M_0=0$, and for $n\geq 1$

$$\tau_n = f_n L_n + p\tau_{n-1}, \tag{A.1}$$

$$M_n = \tfrac{1}{2} f_n L_n^2 + p(M_{n-1} + L_n \tau_{n-1}), \tag{A.2}$$

where p is the number of branches emerging from one at a branching point ($p=1/\lambda$). The non-dimensional stress σ_n at level n reads

$$\sigma_n = \frac{32 M_n}{\pi \Sigma_c D_n^3}. \tag{A.3}$$

By integration of Eqs. (A.1) and (A.2), the stress at each level can be obtained,

$$\sigma_n = C_Y \lambda^{N(1-\beta)/\beta}(A\lambda^{n(\beta-1)/\beta} + B\lambda^{n/2} + C\lambda^{n(\beta-1)/2\beta}), \tag{A.4}$$

with

$$C_Y = \left[\frac{8}{\pi}\left(\frac{L_N}{D_N}\right)^2\right]\frac{\rho C_D U^2}{\Sigma_c}, \tag{A.5}$$

and

$$A = \frac{\lambda^{(1-\beta)/2\beta}+1}{(\lambda^{(1-\beta)/2\beta}-1)(\lambda^{(2-\beta)/2\beta}-1)}, \tag{A.6}$$

$$B = \frac{\lambda^{1/2\beta}+1}{(\lambda^{(2-\beta)/2\beta}-1)(\lambda^{1/2\beta}-1)}, \tag{A.7}$$

Table 1
Predicted breakage type using the results of Section 4. Branch breakage is predicted when $n_c \leq N$.

Ref.	Tree	Slenderness exponent β	Branching parameter λ	Total orders of branching N	Predicted branch breakage level n_c	Predicted breakage type
Sinoquet et al. (1997), Rodriguez et al. (2008)	Walnut Tree *Juglans Regia L.*	1.37	0.25	>8	6	Branch
McMahon and Kronauer (1976)	Red Oak *Quercus Rubra*	1.51	0.41	>6	7	Branch or Trunk
–	White Oak 1 *Quercus Alba*	1.41	0.28	>6	6	Branch
–	White Oak 2 *Quercus Alba*	1.66	0.29	>6	5	Branch
–	Poplar Tree *Populus Tremoloides*	1.5 (estimated)	0.29	>6	5	Branch
–	Pin Cherry *Prunus Pensylvanica*	1.5	0.24	>4	5	Branch or Trunk
–	White Pine *Pinus Strobus*	1.37	0.24	>5	5	Branch

$$C = \frac{-2}{(\lambda^{(1-\beta)/2\beta}-1)(\lambda^{1/2\beta}-1)}. \quad (A.8)$$

Appendix B. Stress derivation in the slender cone model

The stress state for the slender cone model is obtained by direct integration of the fluid force defined in Eq. (1), using Eq. (9) for the diameter. The shear force and resulting bending moment read

$$\tau(z) = \int_{z_0}^{z} f(z')\,\mathrm{d}z', \quad M(z) = \int_{z_0}^{z} \tau(z')\,\mathrm{d}z', \quad (B.1)$$

with $z_0 \geq 0$. The local non-dimensional skin stress reads

$$\sigma(z) = \frac{32\,M(z)}{\pi \Sigma_c d(z)^3}. \quad (B.2)$$

The integration of these equations give Eqs. (10) and (12) depending on z_0.

References

Barthelemy, D., Caraglio, Y., 2007. Plant architecture: a dynamic, multilevel and comprehensive approach to plant form, structure and ontogeny. Ann. Bot. 99, 375–407.

Beismann, H., Wilhelmi, H., Baillères, H., Spatz, H.C., Bogenrieder, A., Speck, T., 2000. Brittleness of twig bases in the genus Salix: fracture mechanics and ecological relevance. J. Exp. Bot. 51, 617–633.

Bejan, A., Lorente, S., Lee, J., 2008. Unifying constructal theory of tree roots, canopies and forests. J. Theor. Biol. 254, 529–540.

de Langre, E., 2008. Effects of wind on plants. Annu. Rev. Fluid Mech. 40, 141–168.

Gardiner, B.A., Quine, C.P., 2000. Management of forests to reduce the risk of abiotic damage—a review with particular reference to the effects of strong winds. For. Ecol. Manag. 135, 261–277.

Gere, J.M., Timoshenko, S.P., 1990. Mechanics of Materials. PWS-KENT, Boston, Massachusetts, USA.

Gosselin, F., de Langre, E., Machado-Almeida, B.A., 2010. Drag reduction of flexible plates by reconfiguration. J. Fluid Mech. 650, 319–341.

Highsmith, R.C., 1982. Reproduction by fragmentation in corals. Mar. Ecol. Prog. Ser. 7, 207–226.

Koehl, M.A.R., 1984. How do benthic organisms withstand moving water? Am. Zool. 24, 57–70.

Koehl, M.A.R., Silk, W.K., Liang, H., Mahadevan, L., 2008. How kelp produce blade shapes suited to different flow regimes: a new wrinkle. Integr. Comp. Biol. 48, 834–851.

Larjavaara, M., 2010. Maintenance cost, toppling risk and size of trees in a self-thinning stand. J. Theor. Biol. 265, 63–67.

Lindenmayer, A., Prusinkiewicz, P., 1996. The Algorithmic Beauty of Plants. Springer-Verlag.

Lundström, T., Jonas, T., Volkwein, A., 2008. Analysing the mechanical performance and growth adaptation of norway spruce using a non-linear finite-element model and experimental data. J. Exp. Bot. 59, 2513–2528.

Madin, J.S., 2005. Mechanical limitations of reef corals during hydrodynamic disturbances. Coral Reefs 24, 630–635.

Madin, J.S., Connolly, S.R., 2006. Ecological consequences of major hydrodynamic disturbances on coral reefs. Nature 444, 477–480.

Martone, P.T., Denny, M.W., 2008. To break a coralline: mechanical constraints on the size and survival of a wave-swept seaweed. J. Exp. Biol. 211, 3433–3441.

McMahon, T.A., 1975. The mechanical design of trees. Sci. Am. 233, 93–102.

McMahon, T.A., Kronauer, R.E., 1976. Tree structures: deducing the principle of mechanical design. J. Theor. Biol. 59, 443–466.

Moulia, B., Coutand, C., Lenne, C., 2006. Posture control and skeletal mechanical acclimation in terrestrial plants: implications for mechanical modeling of plant architecture. Am. J. Bot. 93, 1477–1489.

Niklas, K.J., 1992. Plant Biomechanics: An Engineering Approach to Plant Form and Function. University of Chicago Press, Chicago, Illinois, USA.

Niklas, K.J., Spatz, H., 1999. Methods for calculating factors of safety for plant stems. J. Exp. Biol. 202, 3273–3280.

Niklas, K.J., Spatz, H.C., 2000. Wind-induced stresses in cherry trees: evidence against the hypothesis of constant stress levels. Trees 14, 0230–0237.

Rodriguez, M., de Langre, E., Moulia, B., 2008. A scaling law for the effects of architecture and allometry on tree vibration modes suggests a biological tuning to modal compartmentalization. Am. J. Bot. 95, 1523–1537.

Sinoquet, H., Rivet, P., Godin, C., 1997. Assessment of the three-dimensional architecture of walnut trees using digitizing. Silva Fenn. 31, 265–273.

Tunnicliffe, V., 1981. Breakage and propagation of the stony coral acropora cervicornis. Proc. Natl. Acad. Sci. USA 78, 2427–2431.

Theckes, B., de Langre, E., Boutillon, X. Damping by branching: a bioinspiration from trees. ArXiv paper 1106.1283.

Vogel, S., 1989. Drag and reconfiguration of broad leaves in high winds. J. Exp. Bot. 40, 941–948.

Verpeaux, P., Charras, T., Millard, A., 1988. Castem 2000, une approche moderne du calcul des structures. In: Fouet, J.M., Ladevèze, P., Ohayon, R., (Eds.), Calcul des structures et intelligence artificielle. Pluralis, Paris, France, pp. 261–271.

Bibliography

Alben, S., Shelley, M. & Zhang, J. 2002 Drag reduction through self-similar bending of a flexible body. *Nature* **420**, 479–481.

Bai, K., Meneveau, C. & Katz, J. 2012 Near-wake turbulent flow structure and mixing length downstream of a fractal tree. *Boundary-Layer Meteorology* **143**, 285–308, 10.1007/s10546-012-9700-2.

Baker, C.J. 1995 The development of a theoretical model for the windthrow of plants. *Journal of Theoretical Biology* **175** (3), 355 – 372.

Baker, C.J. 1997 Measurements of the natural frequencies of trees. *Journal of Experimental Botany* **48** (5), 1125–1132.

Balsamo, R. A., Bauer, A. M., Davis, S. D. & Rice, B. M. 2003 Leaf biomechanics, morphology, and anatomy of the deciduous mesophyte *Prunus serrulata* (rosaceae) and the evergreen sclerophyllous shrub *Heteromeles arbutifolia* (rosaceae). *American Journal of Botany* **90** (1), 72–77.

Barthelemy, D. & Caraglio, Y. 2007 Plant Architecture: A Dynamic, Multilevel and Comprehensive Approach to Plant Form, Structure and Ontogeny. *Annals of Botany* **99** (3), 375–407.

Beismann, H., Wilhelmi, H., Baillères, H., Spatz, H. C., Bogenrieder, A. & Speck, T. 2000 Brittleness of twig bases in the genus Salix: fracture mechanics and ecological relevance. *Journal of Experimental Botany* **51** (344), 617–633.

Bejan, A., Lorente, S. & Lee, J. 2008 Unifying constructal theory of tree roots, canopies and forests. *Journal of Theoretical Biology* **254** (3), 529 – 540.

Berry, P. M., Sterling, M., Spink, J. H., Baker, C. J., Sylvester-Bradley, R., Mooney, S. J., Tams, A. R. & Ennos, A. R. 2004 Understanding and reducing lodging in cereals. *Advances in Agronomy* **84**, 217 – 271.

Bertram, J. E. A. 1989 Size-dependent differential scaling in branches: the mechanical design of trees revisited. *Trees* **3** (4).

Bjurhager, I., Berglund, L., Bardage, S. & Sundberg, B. 2008 Mechanical characterization of juvenile european aspen (*Populus tremula*) and hybrid aspen (*Populus tremula* × *Populus tremuloides*) using full-field strain measurements. *Journal of Wood Science* **54**, 349–355.

Bruchert, F. & Gardiner, B. 2006 The effect of wind exposure on the tree aerial architecture and biomechanics of sitka spruce (*Picea sitchensis, Pinaceae*). *American Journal of Botany* **93** (10), 1512–1521.

Butler, D. W., Gleason, S. M., Davidson, I., Onoda, Y. & Westoby, M. 2012 Safety and streamlining of woody shoots in wind: an empirical study across 39 species in tropical australia. *New Phytologist* **193** (1), 137–149.

Chapelle, D., Gerbeau, J.-F., Sainte-Marie, J. & Vignon-Clementel, I. 2010 A poroelastic model valid in large strains with applications to perfusion in cardiac modeling. *Computational Mechanics* **46**, 91–101.

Coutand, C. & Moulia, B. 2000 Biomechanical study of the effect of a controlled bending on tomato stem elongation: local strain sensing and spatial integration of the signal. *Journal of Experimental Botany* **51** (352), 1825–1842.

Crook, M. J., Ennos, A. R. & Sellers, E. K. 1994 Structural development of the shoot and root systems of two winter wheat cultivars, *Triticum aestivum L. Journal of Experimental Botany* **45** (6), 857–863.

Denny, M. W. & Gaylord, B. 2010 Marine ecomechanics. *Annual Review of Marine Science* **2** (1), 89–114.

Diebels, S. & Ehlers, W. 1996 Dynamic analysis of a fully saturated porous medium accounting for geometrical and material non-linearities. *International Journal for Numerical Methods in Engineering* **39** (1), 81–97.

Doaré, O., Moulia, B. & de Langre, E. 2004 Effect of plant interaction on wind-induced crop motion. *Transactions of the ASME: Journal of Biomechanical Engineering* **126**, 146–151.

Dupont, S. & Brunet, Y. 2008 Edge flow and canopy structure: A large-eddy simulation study. *Boundary-Layer Meteorology* **126**, 51–71.

Dupont, S., Gosselin, F., Py, C., de Langre, E., Hemon, P. & Brunet, Y. 2010 Modelling waving crops using large-eddy simulation: comparison with experiments and a linear stability analysis. *Journal of Fluid Mechanics* **652**, 5–44.

Eloy, C. 2011 Leonardo's rule, self-similarity, and wind-induced stresses in trees. *Physical Review Letters* **107**, 258101.

Endalew, A. M., Hertog, M., Gebrehiwot, M. Gebreslasie, Baelmans, M., Ramon, H., Nicolai, B. M. & Verboven, P. 2009 Modelling airflow within model plant canopies using an integrated approach. *Computers and Electronics in Agriculture* **66** (1), 9 – 24.

Farquhar, T., Wood, J. Z. & van Beem J. 2000 The kinematics of wheat struck by a wind gust. *Journal of applied mechanics* **67** (3), 496–502.

Fontenrose, J. 1988 *Didyma: Apollo's Oracle, Cult, and Companions*. University of California Press.

Gardiner, B., Byrne, K., Hale, S., Kamimura, K., Mitchell, S. J., Peltola, H. & Ruel, J-C. 2008 A review of mechanistic modeling of wind damage risk to forests. *Forestry* **81** (3), 447–463.

Gardiner, B., Peltola, H. & Kellomaki, S. 2000 Comparison of two models for predicting the critical wind speeds required to damage coniferous trees. *Ecological Modelling* **129** (1), 1–23.

Gardiner, B. A. & Quine, C. P. 2000 Management of forests to reduce the risk of abiotic damage – a review with particular reference to the effects of strong winds. *Forest Ecology and Management* **135** (1-3), 261 – 277.

Gaylord, B., Denny, M. W. & Koehl, M. A. R. 2008 Flow forces on seaweeds: Field evidence for roles of wave impingement and organism inertia. *The Biological Bulletin* **215** (3), 295–308.

Gere, J. M. & Timoshenko, S. P. 1990 *Mechanics of Materials*. Boston, Massachusetts, USA: PWS-KENT.

Ghisalberti, M. & Nepf, H. M. 2002 Mixing layers and coherent structures in vegetated aquatic flows. *Journal of Geophysical Research* **107** (C2), 1–11.

Gosselin, F. & de Langre, E. 2009 Destabilising effects of plant flexibility in air and aquatic vegetation canopy flows. *European Journal of Mechanics - B/Fluids* **28** (2), 271 – 282.

Gosselin, F., de Langre, E. & Machado-Almeida, B. A. 2010 Drag reduction of flexible plates by reconfiguration. *Journal of Fluid Mechanics* **650**, 319–341.

Gosselin, F. P. & de Langre, E. 2011 Drag reduction by reconfiguration of a poroelastic system. *Journal of Fluids and Structures* **27** (7), 1111 – 1123.

Grant, R. H. 1983 The scaling of flow in vegetative structures. *Boundary-Layer Meteorology* **27**, 171–184.

Higdon, J. J. L. & Ford, G. D. 1996 Permeability of three-dimensional models of fibrous porous media. *Journal of Fluid Mechanics* **308**, 341–361.

Highsmith, R. C. 1982 Reproduction by fragmentation in corals. *Marine Ecology - Progress Series* **7**, 207–226.

Hoffmann, M. R. 2004 Application of a simple spacetime averaged porous media model to flow in densely vegetated channels. *Journal of Porous Media* **7** (3), 183–191.

Hsieh, P-C. & Shiu, Y-S. 2006 Analytical solutions for water flow passing over a vegetal area. *Advances in Water Resources* **29** (9), 1257 – 1266.

Huler, S. 2004 *Defining the wind: the Beaufort scale, and how a nineteenth century admiral turned science into poetry*. Crown Publishers.

Inoue, E. 1955 Studies of the phenomena of waving plant ("honami") caused by wind. part 1: Mechanism and characteristics of waving plant phenomena. *Journal of Agricultural Meteorology (Japan)* **11**, 71–82.

Jacobs, M. R. 1954 The effect of wind sway on the form and development of *Pinus radiata* d. don. *Australian Journal of Botany* **2**, 35–51.

Jacquelin, E., Brochard, D., Trollat, C. & Jézéquel, L. 1996 Homogenization of a non-linear array of confined beams. *Nuclear Engineering and Design* **165**, 213–223.

Jaffe, M. J. 1973 Thigmomorphogenesis: The response of plant growth and development to mechanical stimulation. *Planta* **114**, 143–157.

Kane, B., Pavlis, M., Harris, J. R. & Seiler, J. R. 2008 Crown reconfiguration and trunk stress in deciduous trees. *Canadian Journal of Forest Research* **38**, 1275–1289.

Kerzenmacher, T. & Gardiner, B. 1998 A mathematical model to describe the dynamic response of a spruce tree to the wind. *Trees - Structure and Function* **12**, 385–394.

Koch, D. L. & Ladd, A. J. C. 1997 Moderate reynolds number flows through periodic and random arrays of aligned cylinders. *Journal of Fluid Mechanics* **349**, 31–66.

Koehl, M. A. R. 1984 How do benthic organisms withstand moving water? *American Zoologist* **24** (1), 57 –70.

Koehl, M. A. R. & Alberte, R. S. 1988 Flow, flapping, and photosynthesis of *Nereocystis leutkeana* a functional comparison of undulate and flat blade morphologies. *Marine Biology* **99**, 435–444.

Koehl, M. A. R., Silk, W. K., Liang, H. & Mahadevan, L. 2008 How kelp produce blade shapes suited to different flow regimes: A new wrinkle. *Integrative and Comparative Biology* **48** (6), 834 –851.

de Langre, E. 2008 Effects of wind on plants. *Annual Review of Fluid Mechanics* **40** (1), 141–168.

de Langre, E., Gutierrez, A. & Cossé, J. 2012 On the scaling of drag reduction by reconfiguration in plants. *C. R. Mecanique* **340** (1-2), 35 – 40.

Larjavaara, M. 2010 Maintenance cost, toppling risk and size of trees in a self-thinning stand. *Journal of Theoretical Biology* **265** (1), 63 – 67.

Lene, F. 1984 Contribution l'étude des matériaux composites et de leur endommagement. PhD thesis, Université Pierre et Marie Curie, Paris.

Lindenmayer, A. & Prusinkiewicz, P. 1996 *The algorithmic beauty of plants*. Springer-Verlag.

Liu, D., Diplas, P., Hodges, C. C. & Fairbanks, J. D. 2010 Hydrodynamics of flow through double layer rigid vegetation. *Geomorphology* **116** (3-4), 286 – 296.

Lopez, D., Michelin, S. & de Langre, E. 2011 Flow-induced pruning of branched systems and brittle reconfiguration. *Journal of Theoretical Biology* **284** (1), 117 – 124.

der Loughian, C. 2012 Effets de la dynamique sur la croissance du peuplier en réponse une stimulation mécanique externe. PhD thesis, Ecole Polytechnique, Paris.

Luhar, M. & Nepf, H. M. 2011 Flow-induced reconfiguration of buoyant and flexible aquatic vegetation. *Limnology and Oceanography* **56** (6), 2003 – 2017.

Lundstrom, T., Jonas, T. & Volkwein, A. 2008 Analysing the mechanical performance and growth adaptation of norway spruce using a non-linear finite-element model and experimental data. *Journal of Experimental Botany* **59** (9), 2513–2528.

Madin, J. S. 2005 Mechanical limitations of reef corals during hydrodynamic disturbances. *Coral Reefs* **24** (4), 630–635.

Madin, J. S. & Connolly, S. R. 2006 Ecological consequences of major hydrodynamic disturbances on coral reefs. *Nature* **444** (7118), 477–480.

Martone, P. T. & Denny, M. W. 2008 To break a coralline: mechanical constraints on the size and survival of a wave-swept seaweed. *Journal of Experimental Biology* **211** (21), 3433–3441.

McMahon, T. A. 1975 The mechanical design of trees. *Scientific American* **233**, 93–102.

McMahon, T. A. & Kronauer, R. E. 1976 Tree structures: Deducing the principle of mechanical design. *Journal of Theoretical Biology* **59** (2), 443–466.

Moulia, B. & Combes, D. 2004 Thigmomorphogenetic acclimation of plants to moderate winds greatly affects height structure in field-gown alfalfa (medicago sativa l.), an indeterminate herb. *Comparative Biochemistry and Physiology Part A : Molecular & Integrative Physiology* **137** (3-S1), 77.

Moulia, B., Coutand, C. & Lenne, C. 2006 Posture control and skeletal mechanical acclimation in terrestrial plants: implications for mechanical modeling of plant architecture. *American Journal of Botany* **93** (10), 1477–1489.

Nepf, H. M. 1999 Drag, turbulence, and diffusion in flow through emergent vegetation. *Water Resources Research* **35**, 479–489.

Nicoll, B. C., Gardiner, B. A. & Peace, A. J. 2008 Improvements in anchorage provided by the acclimation of forest trees to wind stress. *Forestry* **81** (3), 389–398.

Niklas, K. J. 1992 *Plant biomechanics: an engineering approach to plant form and function*. Chicago, Illinois, USA: University of Chicago Press.

Niklas, K. J. & Spatz, H. 1999 Methods for calculating factors of safety for plant stems. *Journal of Experimental Biology* **202** (Pt 23), 3273–3280.

Niklas, K. J. & Spatz, H. C. 2000 Wind-induced stresses in cherry trees: evidence against the hypothesis of constant stress levels. *Trees* **14** (4), 0230–0237.

Ochoa-Tapia, J. A. & Whitaker, S. 1995 Momentum transfer at the boundary between a porous medium and a homogeneous fluid–I. theoretical development. *International Journal of Heat and Mass Transfer* **38** (14), 2635–2646.

Pedras, Marcos H.J. & de Lemos, Marcelo J.S. 2001 Macroscopic turbulence modeling for incompressible flow through undeformable porous media. *International Journal of Heat and Mass Transfer* **44** (6), 1081 – 1093.

Py, C., de Langre, E. & Moulia, B. 2006 A frequency lock-in mechanism in the interaction between wind and crop canopies. *Journal of Fluid Mechanics* **568**, 425–449.

Py, C., de Langre, E., Moulia, B. & Hémon, P. 2005 Measurement of wind-induced motion of crop canopies from digital video images. *Agricultural and Forest Meteorology* **130**, 223236.

Raupach, M. R., Finnigan, J. J. & Brunet, Y. 1996 Coherent eddies and turbulence in vegetation canopies: The mixing-layer analogy. *Boundary-Layer Meteorology* **78**, 351–382.

Richter, J.P. & Bell, R.C. 1970 *The Notebooks of Leonardo Da Vinci*. Dover Publications.

Rodriguez, M., de Langre, E. & Moulia, B. 2008 A scaling law for the effects of architecture and allometry on tree vibration modes suggests a biological tuning to modal compartmentalization. *American Journal of Botany* **95** (12), 1523–1537.

Rosner, S., Klein, A., Muller, U. & Karlsson, B. 2007 Hydraulic and mechanical properties of young norway spruce clones related to growth and wood structure. *Tree Physiology* **27** (8), 1165–1178.

Rudnicki, M., Mitchell, S. J. & Novak, M. D. 2004 Wind tunnel measurements of crown streamlining and drag relationships for three conifer species. *Canadian Journal of Forest Research* **34** (3), 666–676.

Salençon, J. 2001 *Handbook of Continuum Mechanics: General Concepts, Thermoelasticity*. Springer.

Schouveiler, L. & Boudaoud, A. 2006 The rolling up of sheets in a steady flow. *Journal of Fluid Mechanics* **563**, 71–80.

Sellier, D. & Fourcaud, T. 2005 A mechanical analysis of the relationship between free oscillations of pinus pinaster ait. saplings and their aerial architecture. *Journal of Experimental Botany* **56** (416), 1563–1573.

Sigrist, J.-F. & Broc, D. 2008 Dynamic analysis of a tube bundle with fluid-structure interaction modelling using a homogenisation method. *Computer Methods in Applied Mechanics and Engineering* **197**, 1080 – 1099.

Sinoquet, H., Rivet, P. & Godin, C. 1997 Assessment of the three-dimensional architecture of walnut trees using digitizing. *Silva Fennica* **31** (3), 265–273.

Speck, O. & Spatz, H.-C. 2004 Damped oscillations of the giant reed arundo donax (poaceae). *American Journal of Botany* **91** (6), 789–796.

Speck, T. & Burgert, I. 2011 Plant stems: Functional design and mechanics. *Annual Review of Materials Research* **41** (1), 169–193.

Stewart, H. L. 2006 Hydrodynamic consequences of flexural stiffness and buoyancy for seaweeds: a study using physical models. *Journal of Experimental Biology* **209** (11), 2170–2181.

Tanino, Y. & Nepf, H. M. 2008 Lateral dispersion in random cylinder arrays at high reynolds number. *Journal of Fluid Mechanics* **600**, 339–371.

Telewski, F. W. 2006 A unified hypothesis of mechanoperception in plants. *American Journal of Botany* **93** (10), 1466–1476.

Theckes, B., de Langre, E. & Boutillon, X. 2011 Damping by branching: a bioinspiration from trees. *Bioinspiration & Biomimetics* **6** (4), 046010.

Tunnicliffe, V. 1981 Breakage and propagation of the stony coral acropora cervicornis. *Proceedings of the National Academy of Science of the USA* **78** (4), 2427 –2431.

Vernier, F. 2001 Storm Lothar, December 1999 26th: Effects and perspectives on the forest in Lorraine. `http://hdl.handle.net/2042/27569`.

Verpeaux, P., Charras, T. & Millard, A. 1988 Castem 2000, une approche moderne du calcul des structures. In *Calcul des structures et intelligence artificielle* (ed. J. M. Fouet, P. Ladevèze & R. Ohayon), pp. 261–271. Paris, France: Pluralis.

Vogel, S. 1984 Drag and flexibility in sessile organisms. *American Zoologist* **24** (1), 37–44.

Vogel, S. 1989 Drag and reconfiguration of broad leaves in high winds. *Journal of Experimental Botany* **40** (8), 941 –948.

Vollsinger, S., Mitchell, S. J., Byrne, K. E., Novak, M. D. & Rudnicki, M. 2005 Wind tunnel measurements of crown streamlining and drag relationships for several hardwood species. *Canadian Journal of Forest Research* **35** (5), 1238–1249.

Whitaker, S. 1999 *The Method of Volume Averaging*. Kluwer.

Internet references

[WEB01]: Champ de blé mûr après une tempête, `www.planete-revelations.com`

[WEB02]: Flag tree, `www.crosthwaiteandlyth.co.uk`